Deeply Virtual Compton Scattering off an Unpolarised Hydrogen Target using the Recoil Detector at HERMES

Jennifer Ruth Bowles

A thesis presented for the degree of
Doctor of Philosophy

Nuclear Physics Research Group
School of Physics and Astronomy
University of Glasgow
Scotland

December 2012

Deeply Virtual Compton Scattering off an Unpolarised Hydrogen Target using the Recoil Detector at HERMES

J R Bowles

Submitted for the degree of Doctor of Philosophy
December 2012

Abstract

Deeply Virtual Compton Scattering (DVCS) provides the simplest access to Generalised Parton Distributions (GPDs), which is a theoretical framework that describes nucleon structure. The GPDs are of particular interest due to the fact that they can provide a 3–dimensional description of the nucleon structure and can be used to determine the total angular momentum of quarks inside the nucleon. The DVCS interaction can be accessed via its interference with the Bethe-Heitler process, which is an experimentally indistinguishable process. At HERMES, asymmetries in the distribution of the real photon around the azimuthal angle for DVCS are measured. The beam–helicity asymmetry amplitudes are extracted from DVCS events with an unpolarised target during the 2006–2007 data taking period. This measurement made use of the final upgrade to the HERMES experiment, the Recoil Detector. This upgrade ensured a truly exclusive DVCS measurement could be made by measuring the recoiling proton.

Declaration

The work in this thesis is based on research carried out at the Nuclear Physics Group, School of Physics and Astronomy, University of Glasgow, Scotland. No part of this thesis has been submitted elsewhere for any other degree or qualification and it is all my own work unless referenced to the contrary in the text.

Acknowledgements

The work in this thesis would not have been possible if it had not been for the help and support from various people over the last few years. First of all I'd like to thank my supervisors, Profs Ralf Kaiser, David Ireland and Guenther Rosner. During my PhD their help and support has been invaluable and provided opportunities to travel, and to acquire new skills.

In order to complete the work, I also worked closely with Sergey Yaschenko and Caroline Riedl. I'd like to thank them both for their help and advice at various stages of the analysis. Id also like to thank the other members of the HERMES DVCS group, for their ideas, suggestions and comments during the analysis.

A great deal of thanks must go to the other Hermesians in Glasgow: Jonathan Burns, David Mahon, Gordon Hill, Morgan Murray and Inti Lehmann. I am very fortunate to have had their guidance and enjoyed worked alongside them.

I would also like to thank the many people I shared an office with during my PhD: Eilidh McNicholl, Seian Al Jebali, Rachel Montgomery, Stefanie Lewis, Gary Smith, Mark Anderson and Jeffrey Philips. Also another special thanks should go to Stuart Fegan for organising daily coffee trips.

Finally I'd like to thank my family, especially my to Mum and Siôn. Diolch yn fawr iawn ichi gyd am y cymorth dros y blynyddoedd diwethaf. Diolch arbenig hefyd i Marian am ddarllen trwy'r gwaith.

Contents

List of Figures

List of Tables

Chapter 1

Introduction

Atoms consist of a central positively charged nucleus surrounded by a cloud of negatively charged electrons. The nucleus consists of positively charged protons and electrically neutral neutrons, known as nucleons. Nucleons are composed of quarks that interact via the exchange of gluons. A proton consists of two up quarks and one down quark, referred to as valence quarks. The gluons can split into quark-antiquark pairs, known as sea quarks.

A complete picture of the internal structure of the nucleon cannot yet be constructed. Our present knowledge is based on measurements of high energy scattering experiments.

Nucleon spin is known to be $\frac{1}{2}\hbar$, and was thought to be due to the spin of the quarks (spin-$\frac{1}{2}\hbar$ fermions). However measurements have shown otherwise. Measurements of the contribution of the quark spins to nucleon spin were first shown to be consistent with zero within experimental uncertainties by the European Muon Collaboration (EMC) experiment in CERN [1]. More precise measurements have shown that the contribution from quark spins is $\approx 33\%$ [2,3]. The spin of a nucleon can be decomposed into contributions from the constituent partons [4];

$$\frac{1}{2} = \frac{1}{2}\Delta\Sigma + L_q + \Delta g + L_g, \tag{1.1}$$

where $\Delta\Sigma$ (Δg) is the contribution from the spin of the quarks (gluons) and L_q (L_g) is the orbital angular momentum of the quarks (gluons). Determining the

contributions to nucleon spin is still one of the most interesting questions in particle physics. Recent measurements of Δg indicate that this is small, which suggests that the orbital angular momentum of the partons is significant.

The only known method to access L_q experimentally is via Generalised Parton Distributions (GPDs). These GPDs have been proven by Xiangdong Ji [4] to be related to J_q, where $J_q = L_q + \frac{1}{2}\Delta\Sigma$. Since the spin contribution from quarks is already known, L_q can be determined once J_q is known.

Apart from providing insight into the spin structure of the nucleon, GPDs can also provide a multidimensional description of the structure of the proton and other bound states [5].

The simplest way to access GPDs experimentally is via Deeply Virtual Compton Scattering (DVCS) [5]. This is the process where a lepton interacts with a quark in the nucleon via exchange of a virtual photon. The quark absorbs the virtual photon, and emits a real photon as it is reabsorbed by the nucleon. There is also another scattering process which is experimentally indistinguishable from DVCS, Bethe-Heitler, where the final photon is radiated from the incoming or outgoing lepton. Because they have the same final state, they interfere and this results in an interference term in the cross section for the exclusive leptoproduction of real photons. For fixed target experiments the DVCS cross section is considerably smaller than BH, however the DVCS amplitude can still be accessed via the interference term. It is possible to access this term from asymmetries in the distribution of real photons with respect to the azimuthal angle between the scattering and photoproduction planes. A number of asymmetries have been published by HERMES, all providing information about GPDs [6–9].

Prior to the installation of a Recoil Detector in 2005/2006, the selection of DVCS events at HERMES was determined by a missing mass technique. This work will present the first truly exclusive measurement of DVCS at HERMES, using the Recoil Detector during the final running period of HERMES. A truly exclusive measurement will mean that the amount of contamination from background processes will be reduced.

This thesis continues in Chapter 2 by explaining some of the theoretical frame-

work which describes our current understanding of the nucleon structure. The GPD models used to compare the result presented in the thesis will be outlined. The $e\,p \rightarrow e\,p\,\gamma$ process is described, and the relation between the DVCS Beam Helicity Amplitude (BHA) measured and the GPDs is presented. The experimental setup of HERMES is then outlined in Chapter 3, focusing on the sub-detectors relevant to this measurement.

The data analysis procedure, from the selection of events to the extraction of the Beam Helicity Asymmetry amplitudes is described in Chapter 4. Chapter 5 explains the studies undertaken to determine the systematic uncertainties, and how they are taken into consideration.

The final results are presented in Chapter 6, alongside comparisons to the GPD models described in Chapter 2. They are also compared to previous measurements by HERMES that did not use the Recoil Detector, and results from Jefferson Lab.

Chapter 2

Nucleon Structure

Much of the current knowledge about the structure of the nucleon comes from scattering high energy leptons off a nucleon. Leptons are used as probes for studying nucleon structure due to their structureless nature and their interactions with matter, which are governed by electromagnetic fields and thus are well understood.

How quarks and gluons make up nucleons has been studied via Form Factors (FFs) in elastic scattering and via Parton Distribution Functions (PDFs) in Deep Inelastic Scattering (DIS).

More recently, Generalised Parton Distributions (GPDs) have been introduced to provide a more complete description of the nucleon structure. They encompass the information from FFs and PDFs as moments and limits and are capable of yielding a rich vein of information on nucleon structure.

2.1 Elastic Scattering

First studied in the 1950's at Stanford [10], elastic electron proton scattering ($ep \to e'p$) provided the first hints on nucleon structure. The leading order Feynman diagram for this process is illustrated in Figure 2.1.

If the nucleon were a structureless object, the scattering of an electron off it would be described by the Mott cross section. The structure of the nucleon is absorbed into the Dirac, Pauli, axial and pseudoscalar form factors,$F_1(t), F_2(t), G_A$ and G_P respectively, which are defined separately for each quark flavour, u, d and s. They

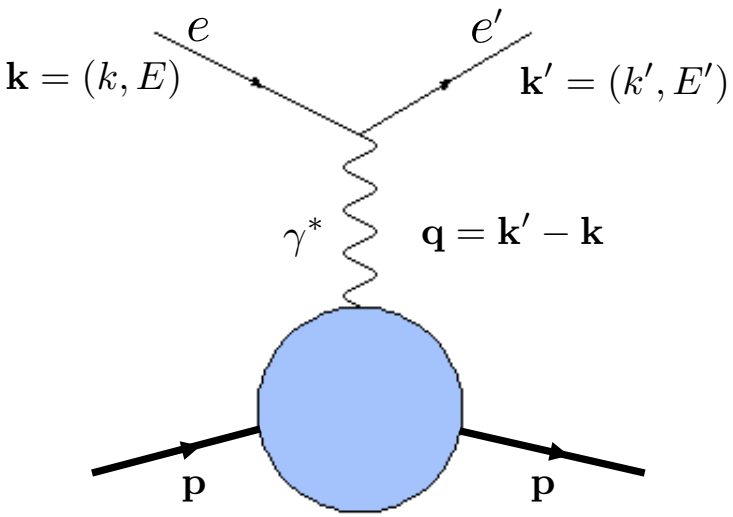

Figure 2.1: Diagram depicting the 1–photon exchange approximation for elastic $ep \rightarrow e'p$ scattering.

depend only on the Mandalstam variable t, which is defined as the 4–momentum transfer between the final and initial nucleon,

$$t = (k - k')^2. \tag{2.1}$$

where $\mathbf{k}\,(E)$ and $\mathbf{k}'\,(E')$ are the four–momenta (energies) of the incoming and outgoing lepton, and q is the 4–momentum of the virtual photon as depicted in Figure 2.1. The Dirac and Pauli form factors can be rewritten in terms of Sachs electric and magnetic form factors G_E and G_M. Via a Fourier transform, these can then be interpreted as the transverse spatial density of electric and magnetic charges within the nucleon in the infinite momentum frame.

2.2 Inclusive Scattering

Inclusive scattering ($lN \rightarrow lX$) is a process where only the scattered lepton is detected, and the resulting nucleon state goes unobserved. Deep Inelastic Scattering (DIS), where a virtual photon from the scattered lepton is exchanged with a quark

in the nucleon is depicted in Figure 2.2 and was first studied at the Stanford Linear Accelerator Center (SLAC) in the 1960's.

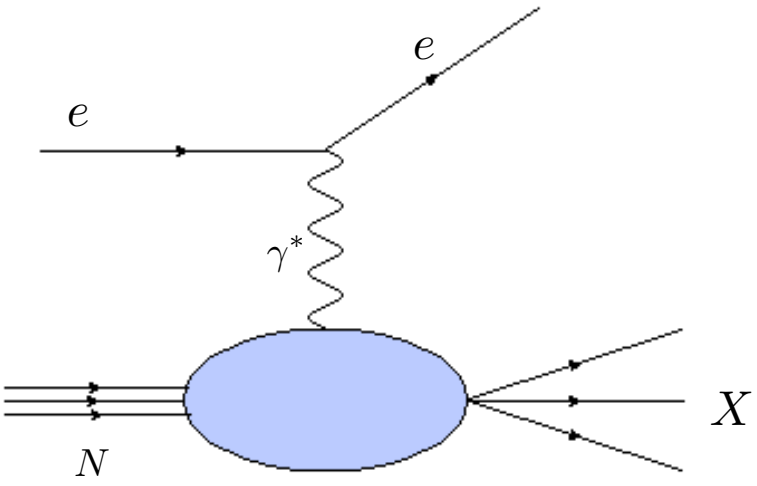

Figure 2.2: The leading order diagram for deep inelastic scattering

To describe DIS, the following kinematic variables are used.

- The Lorentz–invariant negative squared four–momentum of the virtual photon, Q^2 is defined as

$$Q^2 = -q^2 = -(\mathbf{k} - \mathbf{k}')^2. \tag{2.2}$$

- The energy of the virtual photon or the energy transfer from the lepton to the virtual photon is defined as:

$$\nu = \frac{\mathbf{p} \cdot \mathbf{q}}{M_N}, \tag{2.3}$$

  where M_N is target nucleon mass.

- The squared invariant mass of the virtual photon–target system, $\gamma^\star p$, (or the final hadronic system) is defined as

$$W^2 = (\mathbf{p} + \mathbf{q})^2. \tag{2.4}$$

- The Bjorken scaling variable

$$x_B = \frac{Q^2}{2\mathbf{p}\cdot\mathbf{q}}. \tag{2.5}$$

- The fractional energy transfer from a virtual photon to the target nucleon, y

$$y = \frac{\mathbf{p}\cdot\mathbf{q}}{\mathbf{p}\cdot\mathbf{k}}. \tag{2.6}$$

The process separates into a calculable "hard" sub–process from the "soft" non–calculable part which parameterises the structure of the nucleon. This separation of sub-processes is known as "factorisation".

This gives rise to two structure functions, f_1 and g_1, which depend on the fraction of the nucleon's momentum carried by the struck quark, x. The structure functions $f_1(x)$ and $g_1(x)$ are related to the unpolarised and polarised x-momentum distribution of the partons $q(x)$ and $\Delta q(x)$, respectively. The latter are called Parton Distribution Functions PDFs. The relationship is given by

$$f_1(x) = \frac{1}{2}\sum_q e_q^2 q(x) \text{ and} \tag{2.7}$$

$$g_1(x) = \frac{1}{2}\sum_q e^2 \Delta q(x) \tag{2.8}$$

where e_q^2 is the electrical charge of a quark ($q = u, d$ and s).

2.3 Exclusive Scattering

More generally, factorisation has been shown to hold in the Bjorken limit for hard exclusive processes as shown in References [11–13]. For exclusive processes, the hard scattering kernel can be calculated and the soft part is described by Generalised Parton Distributions (GPDs) as shown in Figure 2.3.

A quasi–free parton (most probably a quark at HERMES kinematics) is removed from the nucleon with a longitudinal momentum fraction of $x+\xi$. The struck parton is absorbed with a momentum fraction $x-\xi$. The parton radiates a real photon with

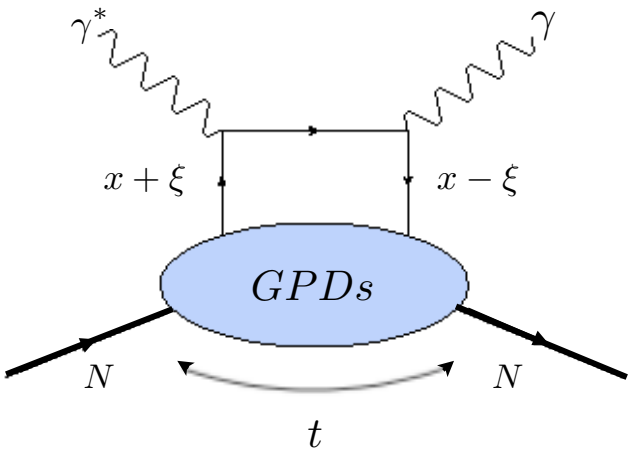

Figure 2.3: Non forward Compton amplitude appearing in DVCS

four–momentum $\mathbf{q}'$. The target nucleon remains intact through out the process.

The skewness, ξ, is half the difference of the longitudinal momentum fractions of quarks with respect to the nucleon momentum between the initial and final states. This is related to x_B as

$$\xi \approx \frac{x_B(1+\frac{t}{2Q^2})}{2-x_B+x_B\frac{t}{Q^2}}. \tag{2.9}$$

2.4 Generalised Parton Distributions

GPDs depend on four kinematic variables: x, ξ, Q^2 and t. The dependence on Q^2 is omitted in the following discussion as it is expected to be driven by Q^2 evolution, which is calculable from the Altarelli–Parisi equations [14–17].

For spin-1/2 nucleons, there are four leading twist quark-chirality conserving GPDs for each quark flavour q written, H^q, E^q, $\tilde{H}^q$ and $\tilde{E}^q$. The GPDs H^q and $\tilde{H}^q$ conserve nucleon helicity and E^q and $\tilde{E}^q$ are associated with a helicity flip of the nucleon.

In this thesis GPDs will be considered at leading twist (twist–2), where twist is defined as the dimension–spin of the operator defining the GPD [18]. The twist term is also identified with its suppression in orders of M_N/Q.

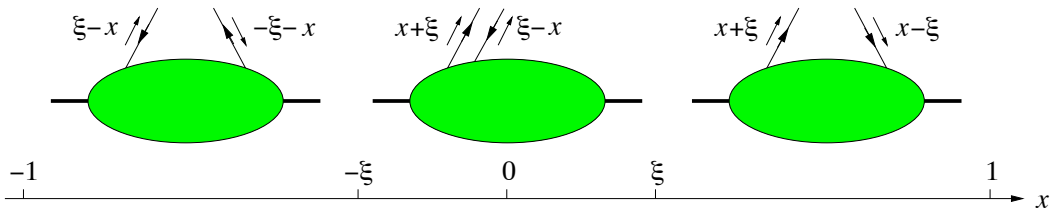

Figure 2.4: Partonic interpretation of GPDs in x and ξ. [5]

2.4.1 Physical Interpretations of GPDs

The physical interpretation of GPDs depends on the kinematic region considered. Three kinematic regions are considered as shown in Figure 2.4 and described below:

- $x \in (\xi, 1]$: the momentum fractions $x + \xi$ and $x - \xi$ are positive, and describe the emission and reabsorption of a quark.
- $x \in (-\xi, \xi)$: $x + \xi$ is positive and $x - \xi$ is negative, which is characterised by the removal of an antiquark pair.
- $x \in [-1, -\xi)$: emission and reabsorption of antiquarks.

The second region is referred to as the ERBL(Efremov-Radyushkin-Brodsky-Lepage) region based on evolution equations described in Refs [19,20], and the other two are described in the DGLAP(DokshitzerGribovLipatovAltarelliParisi) region. More details on the evolution of GPDs in leading order can be found in Refs [4, 21, 22].

2.4.2 Constraints on GPDs

2.4.2.1 Constraints from Elastic Scattering

At finite momentum transfer, the first moments of the GPDs relate to the elastic form factors [4]:

$$\int_{-1}^{+1} dx H^q(x,\xi,t) = F_1^q(t), \tag{2.10}$$

$$\int_{-1}^{+1} dx \tilde{H}^q(x,\xi,t) = F_2^q(t), \tag{2.11}$$

$$\int_{-1}^{+1} dx E^q(x,\xi,t) = G_A(t), \tag{2.12}$$

$$\int_{-1}^{+1} dx \tilde{E}^q(x,\xi,t) = G_P(t), \tag{2.13}$$

where F_1, F_2, G_A and G_P are the Dirac, Pauli, axial and pseudoscalar parton FFs of the nucleon discussed in Section 2.1. The relation between GPDs and FFs gave rise to the idea that the t dependence of the GPDs could be related via a Fourier transform to the transverse spatial distribution of quarks in the nucleon.

2.4.2.2 Constraints from DIS

In the forward limit ($t \to 0$ and $\xi = 0$), helicity conserving GPDs reduce to PDFs. For spin–1/2 nucleons [4, 11] these relationships are

$$H^q(x,0,0) = q(x), \tag{2.14}$$

$$\tilde{H}^q(x,0,0) = \Delta q(x) \tag{2.15}$$

where $q(x)$ is the longitudinal distribution of quarks of flavour q in the nucleon. GPDs E and $\tilde{E}$ are not considered here as they cannot be accessed in the forward limit.

2.4.2.3 Polynomiality

The non-trivial property of the x moments of GPDs called polynomiality is due to Lorentz invariance. This condition states that the Mellin moments of GPDs should

be polynomials of highest order $N+1$. This implies [23] for N odd:

$$\int_{-1}^{1} dx\, x^N\, H^q(x,\xi) = h_0^{q(N)} + h_2^{q(N)}\xi^2 + ... + h_{N+1}^{q(N)}\xi^{N+1}, \tag{2.16}$$

and for N even,

$$\int_{-1}^{1} dx\, x^N\, H^q(x,\xi) = h_0^{q(N)} + h_2^{q(N)}\xi^2 + ... + h_{N+1}^{q(N)}\xi^{N}, \tag{2.17}$$

and similarly for GPD E. The equation only contains even powers of ξ due to the time reversal invariance ($H(x,-\xi,t) = H(x,\xi,t)$). For GPD E the coefficients are related to the coefficients of GPD H as [24]

$$e_{N+1}^{q(N)} = -h_{N+1}^{q(N)}. \tag{2.18}$$

For GPDs $\tilde{H}$ and $\tilde{E}$ the maximum power in equation 2.16 is N rather than $N+1$. The maximum power comes from the properties of Fourier transforms [25].

2.4.3 Physical Interpretation of GPDs

2.4.3.1 Impact parameter space

From the relation between GPDs and Form Factors, the GPDs can also be linked to the spatial distribution of partons in the nucleon [26] for $\xi = 0$. For GPD H^q:

$$q^f(x,b_\perp) = \int \frac{d^2\Delta_\perp}{(2\pi)^2} \exp^{ib_\perp \Delta_\perp} H^f(x,\delta_\perp^2). \tag{2.19}$$

Where $\Delta_\perp$ is the transverse component of the nucleon momentum transfer, and $b_\perp$ indicates the position in the transverse plane. This interpretation allows for three–dimensional "images" of the nucleon, where the third dimension is the longitudinal momentum fraction of the nucleon carried by the parton under investigation. Plots of the spatial distribution of quarks in a nucleon have been produced in, for example, Ref [27] from GPD models. For small x, a very broad distribution is observed while, at large x, the distribution becomes more focussed on the centre of momentum of the nucleon.

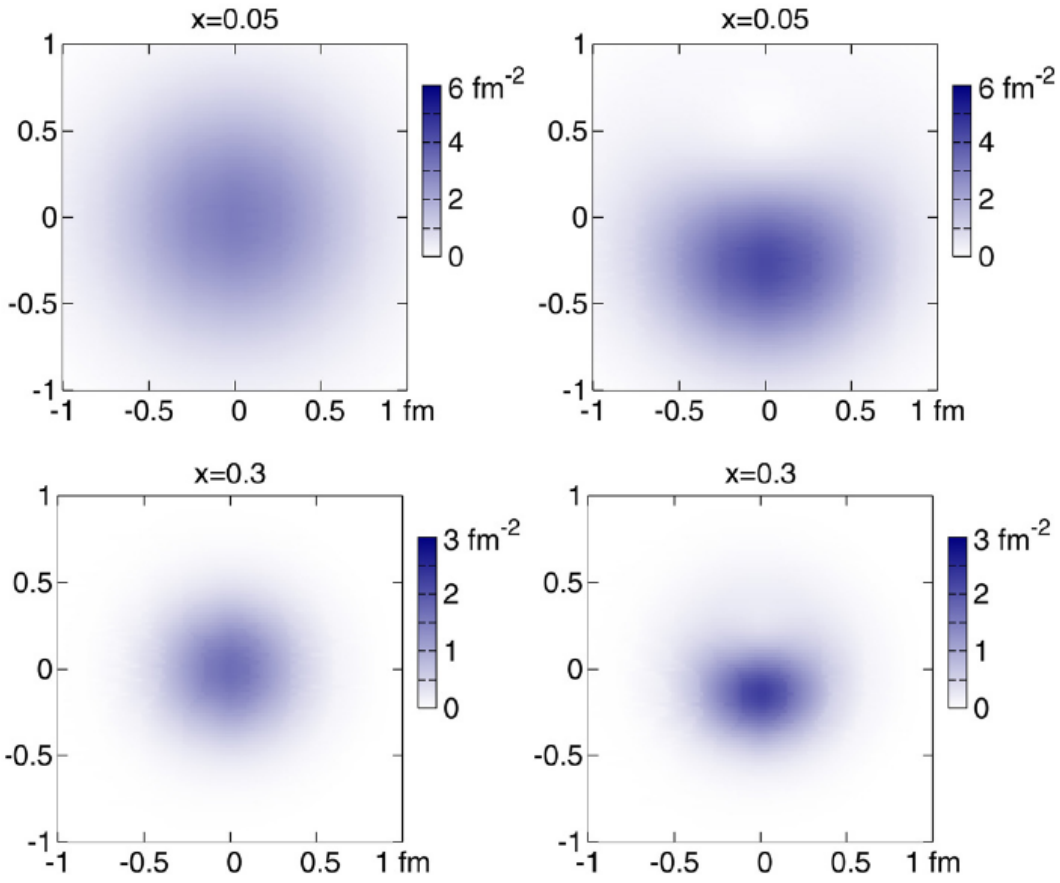

Figure 2.5: The u (left) and d (right) quark densities in impact parameter space. The longitudinal momentum fraction x is set to 0.05 (top) and 0.3 (bottom) [28].

2.4.3.2 Quark angular momentum

In 1996, it was shown by Ji [4] that there is a relation between the second moment of the sum of the unpolarised quark GPDs H^q and E^q in the limit of $t \to 0$ and the angular momentum J_q for each quark flavour q. This is commonly referred to as Ji's relation, and expressed as

$$J_q = \frac{1}{2} \lim_{t \to 0} \int_{-1}^{+1} (H^q(x, \xi, t) + E^q(x, \xi, t)) x dx.$$

Ji's relation is also valid for gluons.

The spin of nucleon can be expressed as the sum

$$\frac{1}{2} = J_q + J_g, \tag{2.20}$$

where J_g is the total angular momentum of gluons. This implies that once, J_q, has been measured, J_g can be deduced. The total angular momentum of quarks J_q can be decomposed in certain gauges into the sum of quark angular momentum L_q and the sum of their spins, $\Delta\Sigma$. Since $\Delta\Sigma$ has been measured (e.g. see Reference [2]), L_q would be able to be deduced once J_q was accessed via GPDs.

2.5 GPD Parameterisation and Models

One solution to parameterise the GPDs while satisfying the the polynomiality condition is to use Double - Distributions. These distributions were introduced by Radyushkin [11]and Mueller [21] and discussed further in Ref [22]. Considering a GPD $F^q(x,\xi,t)$ and a double distribution $F(\beta,\alpha,t)$:

$$F^q(x,\xi,t) = \int_{-1}^{1} d\beta \int_{-1+|\beta|}^{1-|\beta|} d\alpha \delta(\beta + \alpha\xi - x) f(\beta,\alpha,t). \tag{2.21}$$

To complete the parameterisation the D–term is introduced:

$$F^q(x,\xi,t) = \int_{-1}^{1} d\beta \int_{-1+|\beta|}^{1-|\beta|} d\alpha \delta(\beta + \alpha\xi - x) f(\beta,\alpha,t) + \theta\left[1 - \frac{x^2}{\xi^2}\right] D^q\left(\frac{x}{\xi}t\right). \tag{2.22}$$

The contribution of the D–term to GPDs H and E are of the same magnitude, but opposite sign. The D–term now generates the highest power of ξ:

$$\int_{-1}^{1} dx\, z^N\, D^q(z) = h^{q(N)}_{N+1} = -e^{q(N)}_{N+1}. \tag{2.23}$$

2.5.1 VGG model

The most commonly used model is by Vanderhaegen, Guichon and Guidal [29]. The model is based on the double distribution formalism and satisfies the theoretical constraints discussed in Section 2.4.2.

The parameterisation of GPD H first considers the t–independent part of double distributions discussed in Reference [22], expressed as

$$f^q(\beta,\alpha) = h(\beta,\alpha)q(\beta). \tag{2.24}$$

in terms of a PDF $q(\beta)$ which for positive values of β corresponds to a quark PDF and negative for an antiquark PDF. The function $h(\beta, \alpha)$ is parameterised through a one-parameter ansatz [22]. This is characterised by the impact parameter b, which describes the dependence of the GPD on the skewness ξ. It is a free parameter for both valence and sea quarks contributions which needs to be determined from experimental data. The case where $b \to \infty$ corresponds to the skewness dependence of the GPD vanishing, and reduces the GPD to the parton density. The VGG model considered in this thesis uses the quark distributions were taken from [30], however the results for the valence region are similar when using other parameterisations.

The parameterisation of the t dependence was taken from two different approaches. The simplest is known as the factorised ansatz where the GPDs satisfy the forward limit requirements for u and d quark distributions. This essentially reduces the t dependence of the GPD to the Form–Factor.

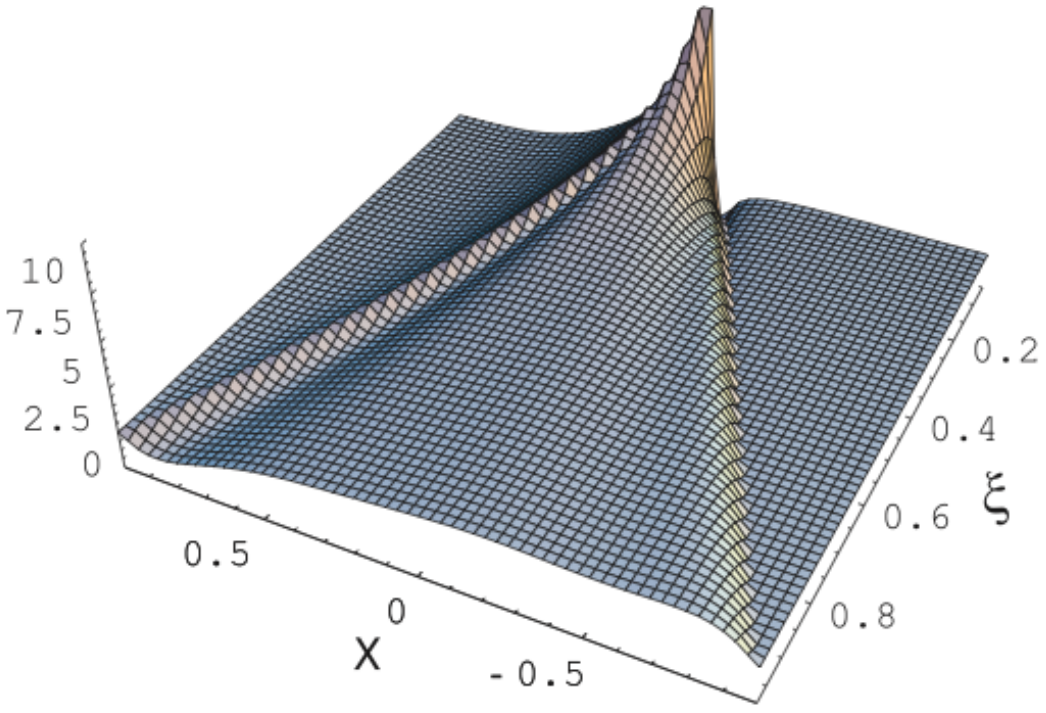

Figure 2.6: The x and ξ dependence of GPD H.

The second approach uses a phenomenological Regge–motivated ansatz. This is determined from the cross-section measurements of hadron-hadron reactions [31]. The Regge ansatz entangles the t–dependence of the GPD with the x and ξ depen-

dencies. This ansatz uses a Regge type parameterisation for the double distributions which $\propto |\xi| - \alpha(0) + \alpha' |t|$ where $\alpha' = 0.8\text{GeV}^2$.

Figure 2.6, from [24], shows an example of the x and ξ dependence of GPD H.

2.5.2 KM Model

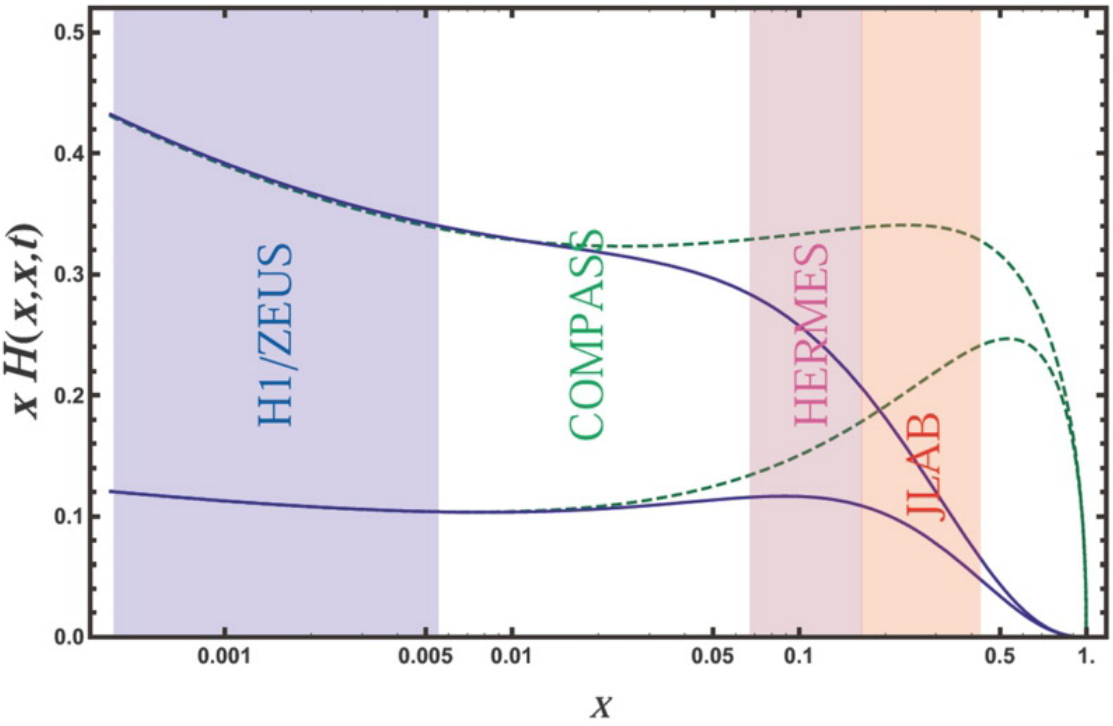

Figure 2.7: Global fit of GPD H [32]. Fits include dat from only HERMES and Hall B, Jefferson Lab data (dashed line), and the second also including Hall A measurements (full line).

A more recent model, which will be compared to the final result of this work, is a "dual" representation of GPDs by Kumericki and Mueller, labelled "KM" [32]. The authors of this model take Deeply Virtual Compton Scattering (DVCS) cross section measurements from the collider experiments at H1 and ZEUS, to set up the GPD model at small x_B. The cross section data was described by using a partial wave interpretation and assuming weakly entangled skewness and t dependencies, with a Regge inspired t dependence. The behaviour at small x_B from the fit of the cross section data was then included in a double distribution representation of GPDs, and the model was fitted to measurements from HERMES and Jefferson Lab. The resulting models, one including only HERMES and Hall B, Jefferson Lab data

(dashed line), and the second also including Hall A measurements (full line) have been used to extract GPD H across a range in x as shown in Figure 2.7.

2.5.3 GGL Model

Another recent model by Goldstein, Gonzalez-Hernandez and Liuti , labeled here as "GGL", is described in Ref [33]. This model also attempts a flexible parameterisation of a GPD model. It begins by considering a diquark model of nucleon. Data from global fits to FF and PDF measurements are then used to constrain the model from the known limits discussed in Section 2.4.2. Additional information is then included for higher moments of GPDs from lattice QCD calculations. In order to describe the t–dependence in the low–x region a Regge term is included. The skewness dependence is then included by fitting DVCS data from Jefferson Lab, before the model can be used to describe data at different kinematics by applying pQCD (perturbative Quantum Chromo Dynamics) evolution.

Figure 2.8 shows GPD H for this model evaluated at $Q^2 = 2\,\mathrm{GeV}^2$ versus x and different values of ζ, where $\zeta \approx x_B$. Here ζ is used instead of ξ to denote the skewness.

2.6 Accessing GPDs Experimentally

There are several processes by which GPDs can be accessed experimentally

- Deeply Virtual Compton Scattering : $\gamma^* N \to \gamma N'$, the hard exclusive lepton production of a real photon.
- Time like Compton Scattering : $\gamma N \to \gamma^* N'$, the production of lepton–antilepton pairs from the produced virtual photon.
- Double Deeply Virtual Compton Scattering : $\gamma^* N \to \gamma^* N'$, where again the produced virtual photon again decays into a lepton-antilepton pair.
- Deeply Virtual Meson Production : $lN \to lNM$, the exclusive lepton production of a neutral meson $M = \rho, \omega\pi...$

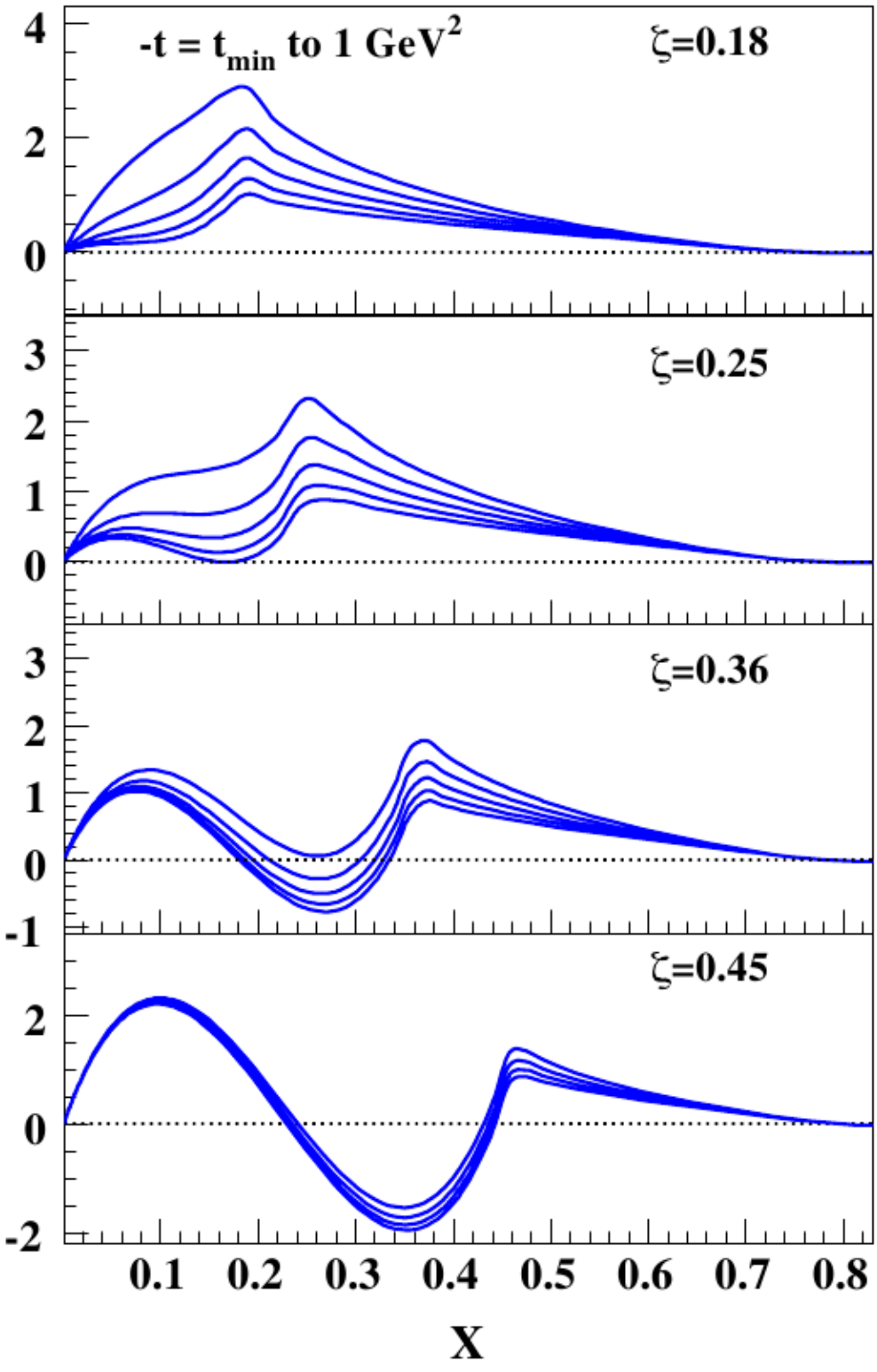

Figure 2.8: GPD H_u evaluated at $Q^2 = 2GeV^2$ vs x and different values of ζ [33].

Of the above processes, DVCS and DVMP are the only processes that have been used to constrain GPDs so far. This thesis will concentrate solely on DVCS from

here on.

2.7 Deeply Virtual Compton Scattering

Deeply Virtual Compton Scattering (DVCS) is theoretically the simplest process to access GPDs, as it has a single hadron in the final state. For the one–photon exchange approximation, DVCS can be represented by:

$$e(\mathbf{k})p(\mathbf{p}) \rightarrow e(\mathbf{k}')p(\mathbf{p}')\gamma(\mathbf{q}') \tag{2.25}$$

where $\mathbf{k}(\mathbf{k}')$ and $\mathbf{p}(\mathbf{p}')$ represent the four momenta of the incoming (scattered) lepton and the target (recoiling) proton respectively. In this process a virtual photon with four momentum $\mathbf{q}$ couples to a nucleon as the incoming lepton Compton scatters off a quasi–free parton in the nucleon. The hand–bag diagram for the leading order DVCS process is shown in Fig. 2.9.

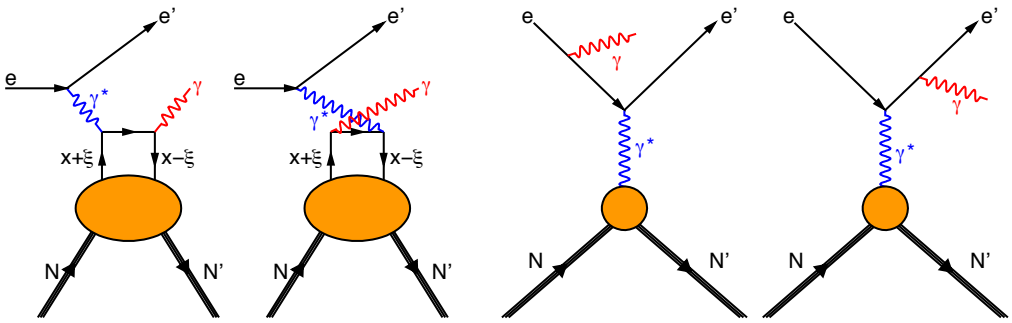

(a) DVCS (b) Bethe-Heitler

Figure 2.9: (a): The DVCS process (b): The Bethe–Heitler process.

The figure also shows the leading-order diagrams for the Bethe–Heitler process. Here, a real photon is emitted from either the incoming or scattered lepton. This process is completely calculable in QED (Quantum Electro Dynamics) [34].

Both processes are considered in the single–photon exchange approximation. The kinematic variables used for DIS (Section 2.2) are also used to describe DVCS. The

four–fold cross section for the DVCS process is [34]

$$\frac{d\sigma}{dx_B dQ^2 d|t| d\phi} = \frac{x_B e^6 |\tau|^2}{32(2\pi)^2 Q^4 \sqrt{1+\epsilon^2}} \tag{2.26}$$

where ϕ is the azimuthal angle between the lepton–scattering and photoproduction planes (Figure 2.10), e is the elementary charge, and the kinematic variable $\epsilon = 2x_B \frac{M_N}{Q}$. The amplitude τ is the coherent sum of DVCS and BH scattering amplitudes, τ_{DVCS} and τ_{BH} respectively,

$$|\tau|^2 = |\tau_{BH}|^2 + |\tau_{DVCS}|^2 + I \tag{2.27}$$

with the interference term

$$I = \tau_{DVCS}\tau^*_{BH} + \tau^*_{DVCS}\tau_{BH} \tag{2.28}$$

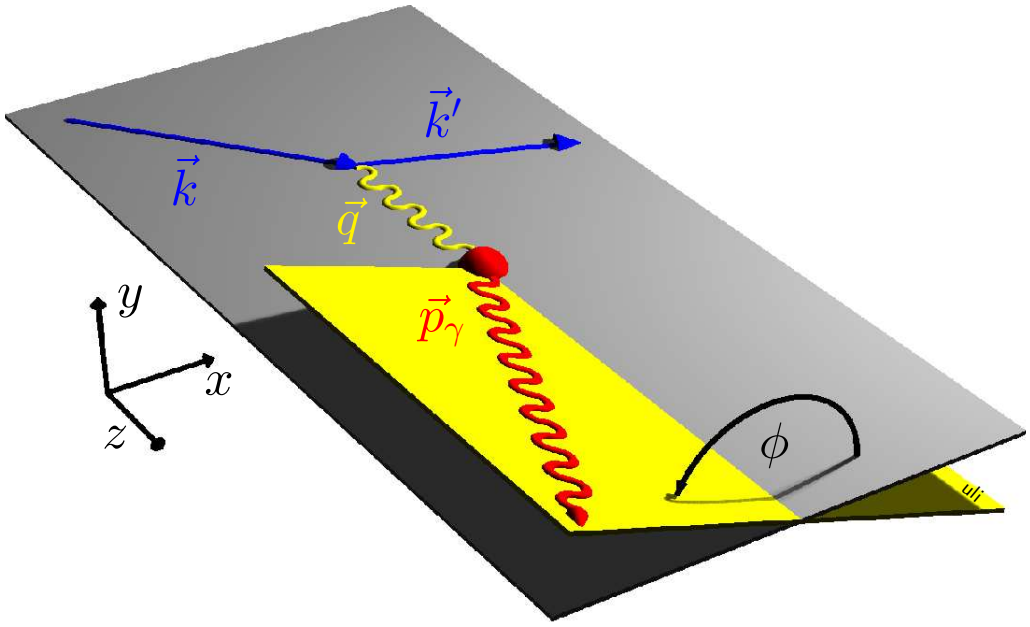

Figure 2.10: Definition of the azimuthal angle ϕ between the lepton scattering plane and the photon production plane.

The BH process dominates at HERMES kinematics. However, it is still possible to study DVCS via the interference term, I. The components of $|\tau|^2$ can be expanded

as a Fourier series in ϕ as [34]

$$|\tau_{BH}|^2 = \frac{K_{BH}}{P_1(\phi)P_2(\phi)} \sum_{n=0}^{2} c_n^{BH} \cos(n\phi), \tag{2.29}$$

$$|\tau_{DVCS}|^2 = K_{DVCS}\left(\sum_{n=0}^{2} c_n^{DVCS} \cos(n\phi) + \sum_{n=1}^{2} s_n^{DVCS} \sin(n\phi) \right), \tag{2.30}$$

$$I = \frac{e_l K_I}{P_1(\phi)P_2(\phi)} (\sum_{n=0}^{3} c_n^{I} \cos(n\phi) + P_l \sum_{n=1}^{3} \sin(n\phi)), \tag{2.31}$$

where e_l is the charge of the lepton beam in terms of the elementary charge and the terms K_{BH}, K_{DVCS} and K_I are the kinematic factors

$$K_{BH} = \frac{1}{x_B^2 t(1+\epsilon^2)^2}, \tag{2.32}$$

$$K_{DVCS} = \frac{1}{Q^2}, \tag{2.33}$$

$$K_I = \frac{1}{x_B y^3 t}. \tag{2.34}$$

The ϕ dependent lepton propagators of the BH process $P_1(\phi)$ and $P_2(\phi)$ are expressed as

$$P_1(\phi) = (\mathbf{k} - \mathbf{q}')^2 = -\frac{J + K\cos\phi}{y(1+\epsilon^2)}, \tag{2.35}$$

$$P_2(\phi) = (\mathbf{k}' + \mathbf{q}')^2 = 1 + \frac{t}{Q^2} - P_1(\phi), \tag{2.36}$$

where K is a $\frac{\sqrt{-t}}{Q}$ suppressed kinematic factor and J is given by

$$J = \left(1 - y - \frac{y\epsilon^2}{2}\right)\left(1 + \frac{t}{Q^2}\right) - (1 - x_B)(2 - y)\frac{t}{Q^2}, \tag{2.37}$$

To measure an absolute cross section, a precise knowledge of the luminosity of the experiment is needed. Alternatively, ratios of different cross sections are measured as asymmetries where acceptance effects should cancel and precise knowledge of absolute luminosity is not essential to the result.

2.7.1 Beam Helicity Asymmetry

The observable extracted in this thesis is the single charge beam helicity asymmetry from an unpolarised hydrogen target. The cross section that is independent of beam helicity, i.e. with an unpolarised beam (U), an unpolarised target (U) and constant charge, is expressed as [34]

$$\begin{aligned}\sigma_{UU}(\phi) &= \frac{\alpha^3}{8\pi Q^2 x_B y(1-\epsilon^2)^{5/2} t P_1(\phi) P_2(\phi)}[c_0^{BH} + \sum_{n=1}^{2} c_n^{BH}\cos(n\phi)] \\ &+ \frac{\alpha^3 x_B}{8\pi y Q^4\sqrt{1+\epsilon^2}}[c_0^{DVCS} + \sum_{n=1}^{2} c_b^{DVCS}\cos(n\phi)] \\ &- \eta\frac{\alpha^3}{8\pi Q^2\sqrt{1+\epsilon^2} y^2 t P_1(\phi) P_2(\phi)}\left[c_0^I + \sum_{n=1}^{3} c_n^I\cos(n\phi)\right]. \end{aligned} \tag{2.38}$$

The cross section that is dependent on the longitudinally polarised beam (L) and an unpolarised target (U) is

$$\begin{aligned}\sigma_{LU}(\phi) &= \frac{\alpha^3}{8\pi Q^2 x_B y(1-\epsilon^2)^{5/2} t P_1(\phi) P_2(\phi)}[c_0^{BH} + \sum_{n=1}^{2} c_n^{BH}\cos(n\phi)] \\ &+ \frac{\alpha^3 x_B}{8\pi y Q^4\sqrt{1+\epsilon^2}}[c_0^{DVCS} + \sum_{n=1}^{2} c_b^{DVCS}\cos(n\phi) - \lambda s_1^{DVCS}\sin(\phi)] \\ &- \eta\frac{\alpha^3}{8\pi Q^2\sqrt{1+\epsilon^2} y^2 t P_1(\phi) p_2(\phi)}[c_0^I + \sum_{n=1}^{3} c_n^I\cos(n\phi) + \lambda\sum_{n=1}^{2} s_n^I\sin(n\phi)]. \end{aligned} \tag{2.39}$$

The cross section σ_{LU} can be expressed as

$$\sigma_{LU} = \sigma_{UU}\left[1 + \lambda\left(K_1\frac{s_1^{DVCS}\sin(\phi)}{\sigma_{UU}} - \eta K_2\frac{\sum_{n=1}^{2} s_b^I\sin(n\phi)}{\sigma_{UU}}\right)\right], \tag{2.40}$$

where λ is the polarisation state, η is the charge, and K_1 and K_2 are the kinematic factors.

The Beam Helicity Asymmetry, A_{LU} is calculated as the difference in cross sections of different beam helicity states for an unpolarised beam with a constant charge

$$A_{LU}^{\eta}(\phi) = \frac{\overrightarrow{\sigma}(\phi) - \overleftarrow{\sigma}(\phi)}{\overrightarrow{\sigma}(\phi) + \overleftarrow{\sigma}(\phi)} \tag{2.41}$$

where $\overrightarrow{\sigma}$ and $\overleftarrow{\sigma}$ represent the positive and negative beam helicity states respectively.

The asymmetry can be expressed as

$$A_{LU}^{\eta}(\phi) = \frac{s_1^{DVCS} sin(\phi) - \eta \frac{1}{Z} \frac{x_B}{y} s_1^I sin(\phi) + s_2^I sin(2\phi)}{\frac{1}{Z} \frac{c_0^{BH} + \sum_{n=1}^{2} c^B H_n cos(n\phi)}{t(1+\epsilon^2)^2} + c_0^{DVCS} + \sum_{n=1}^{2} c_n^{DVCS} cos(n\phi) - \eta \frac{1}{Z} c_0^I + \sum_{n=1}^{3} c_n^I cos(n\phi)} \tag{2.42}$$

where

$$Z = \frac{x_B^2 P_1(\phi) P_2(\phi)}{Q^2}. \tag{2.43}$$

An analysis of the above expression for A_{LU} shows that the asymmetry contains the charge-dependent interference terms (s_1^I, s_2^I) and the charge-independent DVCS term (s_1^{DVCS}). In the denominator the c_0^{BH} is the leading term as BH dominates and the interference s_1^I term is expected to dominate the numerator due to the dipole nature of the Bethe–Heitler term.. The asymmetry can therefore be approximated by

$$A_{LU}(\phi) \approx \frac{x_B}{y} \frac{s_1^I}{c_0^{BH}} sin(\phi). \tag{2.44}$$

2.8 Compton Form Factors

Compton Form Factors (CFFs) provide the link between GPDs and the scattering amplitudes. CFFs $\mathcal{F}$ are convolutions of the corresponding GPD F with a hard scattering kernel

$$\mathcal{F}(\xi, t) = \sum_q e_q^2 \int_{-1}^{1} C^{\pm}(x, \xi) F^q(x, \xi, t) dx, \tag{2.45}$$

where the scattering kernels $C^{\pm}$ are complex functions, the superscript $+$ $(-)$ relates to CFFs $\tilde{\mathcal{H}}$ and $\tilde{\mathcal{E}}$ ($\mathcal{H}$ and $\mathcal{E}$). For each GPD the scattering kernels can be expressed as:

$$C^{\pm} = \frac{1}{x - \xi - i\epsilon} \pm \frac{1}{1 + \xi - i\epsilon} + O(\alpha), \tag{2.46}$$

where ϵ is a non–zero mathematical term that allows $C^{\pm}$ to exist when $x = \xi$. The CFFs can be split into its imaginary and real parts, i.e. to leading order:

$$Re(\mathcal{F}) = PV \int_{-1}^{1} dx \left(\frac{F}{x-\xi} \pm \frac{F}{x+\xi} \right), \tag{2.47}$$

$$Im(\mathcal{F}) = F(\xi,\xi) \pm F(\xi,-\xi) \tag{2.48}$$

where PV denotes a principle value integral.

DVCS observables can be written in terms of the real and imaginary parts of CFFs [34],

$$s_1^I = 8\lambda K y(2-y)\Im C^I(\mathcal{F}), \tag{2.49}$$

where the twist–2 approximation of the Fourier $\mathcal{C}$-function is

$$\mathcal{C}^I = F_1\mathcal{H} + \frac{x_B}{2-x_B}(F_1+F_2)\tilde{\mathcal{H}} - \frac{t^2}{4M^2}F_2\mathcal{E}. \tag{2.50}$$

At HERMES kinematics, the contributions from CFFs $\tilde{\mathcal{H}}$ and $\mathcal{E}$ can be neglected.

2.9 Previous HERMES DVCS results

HERMES has previously extracted a number of different asymmetries with dependencies on combinations of beam charge, beam helicity and target polarisation. These in turn relate to a number of different DVCS observables and relate to different GPDs. The first HERMES result was the Beam–Helicity Asymmetry (BHA) in [35] and a Beam Charge Asymmetry (BCA) [36] has since been superseded by more precise measurements from data taken using both beam charges [7, 9]. HERMES has also published measurements of asymmetry amplitudes with a transversely polarised target [6, 37], a longitudinally polarised target [8]. These results will be described in the following sections with their relations to GPDs.

The currently published data sets, however, have always included an average 12% contamination from BH/DVCS events with a resonant proton (Δ) in the final state.

The aim of this work was to extract BHA amplitudes free from the contamination

to see the if the contamination effected the resulting amplitudes. Comparing the results from this work enables the effect of the contamination on the extracted asymmetry amplitudes can be ascertained.

2.9.1 Simultaneous Extraction of the Beam Helicity and Charge Asymmetries

The simultaneous extraction allows for the separation of contributions from the DVCS and Interference parts of the cross section. The asymmetries $A_{\mathrm{LU}}^{\mathcal{I}}(\phi)$, $A_{\mathrm{LU}}^{\mathrm{DVCS}}(\phi)$ and $A_{\mathrm{C}}(\phi)$ are defined as

$$A_{\mathrm{LU}}(\phi)^{\mathcal{I}}(\phi) \equiv \frac{[\sigma^{\rightarrow+}(\phi)+\sigma^{\leftarrow-}(\phi)]-[\sigma^{\leftarrow+}(\phi)+\sigma^{\rightarrow-}(\phi)]}{[\sigma^{\rightarrow+}(\phi)+\sigma^{\leftarrow-}(\phi)]+[\sigma^{\leftarrow+}(\phi)+\sigma^{\rightarrow-}(\phi)]} \tag{2.51}$$

$$A_{\mathrm{LU}(\phi)}^{\mathrm{DVCS}}(\phi) \equiv \frac{[\sigma^{\rightarrow+}(\phi)+\sigma^{\rightarrow-}(\phi)]-[\sigma^{\leftarrow+}(\phi)+\sigma^{\leftarrow-}(\phi)]}{[\sigma^{\rightarrow+}(\phi)+\sigma^{\rightarrow-}(\phi)]+[\sigma^{\leftarrow+}(\phi)+\sigma^{\leftarrow-}(\phi)]} \tag{2.52}$$

$$A_{\mathrm{C}(\phi)} \equiv \frac{[\sigma^{\rightarrow+}(\phi)+\sigma^{\leftarrow+}(\phi)]-[\sigma^{\rightarrow-}(\phi)+\sigma^{\leftarrow-}(\phi)]}{[\sigma^{\rightarrow+}(\phi)+\sigma^{\leftarrow+}(\phi)]+[\sigma^{\rightarrow-}(\phi)+\sigma^{\leftarrow-}(\phi)]} \tag{2.53}$$

where the superscript $+$ $(-)$ denotes a positron (electron) beam. The results from the 1996-2007 HERMES hydrogen data set [7,9,38,39] are shown in Figures 2.11 and 2.12 integrated across the entire kinematic range and as a function of $-t$, x_B and Q^2. All the extracted asymmetry results are subject to a fractional contribution to the event sample from associated production, which is shown at the bottom of each figure.

The first and second harmonics of $A_{\mathrm{LU,I}}$ are sensitive to the interference in the scattering amplitude are shown in the first and third rows of Figure 2.11. The $A_{\mathrm{LU,I}}^{\sin\phi}$ term is the leading twist term, and is the largest of all the amplitudes extracted at over the entire kinematic range. No strong dependence is shown on $-t$, x_B or Q^2, however there is a dependence on $-t$ at low values. Both the $A_{\mathrm{LU,DVCS}}^{\sin\phi}$ and $A_{\mathrm{LU,I}}^{\sin(2\phi)}$ asymmetry amplitudes are consistent with zero, and neither show any dependence on $-t.$, x_B or Q^2.

The A_{C} harmonics are shown in Figure 2.12. The leading twist amplitudes $A_{\mathrm{C}}^{\cos(0\phi)}$ and $A_{\mathrm{C}}^{\cos(\phi)}$ are both non–zero. They are expected to be related as they

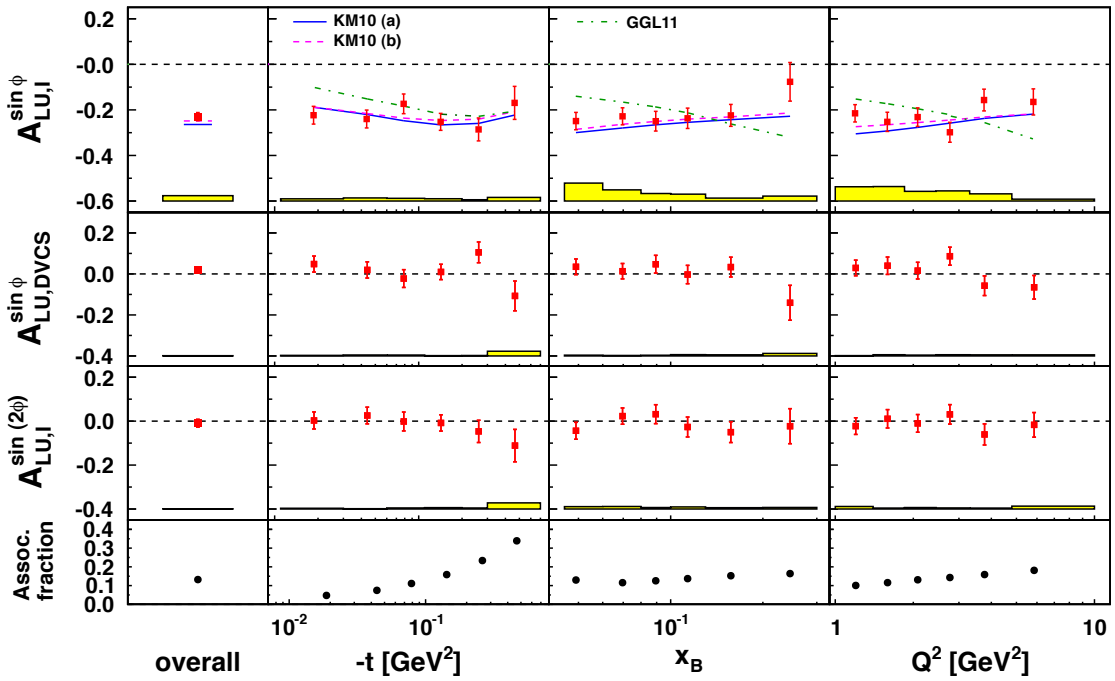

Figure 2.11: The $A_{\mathrm{LU,I}}^{\sin\phi}$, $A_{\mathrm{LU,DVCS}}^{\sin\phi}$ and $A_{\mathrm{LU,I}}^{\sin(2\phi)}$ beam–helicity asymmetry amplitudes extracted from all the hydrogen data recorded at HERMES from 1996 until 2007. The error bars (bands) represent the statistical (systematic) uncertainties. An additional 3.2 % scale uncertainty is present in the amplitudes due to the imprecision of the beam polarisation measurement. Solid and dashed lines show model calculations from [32]; calculations from Ref. [33] are shown as dashed-dotted lines. The bottom panel shows the fractional contribution from associated production to the yield in each kinematic bin estimated from a simulation.

depend on the same set GPDs, but there is a kinematic suppression of $A_{\mathrm{C}}^{\cos(0\phi)}$ with respect to $A_{\mathrm{C}}^{\cos(\phi)}$. The measured values are found to diverge with opposite sign from zero at increasing values of $-t$, but there is no real difference on their dependencies on x_B and Q^2. The $A_{\mathrm{C}}^{\cos(2\phi)}$ and $A_{\mathrm{C}}^{\cos(3\phi)}$ amplitudes are both consistent with zero and have no significant dependence on $-t$, x_B and Q^2. The $A_{\mathrm{C}}^{\cos(2\phi)}$ amplitude is related to the twist–3 GPDs and $A_{\mathrm{C}}^{\cos(3\phi)}$ relates to the gluon helicity–flip GPDs. Both of these amplitudes are expected to be suppressed at HERMES kinematics compared to the leading twist amplitudes.

These results are compared to theoretical calculations from the model described in Section 2.5.2 [32], shown as solid and dashed lines; calculations from the model described in Section 2.5.1 [33], shown as dashed-dotted lines.They both describe well the t–dependence of the leading twist amplitudes, and the KM models describe

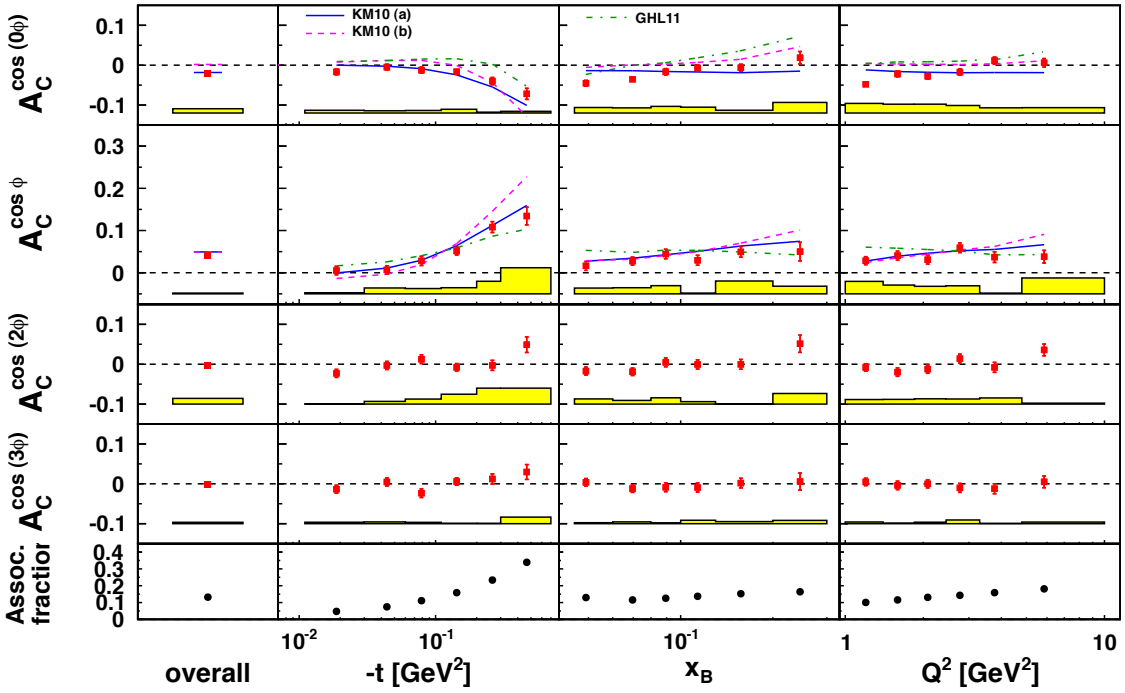

Figure 2.12: The $A_C^{\cos(0\phi)}$, $A_C^{\cos\phi}$, $A_C^{\cos(2\phi)}$ and $A_C^{\cos(3\phi)}$ beam-charge asymmetry amplitudes extracted from all the hydrogen data recorded at HERMES from 1996 until 2007. The error bars (bands) represent the statistical (systematic) uncertainties. Theoretical calculations from the model described in Ref. [32] are shown as solid and dashed lines; calculations from Ref. [33] are shown as dashed-dotted lines. The bottom panel shows the fractional contribution from associated production to the yield in each kinematic bin estimated from a simulation.

better the dependence on x_B and Q^2.

In summary, the leading twist amplitudes are dominated by contributions from the following CFFs, and therefore the corresponding GPDs:

$$A_{\mathrm{LU}}^{\mathcal{I}}(\phi) \propto Im[F_1\mathcal{H}], \tag{2.54}$$

$$A_{\mathrm{LU}}^{\mathrm{DVCS}}(\phi) \propto Im[\mathcal{H}\mathcal{H}^* + \tilde{\mathcal{H}}\tilde{\mathcal{H}}^*], \tag{2.55}$$

$$A_{\mathrm{C}} \propto Re[F_1\mathcal{H}]. \tag{2.56}$$

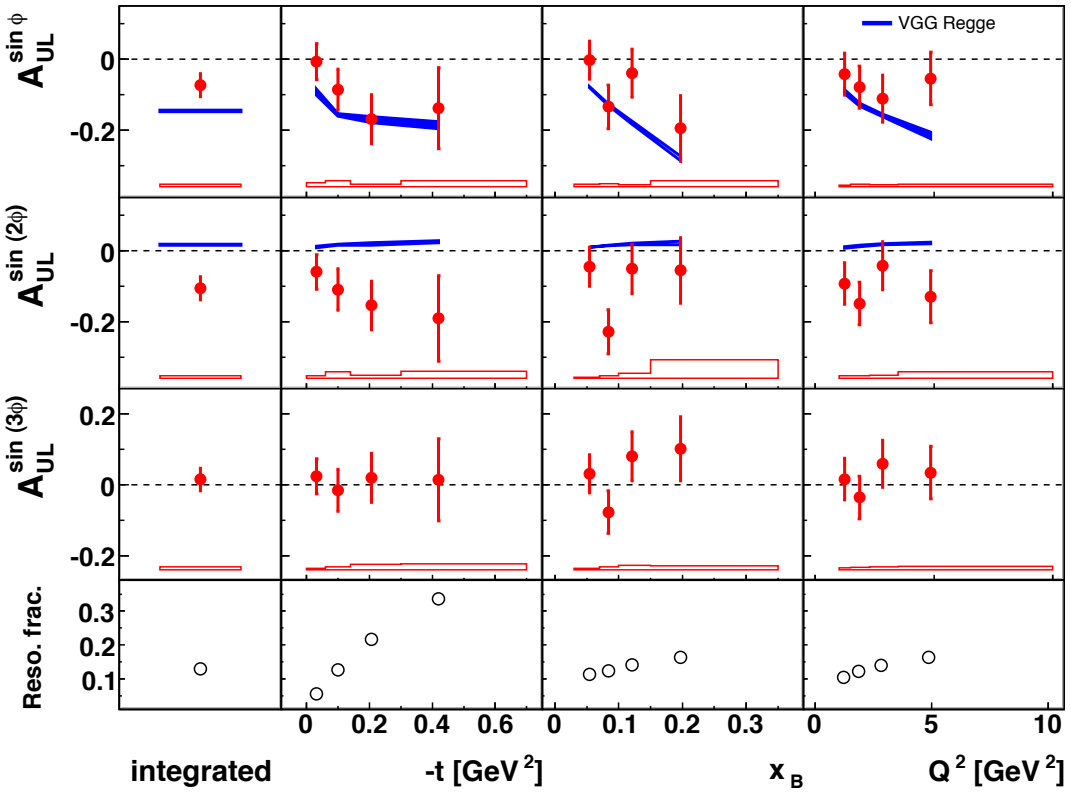

Figure 2.13: Longitudinal target-spin asymmetry amplitudes A_{UL} with positrons incident on a longitudinally polarised hydrogen target. The error bars show the statistical uncertainties and the open error bands show the systematic uncertainties and the solid blue bands represent the predictions from the "VGG Regge" GPD model described in Reference [29]. There is an estimated scale uncertainty of 4.2% due to the precision of the measurement of the target polarisation. The bottom panel shows the fractional contribution from associated production to the yield in each kinematic bin estimated from a simulation.

2.9.2 Extraction of the Longitudinal Target Spin Asymmetries

HERMES has published results [8, 40] of the extraction of longitudinal target spin asymmetries A_{UL} and A_{LL} which can be expressed as

$$A_{UL}(\phi) \equiv \frac{[\sigma^{\leftarrow\Rightarrow}(\phi)+\sigma^{\rightarrow\Rightarrow}(\phi)]-[\sigma^{\leftarrow\Leftarrow}(\phi)+\sigma^{\rightarrow\Leftarrow}(\phi)]}{[\sigma^{\leftarrow\Rightarrow}(\phi)+\sigma^{\rightarrow\Rightarrow}(\phi)]+[\sigma^{\leftarrow\Leftarrow}(\phi)+\sigma^{\rightarrow\Leftarrow}(\phi)]} \tag{2.57}$$

$$A_{LL}(\phi) \equiv \frac{[\sigma^{\rightarrow\Rightarrow}(\phi)+\sigma^{\leftarrow\Leftarrow}(\phi)]-[\sigma^{\leftarrow\Rightarrow}(\phi)+\sigma^{\rightarrow\Leftarrow}(\phi)]}{[\sigma^{\rightarrow\Rightarrow}(\phi)+\sigma^{\leftarrow\Leftarrow}(\phi)]-[\sigma^{\leftarrow\Rightarrow}(\phi)+\sigma^{\rightarrow\Leftarrow}(\phi)]} \tag{2.58}$$

The asymmetry amplitudes extracted are shown in Figures 2.13 and 2.14 inte-

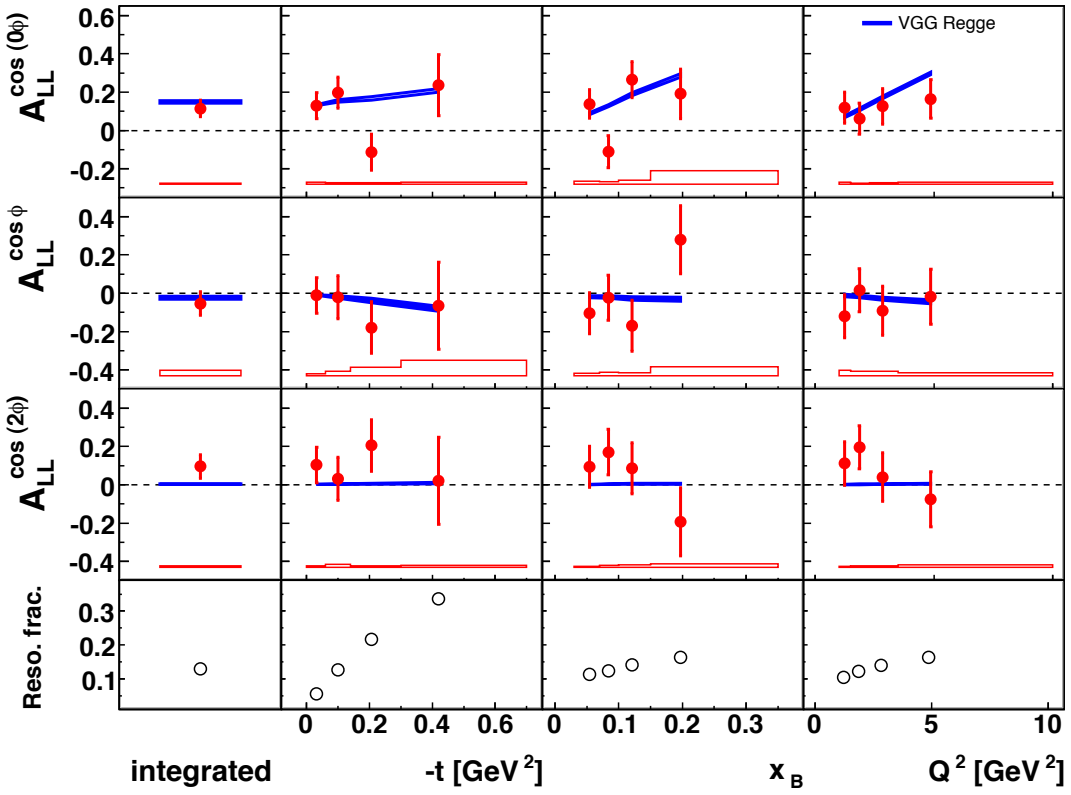

Figure 2.14: Longitudinal target-spin asymmetry amplitudes A_{LL} with positrons incident on a longitudinally polarised hydrogen target. The error bars show the statistical uncertainties and the open error bands show the systematic uncertainties and the solid blue bands represent the predictions from the "VGG Regge" GPD model described in Reference [29]. There is an estimated scale uncertainty of 5.3% due to the precision of the measurement of the target and beam polarisations. The bottom panel shows the fractional contribution from associated production to the yield in each kinematic bin estimated from a simulation.

grated over the entire kinematic range at HERMES and as a function of $-t$, x_B and Q^2. The results are presented alongside theory calculations based on Reference [29] and outlined above in Section 2.5.1. This model was used because at the time of publication it was the only model available and the KM model does not describe target spin asymmetries.

Figure 2.13 shows the amplitudes of $A_{UL}^{\sin(n\phi)}$ of the longitudinally polarised target-sin asymmetry. The leading twist term is the $A_{UL}^{\sin(\phi)}$,which is non–zero. The amplitude shows an increase with increasing $-t$, x_B and Q^2 in agreement with the model calculation. However due to the statistical precision of the measurements no strong conclusions can be drawn. The twist-3 amplitude $A_{UL}^{\sin(2\phi)}$ is observed to be

unexpectedly high.

Figure 2.14 shows the extracted amplitudes of $A_{LL}^{\cos(n\phi)}$ from the double spin asymmetry. The twist-2 amplitude $A_{LL}^{\cos(0\phi)}$ is non zero, and shows no strong dependence on $-t$,x_B or Q^2. As predicted the leading-twist term $A_{LL}^{\cos(\phi)}$ and twist 3 term $A_{LL}^{\cos(3\phi)}$ are consistent with zero.

These asymmetries are of interest because the leading twist amplitudes are related to

$$A_{UL}^{\sin(\phi)} \propto Im[\tilde{\mathcal{H}}], \tag{2.59}$$

$$A_{LL}^{\cos(\phi)} \propto Re[\tilde{\mathcal{H}}]. \tag{2.60}$$

These are the first results to provide access to both the real and imaginary parts of CFF $\tilde{\mathcal{H}}$.

2.9.3 Extraction of the Transverse Target Spin Asymmetries

HERMES has published results from the extraction of the transversely polarised target asymmetries which were extracted simultaneously with a BCA [6], shown in figure 2.15. The azimuthal asymmetries can be expressed as

$$A_{UT}^{\mathcal{I}}(\phi,\phi_s) \equiv \frac{[\sigma^+(\phi,\phi_s)+\sigma^-(\phi,\phi_s+\pi)]-[\sigma^-(\phi,\phi_s)+\sigma^+(\phi,\phi_s+\pi)]}{[\sigma^+(\phi,\phi_s)+\sigma^-(\phi,\phi_s+\pi)]+[\sigma^-(\phi,\phi_s)+\sigma^+(\phi,\phi_s+\pi)]}, \tag{2.61}$$

$$A_{UT}^{\mathrm{DVCS}}(\phi,\phi_s) \equiv \frac{[\sigma^+(\phi,\phi_s)+\sigma^-(\phi,\phi_s)]-[\sigma^-(\phi,\phi_s)+\sigma^+(\phi,\phi_s+\pi)]}{[\sigma^+(\phi,\phi_s)+\sigma^-(\phi,\phi_s)]+[\sigma^-(\phi,\phi_s)+\sigma^+(\phi,\phi_s+\pi)]}, \tag{2.62}$$

where ϕ_s is the azimuthal angle between the lepton-scattering plane and the transverse target polarisation vector. The amplitudes which are of particular interest are $A_{UT,\mathcal{I}}^{\sin\psi\cos\phi}$ and $A_{UT,\mathrm{DVCS}}^{\cos\psi\sin\phi}$, where $\psi = \phi - \phi_s$. These relate respectively to the CFFs as:

$$A_{UT,\mathrm{DVCS}}^{\cos\psi\sin\phi} \propto Im[F_2\mathcal{H} - F_1\mathcal{E}], \tag{2.63}$$

$$A_{UT,\mathcal{I}}^{\sin\psi\cos\phi} \propto Im[F_2\tilde{\mathcal{H}} - F_1\xi\mathcal{E}]. \tag{2.64}$$

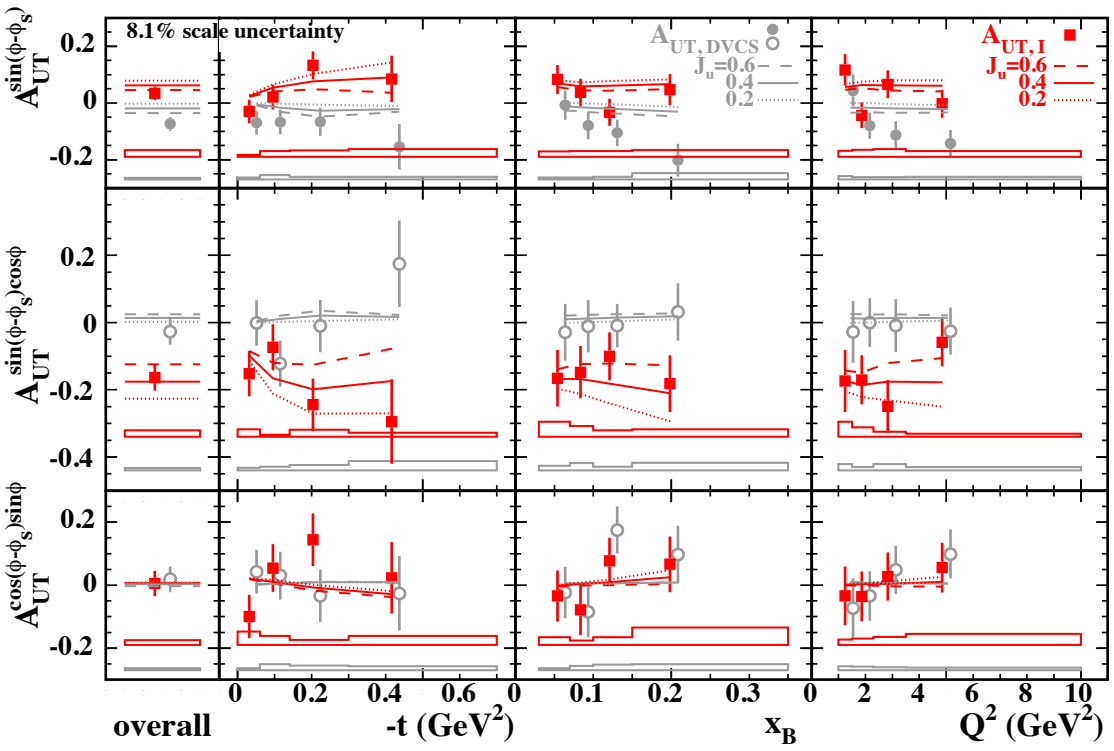

Figure 2.15: The transverse target spin asymmetry amplitudes A_{UT} with a hydrogen target. The error bars show the statistical uncertainties and the error bands show the systematic uncertainties. There is additional scale uncertainty of 8.1% due to the precision of the target polarisation measurement. Also shown are model calculations from the GPD model [29] for certain values of J_u with $J_d = 0$.

These are of interest because they provide the best access to GPD E and it's corresponding CFF.

HERMES also published double spin asymmetries from a transversely polarised target measured with respect to target polarisation combined with beam helicity and beam charge, and with respect to target polarisation combined with beam helicity alone. Here azimuthal asymmetries can be expressed as (due to space the ϕ has been omitted here from the right hand side)

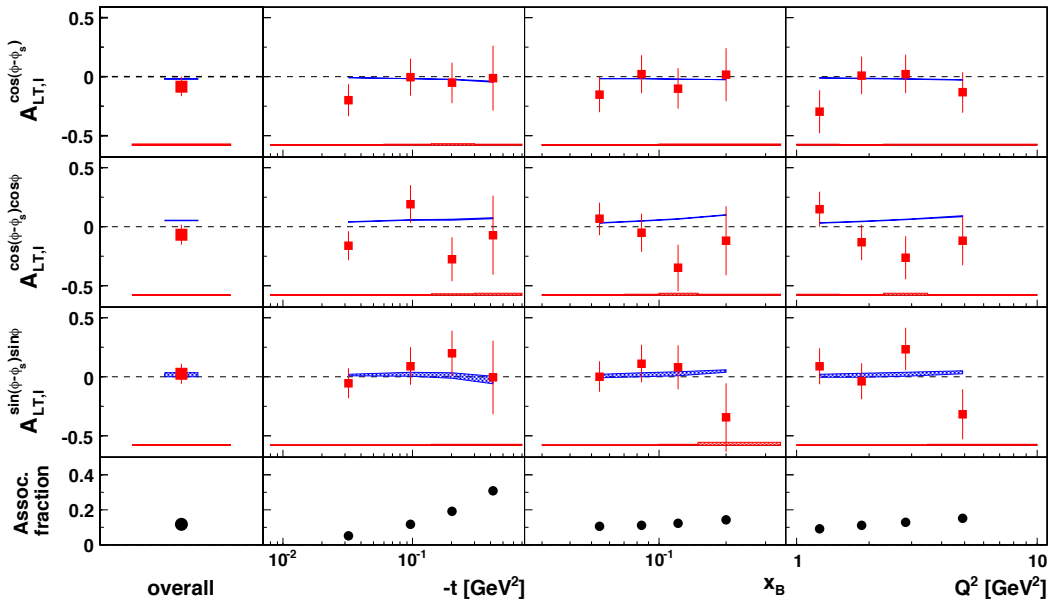

Figure 2.16: The transverse target spin asymmetry amplitudes A_{LT} with a hydrogen target. The error bars show the statistical uncertainties and the error bands show the systematic uncertainties. There is additional scale uncertainty of 8.6% due to the precision of the beam and target polarisation measurements. Also shown are model calculations from the GPD model [29].The bottom panel shows the fractional contribution from associated production to the yield in each kinematic bin estimated from a simulation.

$$A_{LT}^{\mathcal{I}}(\phi,\phi_s) \equiv \frac{[\sigma^{\rightarrow+\Uparrow}+\sigma^{\leftarrow+\Downarrow}-\sigma^{\rightarrow+\Downarrow}-\sigma^{\leftarrow+\Uparrow}]-[\sigma^{\rightarrow-\Uparrow}+\sigma^{\leftarrow-\Downarrow}-\sigma^{\rightarrow-\Downarrow}-\sigma^{\leftarrow-\Uparrow}]}{[\sigma^{\rightarrow+\Uparrow}+\sigma^{\leftarrow+\Downarrow}+\sigma^{\rightarrow+\Downarrow}+\sigma^{\leftarrow+\Uparrow}]+[\sigma^{\rightarrow+\Uparrow}+\sigma^{\leftarrow+\Downarrow}+\sigma^{\rightarrow+\Downarrow}+\sigma^{\leftarrow+\Uparrow}]}, \tag{2.65}$$

$$A_{LT}^{\mathrm{DVCS}}(\phi,\phi_s) \equiv \frac{[\sigma^{\rightarrow+\Uparrow}+\sigma^{\leftarrow+\Downarrow}-\sigma^{\rightarrow+\Downarrow}-\sigma^{\leftarrow+\Uparrow}]+[\sigma^{\rightarrow-\Uparrow}+\sigma^{\leftarrow-\Downarrow}-\sigma^{\rightarrow-\Downarrow}-\sigma^{\leftarrow-\Uparrow}]}{[\sigma^{\rightarrow+\Uparrow}+\sigma^{\leftarrow+\Downarrow}+\sigma^{\rightarrow+\Downarrow}+\sigma^{\leftarrow+\Uparrow}]+[\sigma^{\rightarrow+\Uparrow}+\sigma^{\leftarrow+\Downarrow}+\sigma^{\rightarrow+\Downarrow}+\sigma^{\leftarrow+\Uparrow}]}. \tag{2.66}$$

The amplitudes of particular interest are the $A_{LT}^{\cos(\phi-\phi_s)\cos\phi}$ and $A_{LT}^{\sin(\phi-\phi_s)\sin\phi}$ for both the charge difference and charge average asymmetries. These also provide access to GPD E and are related to CFFs as

$$A_{LT,\mathcal{I}}^{\cos(\phi-\phi_s)\cos\phi} \propto Re[F_2\tilde{\mathcal{H}}-(F_1+\xi F_2)\tilde{\mathcal{E}}], \tag{2.67}$$

$$A_{LT,\mathcal{I}}^{\sin(\phi-\phi_s)\sin\phi} \propto Re[F_2\mathcal{H}-F_1\mathcal{E}], \tag{2.68}$$

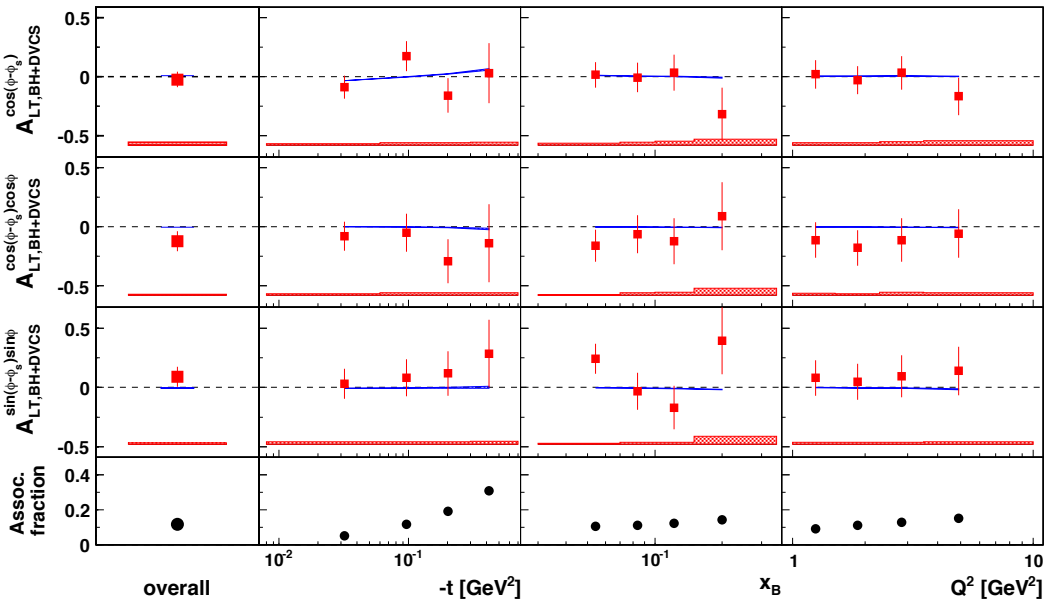

Figure 2.17: The transverse target spin asymmetry amplitudes A_{LT} with a hydrogen target. The error bars show the statistical uncertainties and the error bands show the systematic uncertainties. There is additional scale uncertainty of 8.6% due to the precision of the beam and target polarisation measurements. Also shown are model calculations from the GPD model [29].The bottom panel shows the fractional contribution from associated production to the yield in each kinematic bin estimated from a simulation.

for the charge-difference transverse double spin asymmetry, and for the charge averaged asymmetry

$$A_{LT,\mathrm{BH+DVCS}}^{\cos(\phi-\phi_s)\cos\phi} \propto Re[\mathcal{H}\mathcal{E}^* - \mathcal{E}\mathcal{H}^* - \xi(\tilde{\mathcal{H}}\tilde{\mathcal{E}}^* - \tilde{\mathcal{E}}\tilde{\mathcal{H}}^*)], \tag{2.69}$$

$$A_{LT,\mathrm{BH+DVCS}}^{\sin(\phi-\phi_s)\sin\phi} \propto Re[-\mathcal{H}\mathcal{E}^* - \mathcal{E}\mathcal{H}^* + \xi(\tilde{\mathcal{H}}\tilde{\mathcal{E}}^* - \tilde{\mathcal{E}}\tilde{\mathcal{H}}^*)]. \tag{2.70}$$

2.10 Extraction of CFF from Data

From the results above and results from Hall A and Hall B at Jefferson Lab, global fits to extract CFFs $\mathcal{H}$ and $\tilde{\mathcal{H}}$ [41–43] have been performed.

Figure 2.18 shows global fits of CFF $\mathcal{H}$ from Reference [43] compared to the VGG model (Section 2.5.1) and the model based fit discussed in Section 2.5.2 at HERMES and JLab kinematic conditions. These fits are model independent and are with DVCS observables at fixed kinematics, and use the values from the VGG model

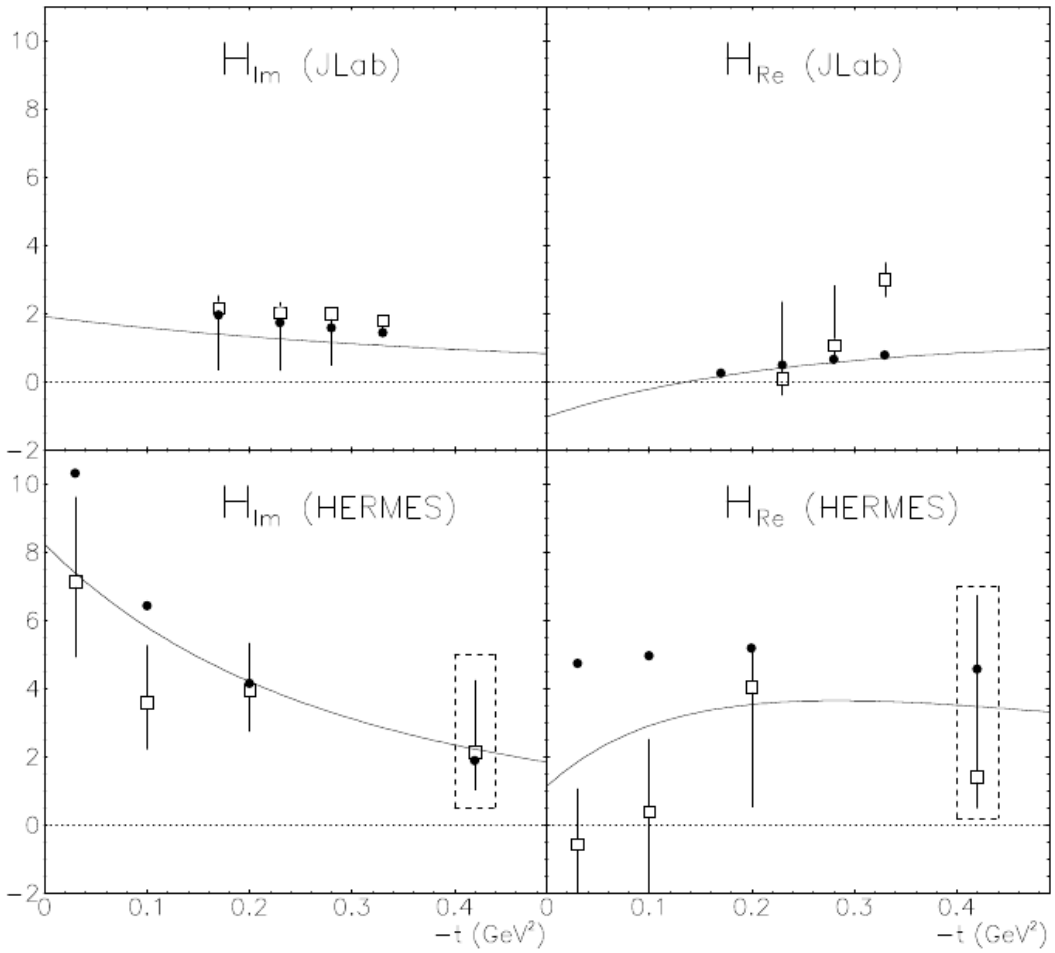

Figure 2.18: The t dependence of the real and imaginary parts of CFF $\mathcal{H}$ (H_{Im} and H_{Re}) from [43] (open squares). The upper panels show fits at JLab kinematics of DVCS unpolarised cross section and BSA. The lower panels show fits at HERMES kinematics. The largest t bin is in a box as this resulth as more constraints. The solid circles show results from the VGG parameterisation [29], discussed in Section 2.5.1. The solid curves show the model based fit discussed in Section 2.5.2 [32].

as the starting point for the fits. Although there are 7 unknown parameters from the 4 CFFs in the fit, only returned with finite error bars $\mathcal{H}_{Im}$, $\tilde{\mathcal{H}_{Im}}$, and $\mathcal{H}_{Re}$ returned with finite error bars.

Figure 2.19 shows the global fit of the real and imaginary part of CFF $\mathcal{H}$ at JLab kinematics in the left panel. These are compared to the fit by Guidal in the centre and Munoz-Camacho [44]. The green (blue) curve is the result from the model calculations from KM [32] with and without $\tilde{\mathcal{H}}$. The full black squares show the result of Reference [45]. The fit by Moutarde [41] is calculated at leading twist

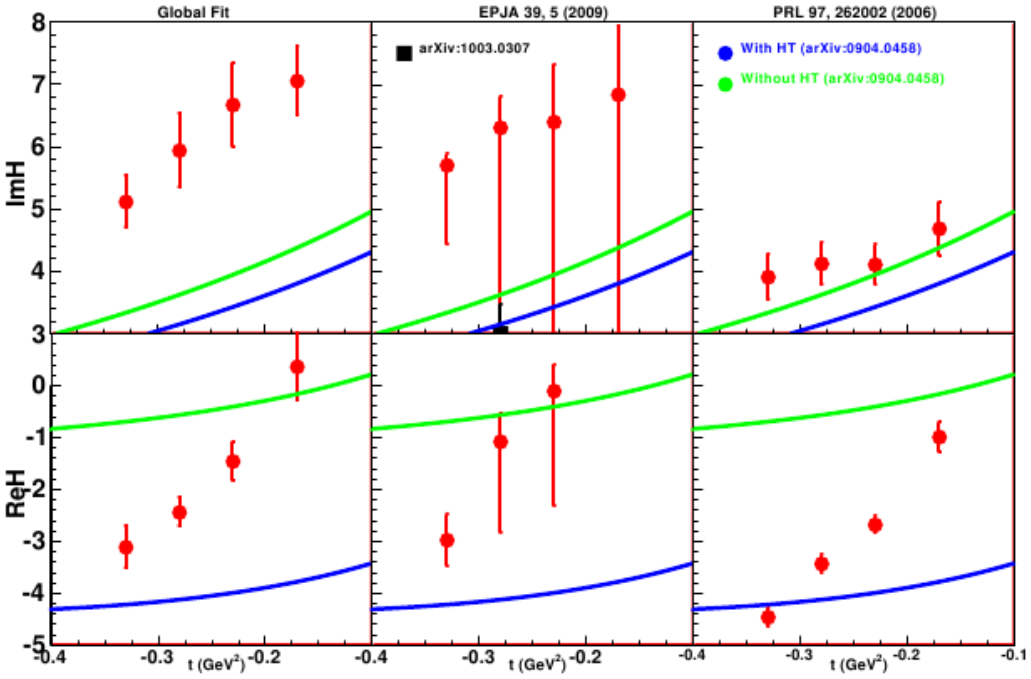

Figure 2.19: The global fit of the real and imaginary part of CFF $\mathcal{H}$ at JLab kinematics in the left panel. This is compared to the fit by Guidal in the centre [43] and Munoz-Camacho [44] . The green (blue) curve is the result from the model calculations from KM [32] with and without $\tilde{\mathcal{H}}$. The full black squares show the result of Reference [45]. [41]

and assumes dominance of GPD H. There is good agreement between this global fit and the other fits shown in the figure.

2.11 Summary

This chapter has reviewed the theoretical background of nucleon structure. A theoretical description of nucleon structure is Generalised Parton Distributions, which are of particular interest as they can provide access to the total angular momentum of quarks in the nucleon and provide a 3–dimensional picture of the nucleon structure. These can be accessed experimentally via exclusive processes, the simplest being DVCS. This chapter described in further detail how the DVCS experimental observables relate to GPDs. There are a number of models of GPDs, a few of which were described in this chapter. These models were selected as they have been used for comparison against experimental results from HERMES in this thesis.

After discussing the theoretical aspects, a review of the various DVCS asymmetry measurements made at HERMES and how they relate to different combinations of GPDs was made. These results have been used to constrain global fits of GPDs.

The aim of this work was to compare the previously published results that contained a contamination from from BH/DVCS events with a resonant proton (Δ) in the final state. The BHA amplitudes in this thesis are free from this background. By comparing this work with currently published measurements, the effect of the associated background on the extracted asymmetry amplitudes can be ascertained.

Chapter 3

The HERMES Experiment

The HERMES experiment was one of four experiments located on the HERA (Hadron–Electron Ring Accelerator) ring at the Deuches Elektronen-Synchrotron (DESY) facility in Hamburg, Germany. The initial aim of HERMES was to investigate the spin structure of the nucleon via Deep Inelastic Scattering (DIS). Experimental data was taken for the first time in 1995 and continued until the HERA shutdown in 2007. It was a fixed target experiment using a gaseous target and used only the lepton (electron/positron) beam at HERA. During its lifetime, HERMES had several upgrades in order to expand upon the original physics programme. The final upgrade presented in this thesis, was the construction and installation of the Recoil Detector [46, 47] in the target region.

There were three other experiments situated on the HERA ring. Two, H1 and ZEUS, were collider experiments using both beams, which collided in the detector halls. The third, HERA–B was a fixed target experiment like HERMES, but used the proton beam rather than the lepton beam. All experiments continued data taking until the end of HERA, with the exception of HERA–B which finished in 2003.

This chapter will describe the HERA storage ring, and the HERMES experimental set–up, focusing on the sub–detectors that were key to the DVCS analysis presented in this thesis.

3.1 The Lepton Beam at HERA

The HERA storage ring (Fig. 3.1) has a circumference of 6.3 km. The lepton beam was accelerated to 27.6 GeV. Primarily, positrons were used as the beam-lifetime was longer for positrons, however electrons were used for some short periods during the lifetime of the experiment.

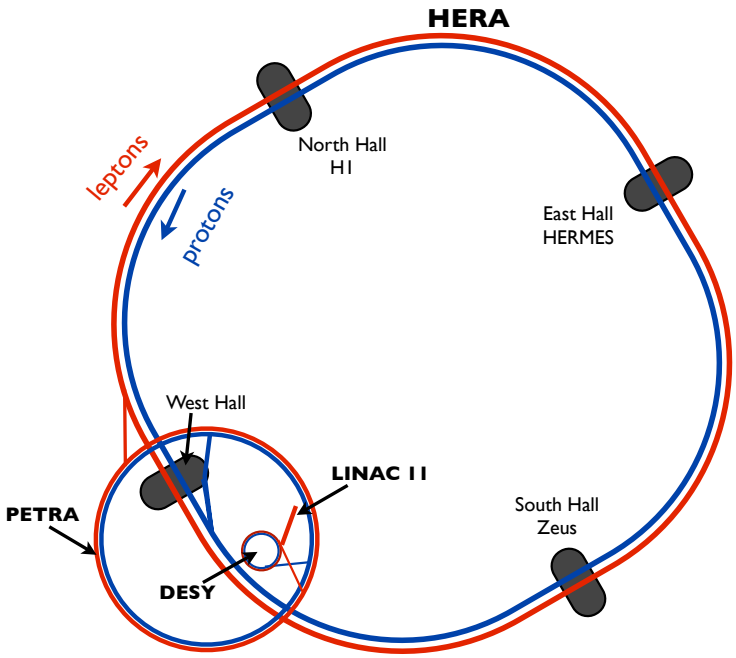

Figure 3.1: A schematic diagram of the HERA accelerator at DESY and the system of pre–accelerators for the lepton beam (shown in red)

.

3.1.1 Polarisation of the Beam

The lepton (electron/positron) beam was accelerated up to energies of 27.6 GeV using the different pre–accelerators shown in Figure 3.1. Initially, the beam was accelerated through the LINAC-II linear accelerator to 450 MeV, before further acceleration in the DESY-II storage ring to 7.5 GeV. Next, the leptons were transferred to the PETRA storage ring, and accelerated to 12 GeV. Finally the beam was injected

into HERA and accelerated up to the operational energy of 27.6 GeV.

At the point of injection into HERA, the beam was unpolarised. The beam polarisation in HERA occurred naturally via the Sokolov–Ternov (ST) effect [48], where a small asymmetry arose in the flip probability in the emission of synchrotron radiation. The effect accumulated over successive orbits providing a large transverse polarisation. The polarisation of the beam can be defined by

$$P = \frac{N^{\uparrow} - N^{\downarrow}}{N^{\uparrow} + N^{\downarrow}}, \tag{3.1}$$

or as an asymmetry in the spin orientation ($\uparrow$ or $\downarrow$) of the beam lepton yield N. This increases exponentially with time, τ, as

$$P = P_{ST}(1 - \mathrm{e}^{-\tau/\tau_{ST}}). \tag{3.2}$$

The maximum polarisation possible from the ST effect is $P_{ST} = \frac{8\sqrt{3}}{15}$, $\approx 92.4\%$ in an ideal machine. The characteristic polarisation rise-time is given by

$$\tau_{ST} = P_{ST}\frac{m_e\rho^3}{\hbar c^2 r_e \gamma^5}, \tag{3.3}$$

where m_e is the electron mass, ρ is the bending radius of the magnetic field, r_e is the classical electron radius and $\gamma = \frac{E_l}{m_e}$ is the Lorentz factor with beam energy E_l. When this is applied to the HERA storage ring, an optimum rise time of 37 minutes is deduced. However, several depolarising effects limited the maximum polarisation achieved at HERA, such as lepton-proton beam interaction and misalignment of the beam magnets, among other effects. The average beam polarisation of the data analysed in this thesis was 40 %. These effects were not controlled, therefore the beam polarisation was constantly monitored.

At HERMES, longitudinal beam polarisation was required, and this was achieved using 'spin rotators' installed upstream and downstream of HERMES [49]. These consisted of six horizontal and vertical dipole magnets, which rotated the spin vector of the leptons in increments up to 90°. The effect of these rotations had no effect on the overall polarisation, only the direction. The spin rotators located upstream of

HERMES returned the polarisation to its initial state to take advantage of the natural self–polarisation due to the ST effect and prevented degradation which would occur for longitudinal polarisation.

The beam polarisation at HERMES was measured simultaneously by transverse and longitudinal polarimeters. The transverse polarimeter (TPOL) was located in the West section of the HERA ring, and longitudinal polarimeter (LPOL) was located in the East section of HERA. Both of them utilised the spin dependent cross sections for Compton scattering of circularly polarised laser photons on polarised electrons. These are described in the following sections. Figure 3.2 shows a comparison of the beam polarisation measurements from the TPOL and LPOL.

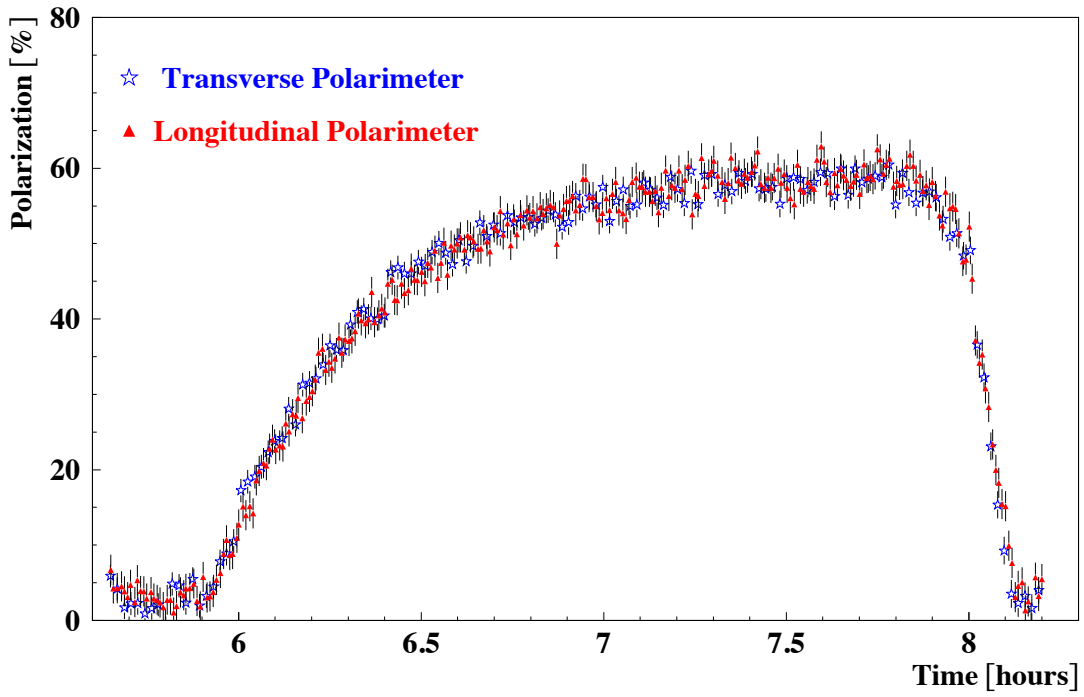

Figure 3.2: Comparison of the beam polarisation measurements from the TPOL and LPOL [**?**]. The beam polarisation typically reached a maximum within a 40 minute rise–time.

Transverse Polarimeter (TPOL)

The TPOL [50] used a method known as Compton-laser polarimetry which relied on the interaction of circularly-polarised laser light with the transverse polarisation direction of the beam. The asymmetries in the Compton back-scattering distribution

of polarised photons incident on the beam were measured from the detection of the back-scattered photons by calorimeters. The asymmetrical distribution of photons is given by

$$\Delta y(E_\gamma) = \Delta S_3 \Pi_y(E_\gamma) P_\gamma, \tag{3.4}$$

where E_γ is the energy of the photons, P_γ is the polarisation of the lepton beam in the y direction, Π_y is the analysing power of the polarimeter and ΔS_3 is the circular polarisation of the laser light. For the measurement of the beam polarisation to be within 1% statistically accuracy typically took less than a minute. The measurement had a systematic uncertainty of 3.4%.

The Longitudinal Polarimeter (LPOL)

The LPOL [51] also used circularly polarised laser photons, however the LPOL measured an energy asymmetry of the photons incident on the longitudinally polarised beam, given by

$$A(\Delta S_3, P_{lz}) = \Delta S_3 \Pi_z P_{lz}. \tag{3.5}$$

This depends on the analysing power of the LPOL, Π_z and the beam polarisation P_{lz}. The systematic uncertainty of the LPOL was 1.6%.

3.2 The Hermes Target

The Hermes experimental set up used a gas target internal to the storage ring. A gas target was chosen to minimise any effects on other experiments located on the storage ring by degrading the lifetime of the beam. The density of the gas was increased at the end of a fill, thus increasing the reaction rate. During 2006 and 2007 this method was used to increase the luminosity during the final two years of Hera operation.

The storage cell was filled with a number of target gases over the running period of Hermes including hydrogen, deuterium as well as heavier gases. The analysis presented in this thesis used only data taken on a hydrogen target. Therefore, for the remainder of this thesis a hydrogen gas target will be assumed unless otherwise stated.

3.2.1 The Unpolarised Gas Feed System

At Hermes, there were two systems used for the injection of gas into the target cell, the Atomic Beam Source (ABS) [52] and the Unpolarised Gas Feed System (UGFS) [53]. These were used to provide a polarised and unpolarised hydrogen target respectively. For this thesis only data taken with an unpolarised target was used.

The UGFS allowed the selection of target gas type and density as required. For the final two years of Hera operation, hydrogen and deuterium were used.

The Target Cell

Many target cells were used throughout the lifetime of the Hermes experiment, designed to accommodate the varied physics programme and to provide the highest number of interactions possible between the lepton beam and the gas target.

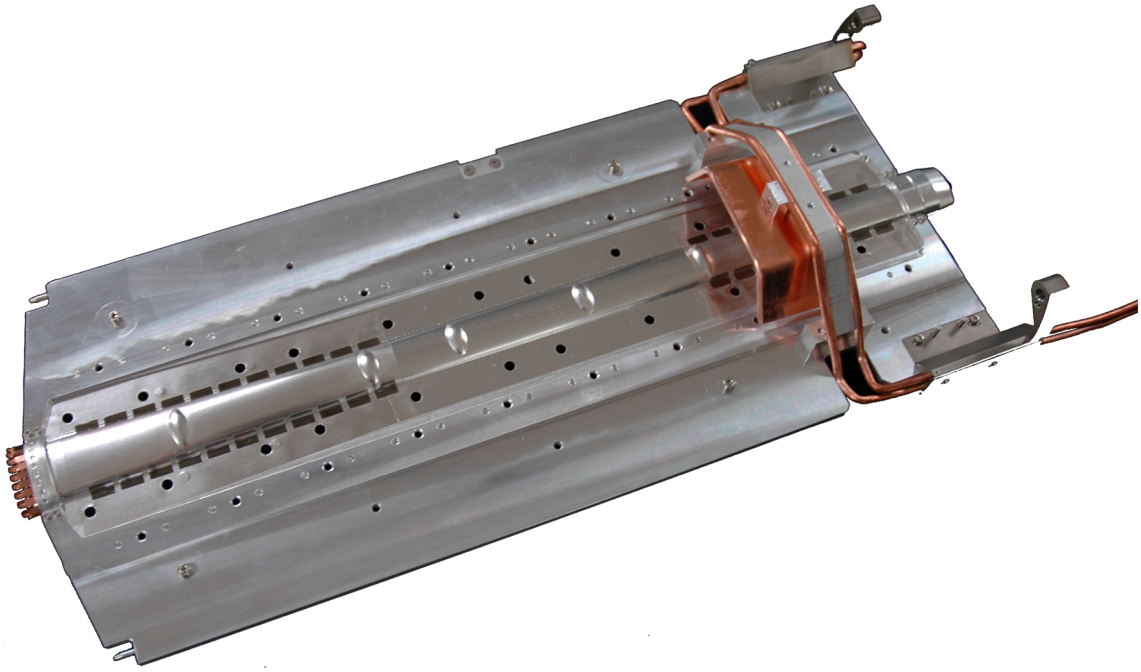

Figure 3.3: A photograph of the target cell used in 2006 and 2007. Image from [54].

During the running period relevant to this thesis, the target cell used was an open ended elliptical aluminium tube shown in Figure 3.3 with a horizontal (vertical) diameter of 21 (9) mm, 150 mm long [46], and cell walls 75 μm thick. At the centre of the target cell was the gas inlet where gas was injected into the target cell. The

gas atoms diffused out of the cell, and were pumped away at the outer edges by a pumping system. The target was water cooled to maintain the optimum operational temperature and maintain the target density.

3.2.2 The HERMES Coordinate System

Throughout this thesis, kinematic variables are defined in the HERMES coordinate system. It is a right handed coordinate system as defined in Fig. 3.4 with the positive z direction originating from the target cell along the beam line to the forward spectrometer that is described in Section 3.3.

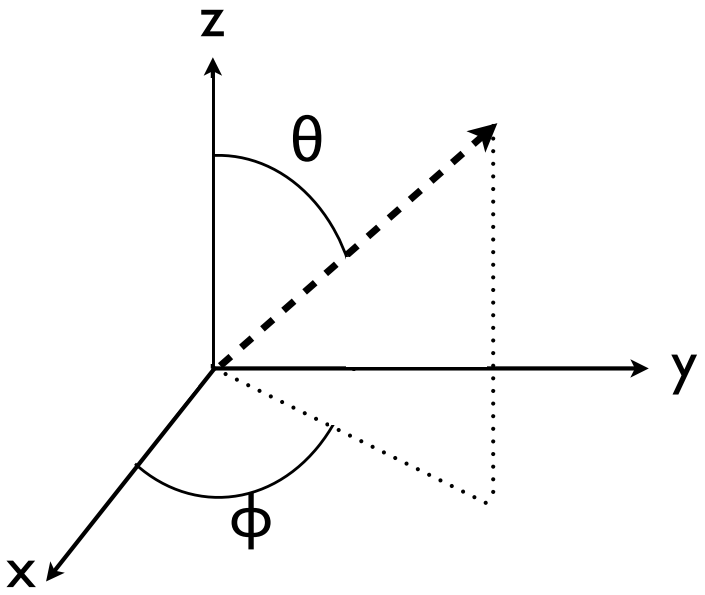

Figure 3.4: The HERMES coordinate system. The z direction is along the beam line, and the ϕ angle is defined by the x-y plane, with the θ angle defined with respect to the y-z plane.

3.3 The HERMES Spectrometer

The HERMES forward spectrometer [55], as shown in Figure 3.5, consisted of two halves above and below the beam line. A dipole magnet provided a magnetic field of

1.3 T. The beams were shielded from this field by a steel plate. Due to the presence of this plate, the angular acceptance was limited to $|\theta_{horizontal}| < 170\,\text{mrad}$ and $40\,\text{mrad} < |\theta_{\text{vertical}}| < 140\,\text{mrad}$.

The sub–detectors can be organised into three categories, those used for particle track reconstruction, those for momentum reconstruction, and those for particle identification. This section will describe those detectors used in the DVCS analysis presented in this thesis.

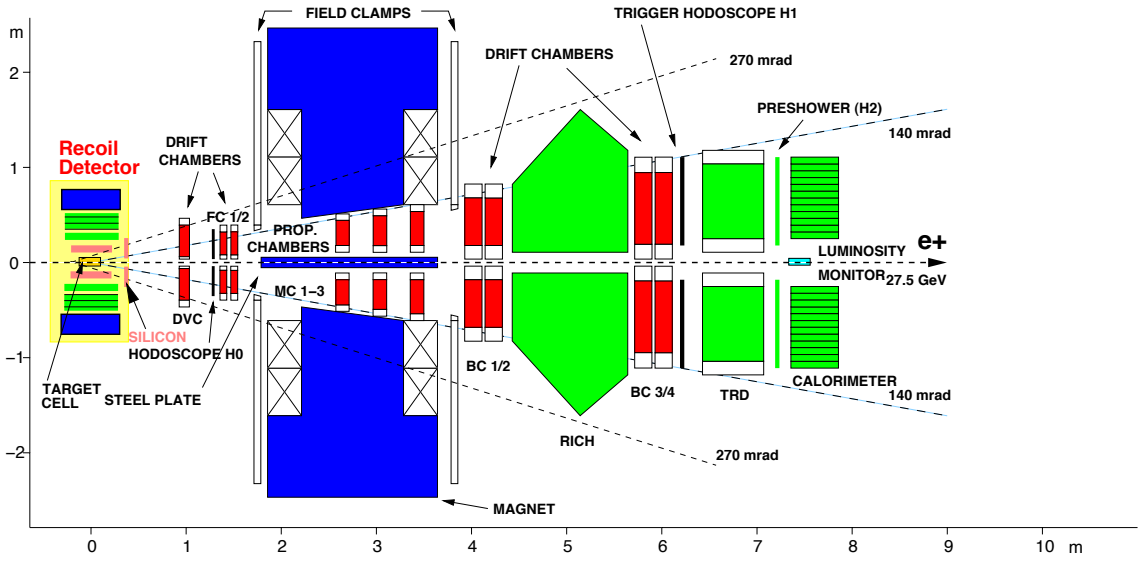

Figure 3.5: The HERMES experimental setup used in 2006–2007. The components shown in green were used for particle identification, red components were part of the tracking system, and the magnets are shown in blue.

3.3.1 Tracking Detectors

Once particles had left the target region they passed through the Drift Vertex Chambers (DVC) and Front Chambers (FCs), located in the front region before the magnet. The rear area (after the magnet) contained the Back Chambers (BCs). Within the magnet region there was a series of 3 Magnet Chambers (MCs).

3.3.1.1 Drift Vertex Chambers

The chambers consisted of wires fixed in a gas–filled volume, each layer with alternating anode wires (at ground) and cathode wires (at a negative high voltage). They operated with a gas mixture of Ar(90%), CO_2(5%) and CF_4(5%). As charged

particles traversed the chambers, the gas was ionised thus producing electrons accelerated by the internal electric field. This induced further ionisation and created an avalanche.

3.3.1.2 Magnet Chambers

The Magnet Chambers (MCs) were Multi–Wire Proportional Chambers (MWPCs), with a similar design to the DVCs. The gas mixture used for MWPCs was Ar(65%), CO_2(30%) and CF_4(5%). The gas mixture was optimised for the drift velocity of electrons and was non–flammable. The MCs provided a spatial resolution of 700 μm.

3.3.2 Particle Identification Detectors

The particle identification (PID) systems in the forward HERMES spectrometer were optimised to discriminate between leptons and hadrons. There were four subdetectors in the spectrometer used for this purpose: the Transition Radiation Detector (TRD), the electromagnetic calorimeter, a preshower detector, and the Ring Image Cerenkov Detector (RICH). For the analysis in this thesis, the RICH wasn't used, and will not be described in the following section. For further details about the RICH, consult Ref [56].

3.3.2.1 Transition Radiation Detector

The TRD [57] was made up of 6 modules above and below the beam line. Each module consisted of a radiator and a proportional wire chamber. The chambers consisted of 256 vertical wires, separated by 1.27cm and filled with a Xe(90%) and CH_4(10%) gas mixture. This mixture was used due to its high X-ray absorption efficiency.

The purpose of the Transition Radiation Detector (TRD) was to discriminate between hadrons and leptons. The positrons in the HERMES energy regime produced transition radiation as photons with X-ray energies. Hadrons also deposited some energy due to ionisation in the TRD, however the signal was much lower in energy and was easily separable from the positron signal.

3.3.2.2 The Electromagnetic Calorimeter

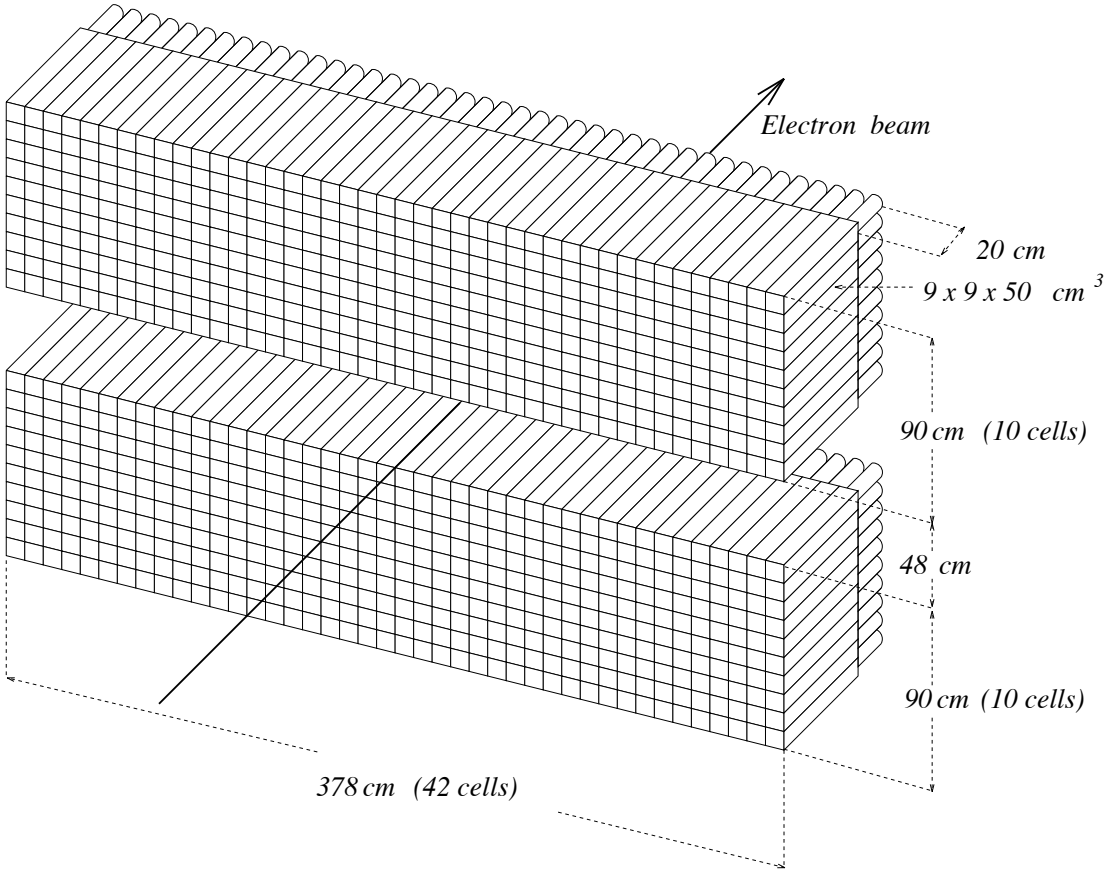

Figure 3.6: Schematic diagram of the electromagnetic calorimeter [58]

The electromagnetic calorimeter [59], shown in Fig 3.6, as well as providing energy measurements for photons and neutral particles, was also used to differentiate between hadrons and electrons. This was achieved by comparing the ratio of their energy deposition and momenta (E/p), where the momentum was determined from the track reconstruction. The calorimeter was designed such that it was thick enough to contain an electromagnetic shower from a charged lepton within a block. For a charged lepton almost all the lepton energy was deposited, i.e. $E/p \approx 1$, as seen in Figure 3.7.

For hadrons, the mean free path between intersections is larger than for leptons and hence hadrons would not be contained within the calorimeter. Therefore, their ratio E/p was typically smaller than 1.

The calorimeter comprised of 840 lead glass blocks, 9 cm $\times$ 9 cm and 50 cm long,

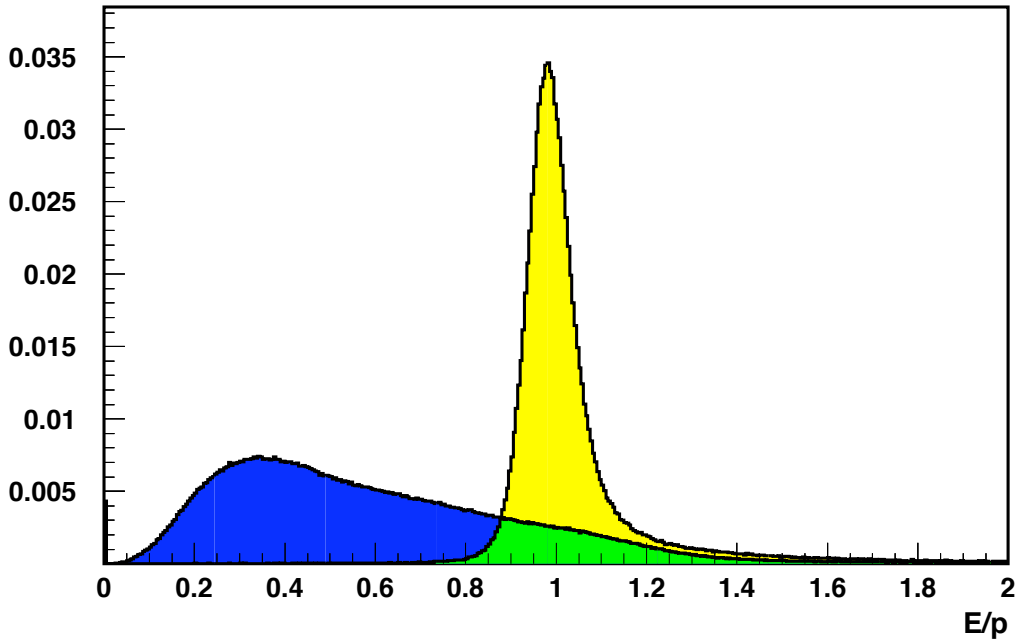

Figure 3.7: Energy distribution in the calorimeter. The dark region shows the hadrons, and light region shows the leptons. [57]

arranged in two 42×10 arrays either side of the beam line (Figure 3.6). The calorimeter was also used in the DVCS analysis to provide information for the produced real photon. However the energy resolution of the calorimeter is poor for photons.

The calorimeter was complimented by a preshower hodoscope (H2), which was a 1.14 cm thick lead plate from which the electromagnetic showers originated.

Uncharged particles, such as photons, were detected only in the calorimeter. With no corresponding track, all the information for electrically neutral particles came from just the one source. This meant that the energy resolution was poorer than for tracked particles. Thus for a DVCS analysis, the introduction of a constraint on the calculation of Mandelstam t is used throughout the analysis. This is introduced in Section 4.1

3.3.2.3 The Preshower detector

The preshower, or H2 hodoscope, consisted of 42 vertical scintillators of width 9.3 cm to equal the size of the calorimeter. The preshower also had a passive radiator of two radiation lengths of lead in front to act as a preshower counter to provide a com-

plimentary discrimination between hadrons and leptons. Only leptons produced an electromagnetic shower when passing through the lead layer, thus hadrons can be distinguished from leptons by the different amount of Electromagnetic radiation they produce when passing through the H2 hodoscope. In the region where the distributions overlapped, the calorimeter was used to distinguish hadrons from leptons.

3.4 Recoil Detector

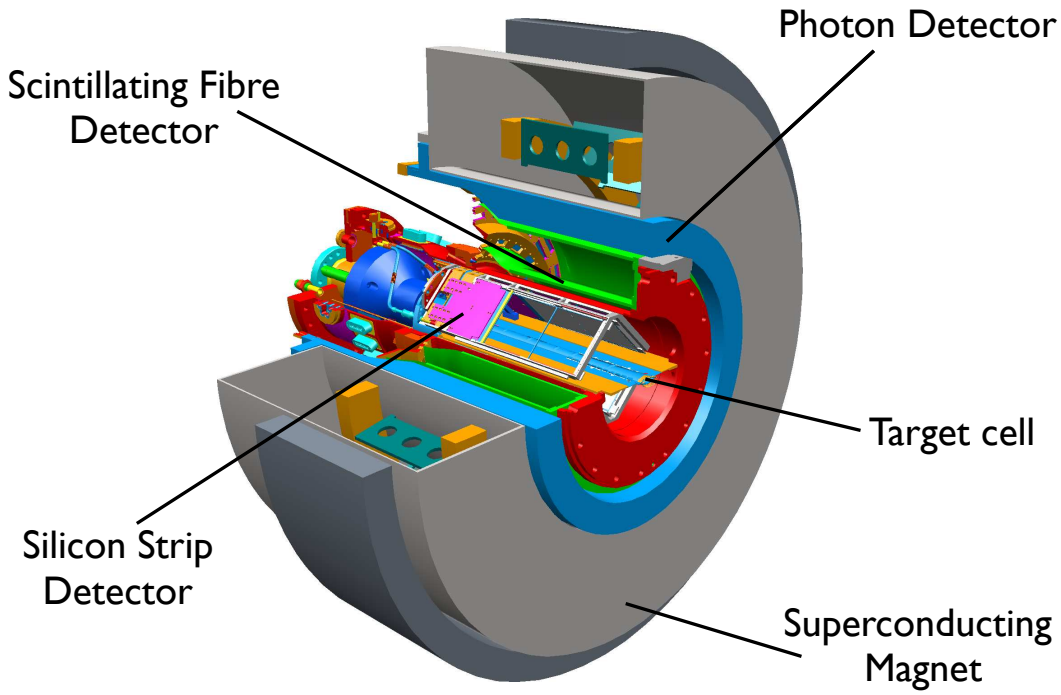

Figure 3.8: Schematic diagram of the Recoil Detector showing each component. Figure modified from [46]

The purpose of the Recoil Detector (RD) [46, 47] was to detect the recoiling proton for exclusive physics scattering processes, and thus prove the exclusivity of the DVCS measurements at HERMES. The RD was located around the target region, and consisted of three sub-detectors: the Silicon Strip Detector (SSD), the Scintillating Fibre Tracker (SFT) and the Photon Detector (PD), operating within

a 1.0 T magnetic field from a superconducting Helmholtz coil. This can be seen in Fig. 3.8.

3.4.1 Silicon Strip Detector

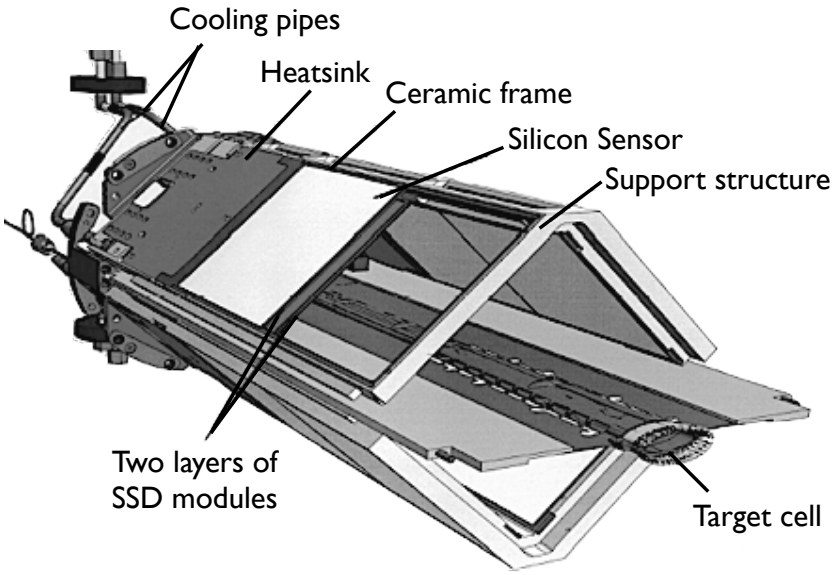

Figure 3.9: Schematic diagram of the silicon strip detector (SSD), modified from [60].

In order to detect low momentum recoiling particles (0.135 GeV/c - 0.4 GeV/c) the SSD was located inside the scattering chamber in the beam vacuum. The detector consisted of 16 double sided silicon strip-sensors, with 128 strips per side, and each strip 758 μm wide. Each sensor was 99 $\times$ 99 mm^2 and 300 μm thick. The sensors were placed in a diamond configuration around the target cell, each side consisting of 4 sensors, two sensors side by side in two layers.

The cross section of the RD was in quadrants, which will be referred to in this thesis. Quadrant 1 is the region with azimuthal angle in the range $[3\pi/2, 2\pi]$, quadrant 2 is the region between 0-$\pi/2$ rad, and quadrants 3 and 4 following in increasing azimuthal angle. The quadrants are shown in Figure **??**.

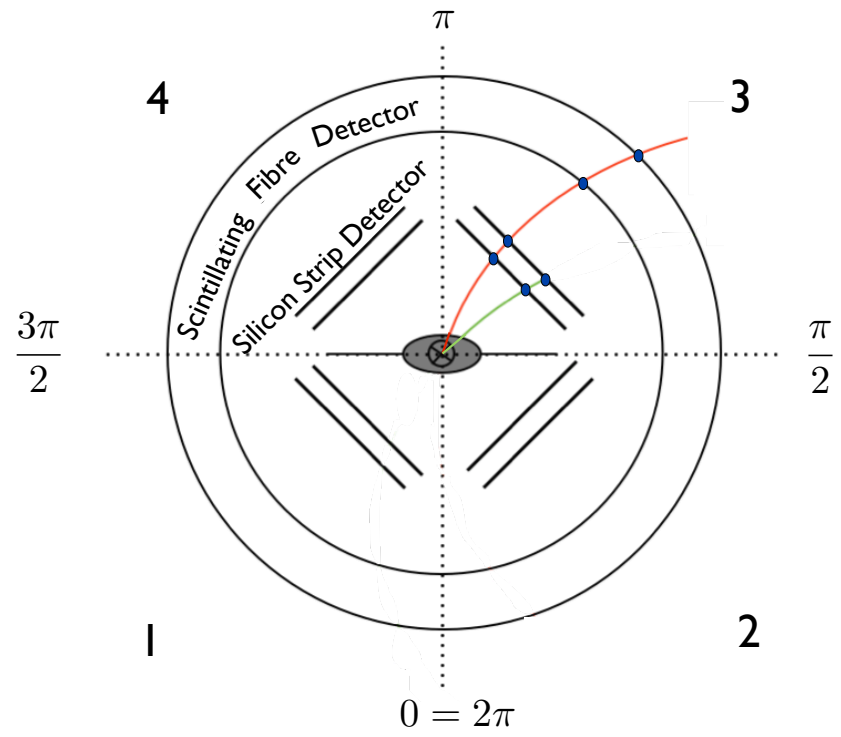

Figure 3.10: Schematic diagram showing the recoil detector quadrants and tracking scheme. A 4–spacepoint track is shown in red, and a 2–spacepoint track shown in green.

3.4.2 Scintillating Fibre Tracker

The Scintillating Fibre Tracker (SFT) was designed to measure protons and pions with momenta of 0.25 to 1.40 GeV/c, and to provide particle identification for particles below 0.65 GeV/c.

It was located outside the beam vacuum around the SSD, and consisted of 2 barrels of scintillating fibres, with a thickness of 4 mm and an inner radius of 108 mm and 183 mm respectively. Each barrel contained 4 layers of scintillating fibres, 2 parallel to the beam, and 2 layers at a stereo angle of 10°. The 4992 fibres were 1 mm in diameter. The fully constructed SFT is shown in Fig. 3.11.

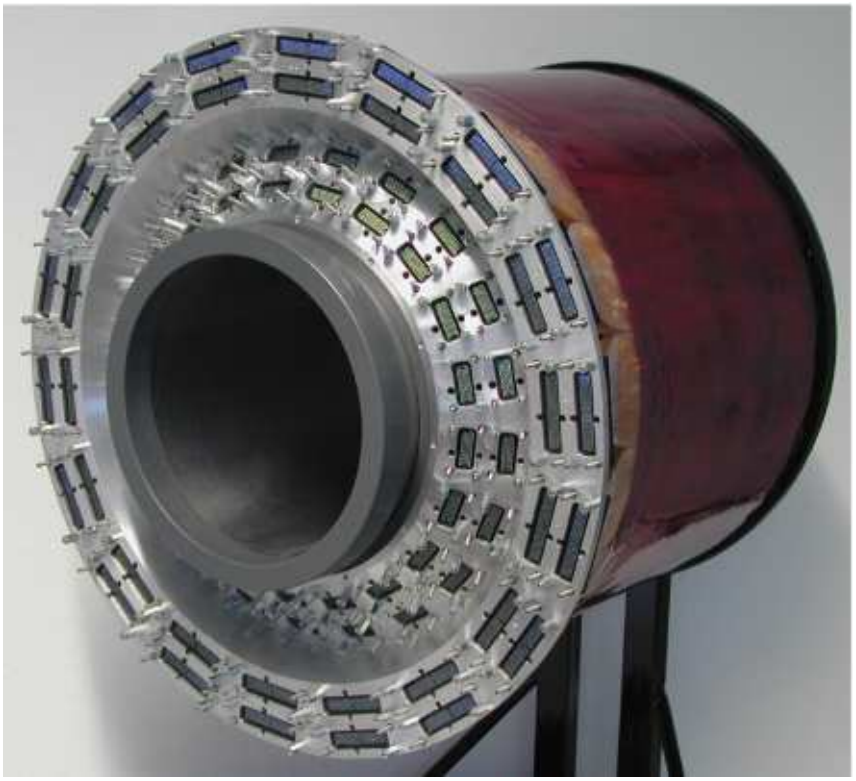

Figure 3.11: Photograph of the assembled SFT before its installation [61].

3.4.3 Photon Detector

The Photon Detector (PD) [62] was designed to detect photons and help with the reconstruction of neutral pions from the decay of the Δresonance to help reduce background. It consisted of 3 layers of 2 cm wide scintillating strips. The inner layer strips were parallel to the beam pipe, while the two outer layer strips were at an angle of $\pm 45\,^{\circ}$ with respect to the beam pipe. The strips were sandwiched with layers of tungsten. The scintillated light was then detected by multi–anode Photo Multiplier Tubes (PMTs).

3.4.4 Superconducting Magnet

The Recoil Detector was surrounded by a superconducting magnet which was necessary to determine the momentum from the track reconstruction in the SSD and SFT detectors. The magnet provided a 1 Tesla field, and consisted of two Helmholtz coils immersed in liquid Helium. To provide sufficient overlap in the momentum resolutions of the two detectors, the magnetic field homogeneity had to exceed 20 %,

Figure 3.12: Photograph of the photon detector before it's installation [61].

and have sufficient field strength (1 Tesla). For accurate momentum reconstruction the magnetic field had to be well understood [63].

The magnet also provided shielding for the SSD from background scattering events. In the case of a positron beam, the background was from Bhahba scattering, where positrons within the beam scattered on electrons of the target atoms. The magnet was able to remove these high energy electrons from the acceptance of the SSD.

3.5 Data Taking and Processing

3.5.1 Data Taking

To activate the readout from the detectors a trigger was needed to identify events of interest. There were many trigger schemes defined at HERMES, though for the purposes of this thesis only trigger–21 (the DIS trigger) is considered. This trigger

signified the presence of a high energy scattered lepton, which required simultaneous signals in the three hodoscopes, and a total energy deposit $> 3.5\,\text{GeV}$ to ensure good separation between hadrons and leptons. Once the trigger had been activated, the data acquisition (DAQ) system read out the detector signals. In approximately 10 second intervals (bursts) additional control data, such as the luminosity and beam polarisation, were read out. The events from the 10 second time frame were grouped together; and these bursts were then grouped together into a run, which was defined by a size of 450 MB of Experimental Physics Input Output (EPIO) data. The data were then processed offline.

The data structure at HERMES is depicted in Figure 3.13. Each year of data–taking has a number of data productions, the most recent productions containing the most recent improvements in detector calibrations, particle tracking and data quality. Each data production consisted of data runs, which lasted approximately 30 minutes. Each run was made up of 10 second bursts of data, where the beam target and detectors were continuously monitored. THe data burst contained the physics events recorded.

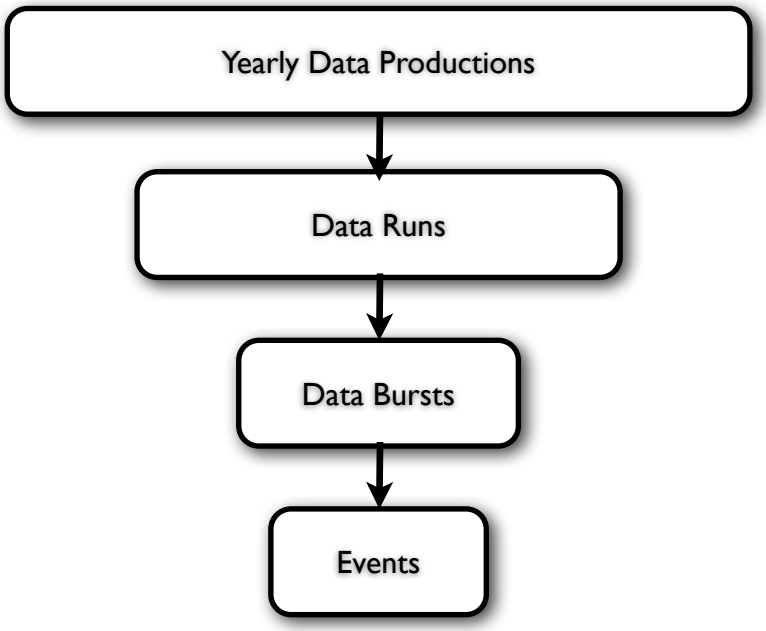

Figure 3.13: Schematic diagram of the structure of data storage.

3.5.2 Decoding

The first step in the offline data processing was by the HERMES decoder (HDC) which translated the signals from the Analogue to Digital Converter (ADC) and Time to Digital Converter (TDC) modules into physical quantities in the HERMES coordinate system. These were then stored in DAD (Distributed ADAMO (Aleph Data Model)) tables [64].

3.5.3 Track Reconstruction Software

3.5.3.1 Forward Spectrometer Tracking

The HERMES reconstruction code (HRC) [65] reconstructed charged particle tracks in the spectrometer. It examined the hits in the drift chambers, and used a tree-search algorithm to find tracks. Tracks in the front (FCs and DVCs) and back (BCs) regions were reconstructed separately and then combined with the MCs to determine the particle track. In 2009, the HERMES Tracking Code (HTC) was added to HRC to improve the tracking. It takes as input the tracks found by HRC and reparameterises them via an advanced track fitting procedure. The HTC provided reparametrisation at a few different z positions along the beam line. These track parameters were then saved into μDST tables. The steps in the decoding and tracking reconstruction are shown in Figure 3.14.

3.5.3.2 Recoil Detector Tracking

The eXternal Tracking Code (XTC) reconstructed tracks in the RD using space point information from the SSD and SFT. The first stage of the track fitting procedure is the track search, initially for tracks with a spacepoint in each sub-detector (4–spacepoint track). Each track is then fitted, and if the χ^2 uncertainty is below a predetermined cut the track is accepted. The next step looks for all possible combinations of 3–spacepoint tracks (with spacepoints which do not belong to the 4–spacepoint tracks), these are then fitted and accepted in a similar fashion. Finally 2–spacepoint tracks in the SSD were considered (without spacepoints included in the 3- or 4–spacepoint tracks). Figure **??** shows what is meant by a 2- or 4–spacepoint

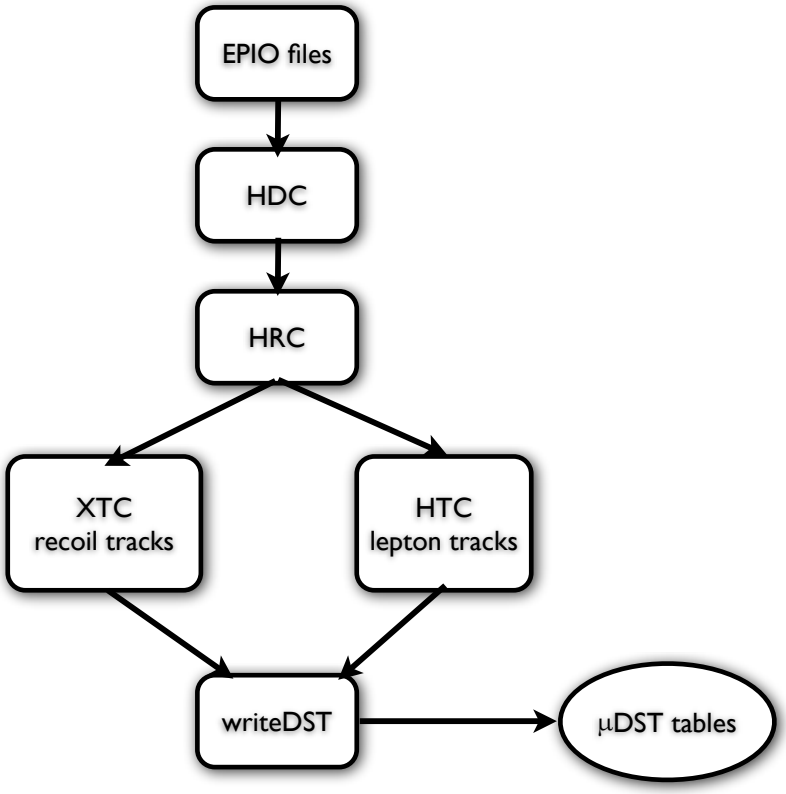

Figure 3.14: Schematic diagram to illustrate data processing.

track.

Every track was fitted using different particle type hypotheses:

- **Pion Hypothesis**: Reconstruction of particle momentum from bending in the magnetic field and taking into account the energy losses from detector components and passive materials, assuming a pion mass.
- **Proton Hypothesis**: The same as the pion hypothesis, but assuming a proton mass.
- **Stopped Proton Hypothesis**: Reconstruction of particle momentum from the energy deposited in the SSD.

There are several different track reconstruction methods [66], for this analysis the tracking method used is referred to as 'Method–7'. Only tracks reconstructed using this method are considered in this thesis. Further details on the track fitting procedures can be found in references [39], [63], [67]. Each fit provided a set of parameters

to be used by the analyser. The hypothesis selection used in the analysis of this thesis will be discussed in the next section. The μDST tables include information from each hypothesis available for each track, and linked via event and run number to the forward spectrometer tracks.

3.5.4 Particle Identification

Particle type was used to discern between hadrons and leptons in the forward spectrometer, and between protons and pions in the Recoil Detector, as detailed below.

3.5.4.1 Forward Spectrometer

The Particle Identification (PID) for the forward spectrometer discriminated between hadrons and leptons with a 99% efficiency using combined responses from all the detectors described in Section 3.3.2, to achieve this. The PID scheme is a Bayesian algorithm , where the probability that the track is a lepton (hadron) is evaluated given an observed detector response [58]. The PID value is then evaluated for each detector by comparing the probability of the track being a lepton or a hadron. Various PID combinations are stored in the μDST tables to be used by the analysers. For a DVCS analysis, particle identification information from the preshower and calorimeter (PID2 in the HERMES and the TRD (PID5) is used.

3.5.4.2 Recoil Detector

The Recoil Detector (RD) had an analogous PID (rdPID) to the spectrometer which was to separate low-momentum charged pions and protons. It was based on a similar Bayesian algorithm [68].

Information on the particle type could be deduced from 6–spacepoint layers in the RD, 2 in the SSD and 4 in the SFT. Particles with 3 or 4–spacepoints were only considered for the calculation of the rdPID. For each layer, the rdPID was calculated from parent distributions for real data using Method–7 tracking and the pion hypothesis. The parent distributions were calculated separately for each quadrant and were binned in momentum. The rdPID values for each layer were stored in the data tables and summed, i.e. rdPID $=\sum$ rdPID$_i$. The summed rdPID

versus momentum is shown in Figure 3.15, where the separation between protons and pions can be clearly seen.

For 2–spacepoint tracks, there is no rdPID available in the data tables and positive tracks are assumed to be protons. Studies on the use of the rdPID in the analysis of this thesis will be detailed in Section 4.7.

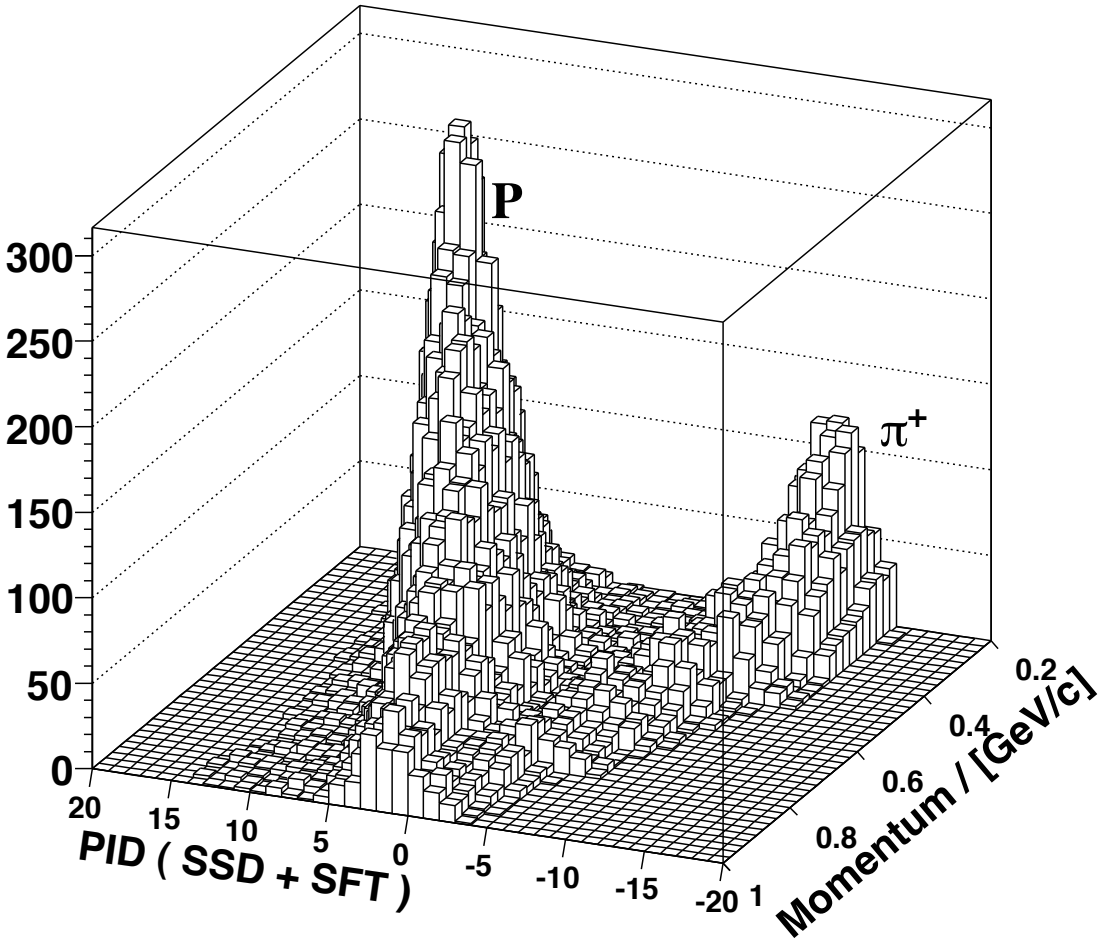

Figure 3.15: A plot of the Recoil Detector PID vs momentum of all tracks to demonstrate the separation between protons and pions at mom $<$ 650MeV [69].

Chapter 4

Data Analysis

This chapter presents the details of the analysis of data taken with the Recoil Detector from positron scattering off an unpolarised hydrogen target. The Recoil Detector was installed in 2006, and was fully operational from November of that year up until the end of July 2007. This is the first full analysis of this data set using information gained from Recoil Detector.

4.1 Kinematic Variables

In Chapter 2 most of the kinematic variables required have already been introduced. For the purposes of this thesis the analysed process involves the scattering of a positron off an unpolarised hydrogen target with a real photon produced in a final state that was detected as a trackless cluster in the calorimeter. The scattered positron was tracked through the HERMES spectrometer and identified as a single charged track. The recoiling proton was detected in the Recoil Detector. The process is illustrated in Figure 4.1, and is described by

$$e(\mathbf{k})\, p(\mathbf{p}) \overset{\gamma^*(\mathbf{q})}{\rightarrow} e(\mathbf{k}')\, p(\mathbf{p}')\, \gamma(\mathbf{q}'). \tag{4.1}$$

The four–momentum is defined using the standard notation $\mathbf{p} = (E, \vec{p})$, with the corresponding three-vector $\vec{p} = (p_x, p_y, p_x)$. With a fixed target, where the proton is at rest the four momenta can be expressed as

- The beam positron is assumed to be moving purely in the z direction. It's four–momentum is expressed as $\mathbf{k} = (E, 0, 0, P_{\text{beam}})$, where E (P_{beam}) is the incoming lepton energy (momentum).

- The four–momentum of the target proton at rest is $\mathbf{P} = (M_p, 0, 0, 0)$.

- The four–momentum of the virtual photon is calculated from the measured $\mathbf{k}'$ and $\mathbf{q}'$. It is expressed as $\mathbf{q} = (\nu, -|P_{\text{track}}| \sin\theta_l \cos\phi_l, -|P_{\text{track}}| \sin\theta_l \sin\phi_l, (P - |P_{\text{track}}| \cos\theta_l))$ where P_{track} is momentum of the detected positron track, θ_l is the polar angle between the incoming and scattered positrons, and ϕ_l is the azimuthal angle of the positron.

- The four–momentum of the scattered positron detected in the calorimeter. It is expressed as $\mathbf{k}' = \left(E', |P_{\text{track}}| \sin\theta_l \cos\phi_l, |P_{\text{track}}| \cos\theta_l\right)$, where E' is the energy of the scattered lepton.

- The four–momentum of the recoiling proton detected in the recoil detector is $\mathbf{P}'$.

- The four–momentum of the real photon, detected in the calorimeter, is expressed as

$$\mathbf{q}' = \left(E_\gamma, \frac{E_\gamma \vec{q'}}{|\vec{q'}|}\right).$$

The azimuthal angle between the lepton scattering plane and the photon production planes is calculated from the three–vectors of incoming positron and the real and virtual photons. This is expressed as

$$\phi = \frac{\vec{q} \times \vec{k} \cdot \vec{q'}}{|\vec{q} \times \vec{k} \cdot \vec{q'}|} \cdot \cos^{-1}\left(\frac{\vec{q} \times \vec{k}}{|\vec{q} \times \vec{k}|} \cdot \frac{\vec{q} \times \vec{q'}}{|\vec{q} \times \vec{q'}|}\right). \tag{4.2}$$

The kinematic variables introduced in Chapter 2 are also expressed in the lab frame. The negative squared four–momentum Q^2 of the virtual photon is calculated from the four–momenta of the incident and scattered leptons,

$$Q^2 \equiv -\mathbf{q^2} \equiv -(\mathbf{k} - \mathbf{k}')^2 \overset{\text{lab}}{=} 4EE' \sin^2\left(\frac{\theta_l}{2}\right). \tag{4.3}$$

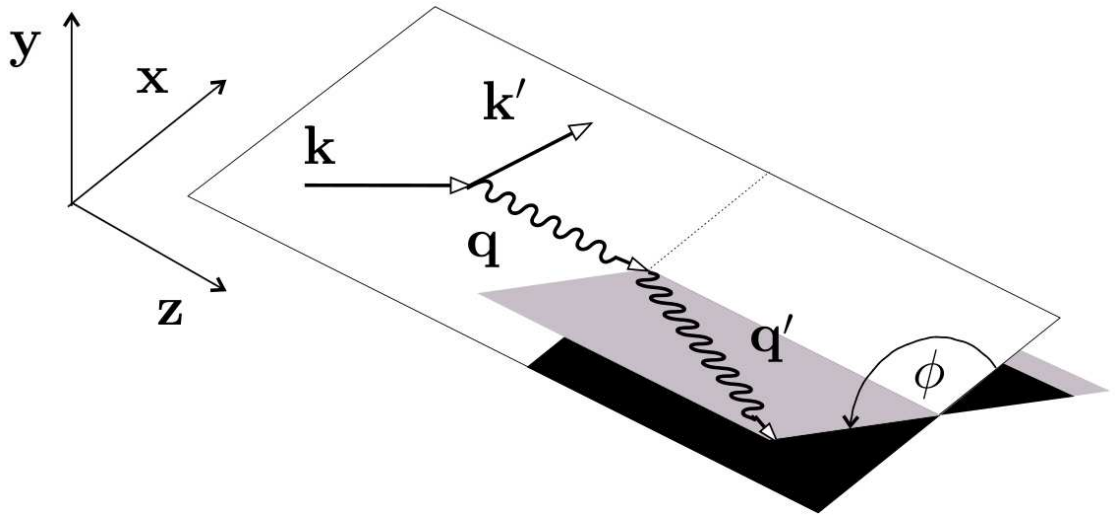

Figure 4.1: The definition of the angle ϕ between the lepton scattering and photoproduction plane [70].

The energy of the virtual photon ν is defined as

$$\nu = \frac{\mathbf{p}.\mathbf{q}}{M_p} \overset{\text{lab}}{=} E - E'. \tag{4.4}$$

The Bjorken scaling variable, x_B can be calculated as

$$x_B \equiv \frac{Q^2}{2(\mathbf{p}\cdot\mathbf{q})} \overset{\text{lab}}{=} \frac{Q^2}{2M_p\nu}. \tag{4.5}$$

The Mandelstan variable,t , is determined from the difference in four–momentum of the initial and final state nucleons or photons as

$$t \equiv (\mathbf{p}-\mathbf{p}')^2 \equiv (\mathbf{q}-\mathbf{q}')^2. \tag{4.6}$$

From the real and virtual photons it is calculated as

$$t \overset{\text{lab}}{=} -Q^2 - 2E_\gamma - \left(\nu - \sqrt{\nu^2+Q^2}\cos\theta_{\gamma^\star\gamma}\right), \tag{4.7}$$

where E_γ is the energy of the real photon deposited in the calorimeter that is subject to a large uncertainty and $\theta_{\gamma^\star\gamma}$ is the polar angle between the three–vectors of the

real and virtual photons, calculated as

$$\theta_{\gamma^\star\gamma} = \cos^{-1}\left(\frac{\vec{q}\cdot\vec{q'}}{|\vec{q}||\vec{q'}|}\right). \tag{4.8}$$

There is a large uncertainty in $\theta_{\gamma^\star\gamma}$ due to the comparatively poor resolution ($\approx$ 5%) of the photon energy measurement E_γ. Consequently the measurement in t is affected. As the final state proton is detected t can also be detected using the Recoil Detector as

$$t_{\mathrm{rd}} = 2M_p(M_p - \sqrt{P'^2 + M_p^2}). \tag{4.9}$$

Prior to the installation of the Recoil Detector, the selection of exclusive events relied on a missing mass technique. In order to compare to the previous analysis technique the squared 'missing-mass' M_x^2 of the $ep \to e\gamma X$ interaction was calculated for this analysis although it was not used for event selection. It is expressed as,

$$M_X^2 \equiv \left(\mathbf{k} - \mathbf{k'} + \mathbf{p} - \mathbf{q'}\right)^2 \overset{\mathrm{lab}}{=} M_p^2 + 2M_p^2(\nu - E_\gamma) + t. \tag{4.10}$$

Because there was a large uncertainty from measuring t from the real photon it was found that using a "constrained" calculation provided greater resolution. Assuming $M_X = M_p$ for elastic DVCS events, where the proton is left intact, equation 4.1 can be rearranged as

$$E_\gamma = \frac{t}{2M_p} + \nu. \tag{4.11}$$

This is then substituted to provide a constrained calculation of t for exclusive events. This quantity t_c no longer relies on the energy measurement of the real photon, but on its interaction position in the calorimeter, which can be measured with greater precision.

$$t_c \overset{\mathrm{lab}}{=} \frac{-Q^2 - 2\nu\left(\nu - \sqrt{\nu^2 + Q^2}\cos\theta_{\gamma^\star\gamma}\right)}{1 + \frac{1}{M_p}\left(\nu - \sqrt{\nu^2 + Q^2}\cos\theta_{\gamma^\star\gamma}\right)}. \tag{4.12}$$

It is shown that calculating t_c is comparable to using t_{rd}, therefore to be consistent with previous analyses t_c was used. For the remainder of this thesis t will be calculated as above, i.e $t = t_c$, unless otherwise stated.

Finally the definition of the invariant mass W of the $\gamma^* p$ system is needed because it is used as one of the key selection criteria for DIS events. The squared invariant mass is measured as

$$W^2 \equiv (\mathbf{p} + \mathbf{q})^2 \stackrel{\text{lab}}{=} M_p^2 + 2M_p\nu - Q^2. \tag{4.13}$$

4.2 Data Selection

The selection of a data sample from which to extract a beam helicity asymmetry is done in several stages. Initially the data quality is checked on each burst by comparison with logs that are encoded with a bit pattern. Further constraints not encoded in the burst lists are tuned also on the burst level. Events are then selected to be within the detector acceptance before then being identified as DIS Candidates, then DVCS event candidates, then events for which the Recoil Detector has taken good data.

4.2.1 Initial Data Quality

Initially the data quality is verified on the burst level. For this analysis the 32–bit pattern used was 0xfc1e1bdc, which corresponds to bits being set to (1) as described in Table 4.1.

In addition to using the bit pattern, the following additional data quality cuts were applied to the data, expressed using the HERMES ADAMO data table variables:

- The beam polarisation was not unphysical: `|g1Beam.rPolFit|` < 1.
- The TRD was operating in both spectrometer halves: `g1Quality.iTRDDQ`==3.
- A beam polarimeter was operational: `g1DAQ.bProdMethods` & 0x00800 != 0x00800.
- The luminosity rate was reasonable: 5 <`g1Beam.rLumiRate`< 10000.
- The beam energy was greater than 27 GeV: `g1Beam.rHeraElEnergy` > 27.

Bit	Description
2 & 30	Ensures the burst had a reasonable dead time for the main physics event trigger, Trigger–21. This trigger relates to the energy deposition in the calorimeter and hodoscopes.
3	Ensures the burst length was reasonable (< 11 seconds).
4	Ensures the beam current was reasonable ($5\text{mA} < I < 50$ mA), where the lower cut removes small count rates and the upper removes unphysical count rates.
6	Ensured the burst wasn't the first in a run, to exclude events recorded during the rise time of the detectors.
7	There are no bad μDST records in the burst.
8	There were PID values for the forward spectrometer available.
9	The burst was within a run marked as analysable in the logbook.
12	There is information available on the status of the experiment.
28	The beam polarisation measurement was made within 5 minutes of the burst.
17	There were no dead blocks in the calorimeter.
18	There were no dead blocks in hodoscope H2 or the luminosity monitor.
19	The TRD was fully operational.
20	There were no high voltage trips in the FCs or BCs.
26	Excludes bad events where the VC isn't operational. This ensures good tracking efficiency.
11	The recoil magnet was switched on, which is needed for recoil tracking.
27, 29 & 31	The components of the Recoil Detector (SSD, SFT and PD) were fully operational.

Table 4.1: Table summarising the bits that were set to 1 corresponding to the bit pattern used to check the data quality of the runs analysed in this thesis.

Since 2009, there is a new tracking algorithm developed for the HERMES forward spectrometer that was used in this analysis. It has been demonstrated that using the newer tracking method gives a consistent result [69]. For a DVCS analysis, where

we only require one track in the forward spectrometer, the following conditions are required:

- The option for "1 track to beam vertex" was set, which means only a single track in the forward spectrometer is used.
- The track flavour `_TF_HTC_UNBOUND_VERTEX_` is used, which means that the beam line was not used as a constraint in the fitting of the track.
- The fit probability to the track is > 0.01, to remove any obviously false tracks from the event sample.

In addition to the burst–level and track requirements above, the following geometrical requirements were imposed on the particles in the forward spectrometer:

- The tracked lepton originated from within the target cell: $5\,\text{cm} < \text{Z}_{\text{vertex}} < 20$ cm
- The transverse distance to the vertex is t_{vertex} <0.75 cm, to ensure that the event originates from within the target cell.
- The energy deposition of the lepton is measured within the calorimeter: $|x_{\text{calo}}| \leq 175\,\text{cm}$ and $30\ \text{cm} \leq |y_{\text{calo}}| \leq 108\ \text{cm}$.
- The polar angle between the virtual and real photon is $5\,\text{mrad} < \theta_{\gamma^\star\gamma} < 45\,\text{mrad}$. The lower limit is to ensure that the angle ϕ is still defined within the resolution of the calorimeter, and the upper limit is to ensure minimal background processes in the event sample [71].
- The lepton wasn't deflected by the septum plates, which is ensured by placing limits on the slopes (x_{slope} and y_{slope}) and spatial offsets (x_{offset} and y_{offset}) of the lepton track:
  $|x_{\text{offset}} + 172.04\tan\theta_x| < 31$ cm,
  $|y_{\text{offset}} + 181.0\tan\theta_y| < 7$ cm,
  $|y_{\text{offset}} + 383.0\tan\theta_y| < 54$ cm,
  $|x_{\text{pos}} + 108.0 x_{\text{slope}}| \leq 100$ cm,

$|y_{\text{pos}}+108.0y_{\text{slope}}| \leq 54$ cm.

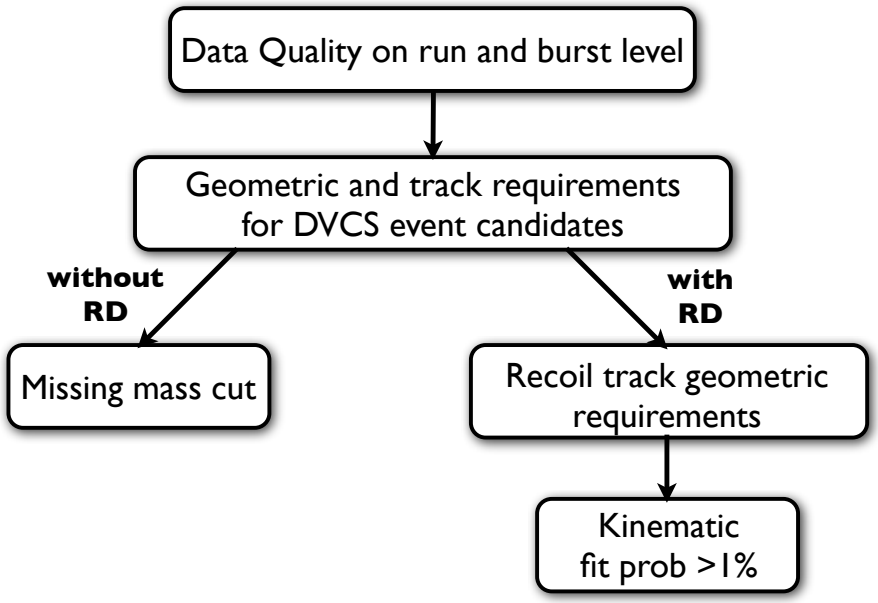

Figure 4.2: An overview of the data selection for a DVCS analysis with and without the Recoil Detector.

4.2.2 DIS Events

The DVCS event sample is a subset of the DIS event sample ($ep \to eX$), where exactly one lepton is tracked through the forward spectrometer meeting the following requirements:

- Identified as a positron: $2 <$ (`g1Track.rPID2` +`g1Track.rPID5`) < 100.
- Trigger–21 is fired, signifying that a physics event occurred in the detector.
- The scattered lepton has the same charge as the beam.
- The lepton is tracked by all the tracking detectors in the forward spectrometer : `g1Track.iSelect`&0x0200.
- $Q^2 >1$ GeV^2: selecting events in the DIS region and ensuring factorisation.

- $W^2 > 9$ GeV^2: which restricts the kinematic region in which the Monte Carlo fragmentation model operates. This model provides a reliable estimation of the background processed to be estimated in the event sample.

- $\nu < 22$ GeV: which eliminates events where virtual photon energy reconstruction was unreliable.

The kinematic distributions of W^2, Q^2 and ν are shown in Fig. 4.3 for the DIS events.

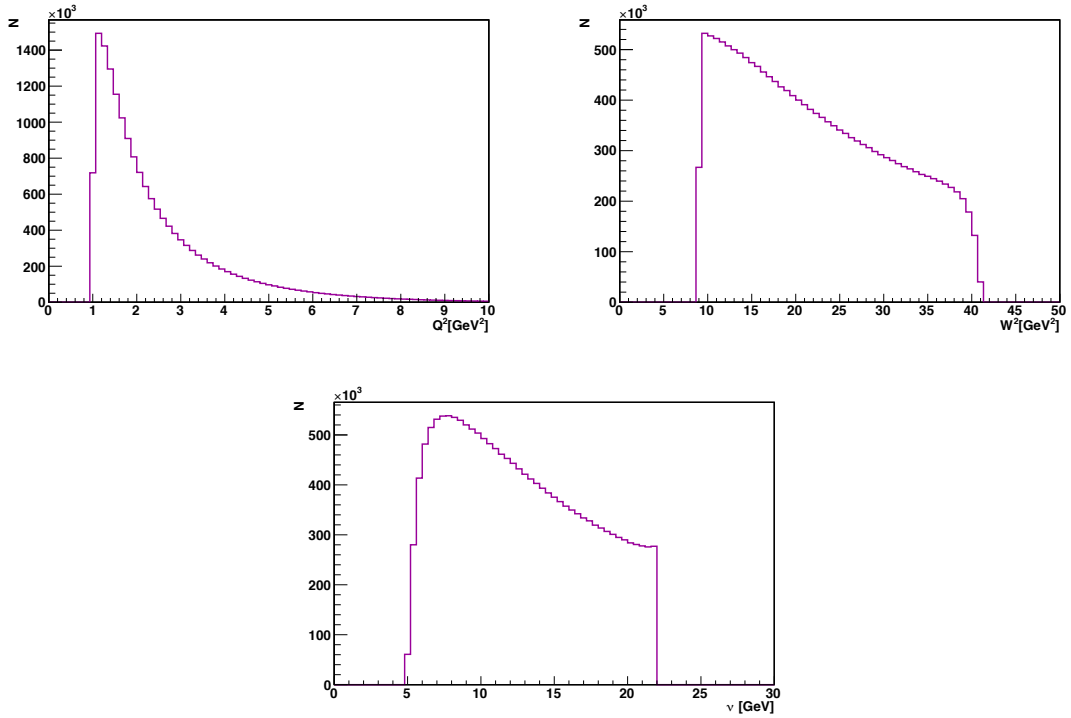

Figure 4.3: The distributions from left to right of Q^2, W^2 and ν for the DIS data samples for both 2006 and 2007.

4.2.3 Single Photon Events

After selection of the DIS lepton, the detection of a single photon in the calorimeter was required. The photon was measured using the following requirements:

- $E_\gamma > 5$ GeV, to ensure that background processes did not contaminate the event sample.

- 1 Mev $< E_{\text{preshower}} \leq 120$ MeV: the lower limit ensures the minimum energy required to produce an electromagnetic shower in the calorimeter, and the upper limit was to ensure that the energy was lower than the preshower overflow limit.

- $|x_\gamma| < 125\,\text{cm}$ and $33\,\text{cm} < y_\gamma| < 105\,\text{cm}$: to ensure that the photon was detected within the fiducial volume of the calorimeter.

The phrase Single Photon Events (SPEs) will refer to events that passed all of the above requirements.

4.2.4 DVCS Event Candidates

After selecting one DIS lepton and a photon, the following criteria are applied to select the DVCS event candidates:

- To clearly define the kinematic region $Q^2 < 10\,\text{GeV}^2$ and $0.03 < x_B < 0.35$.

- t_c <0.7 GeV^2 in order to reject background [71]

The exclusive event sample, before the use of the Recoil Detector, was selected by selecting events with a missing–mass consistent with the mass of the proton. The missing–mass window is calculated for a positron beam as $[(\mu - 3\sigma), (\mu + 3\sigma)]$ [40].

For the analysis in this thesis, the exclusive event sample is selected by taking all DVCS event candidates with a reconstructed recoiling proton. The selection of the recoiling proton track is described in the next section.

4.3 Selection of the Recoiling Proton

This section describes the criteria that are used to select a recoiling proton in the Recoil Detector (RD). In summary all DVCS event candidates with a positive reconstructed track in the RD are selected. These events are then fitted using kinematic fitting procedure for each DVCS event candidate with a track in the Recoil Detector. The track with the smallest kinematic fit χ^2 is then selected. The exclusive

DVCS event sample is then selected as the event with a kinematic fit χ^2 less than a specified value, this value corresponds to a fit probability greater than 1%.

4.3.1 Recoil Track Information

The recoil track information available has already been described in detail in Section 3.5.3.2 . To select candidate proton recoil tracks the following conditions for the tracks are required:

- Only tracks reconstructed using Method–7, described in Section 3.5.3.2.
- Track parameters are read from the proton hypothesis table.
- If there is no proton hypothesis available or the χ^2 of the track fit is > 100, the track parameters are read from the stopped proton hypothesis tables.
- If neither of the tables are available then the track parameters are read from the pion hypothesis tables.

The distributions of the recoil ϕ, θ and the z–vertex are shown in Figure 4.4 for DVCS candidate events with a positive recoil track. A single track per event is selected using the kinematic fitting routine. The ϕ angle distribution demonstrates clearly the quadrants of the RD. The rightmost quadrant in the plot (quadrant 1) has fewer events due to mis–calibration of the SSD, causing fewer pions to be reconstructed.

4.3.2 Kinematic Fitting

Once DVCS event candidates with a recoiling proton track in the Recoil Detector were selected, kinematic event fitting is used to select the final event sample. Kinematic fitting is a technique which was first introduced 50 years ago [72] for improving measurements.

For this analysis, the kinematic fitting routine [73] used all available information from the detected particles and combined using energy–momentum conservation under the hypothesis $ep \to ep\gamma$. There are several methods which can be used, in

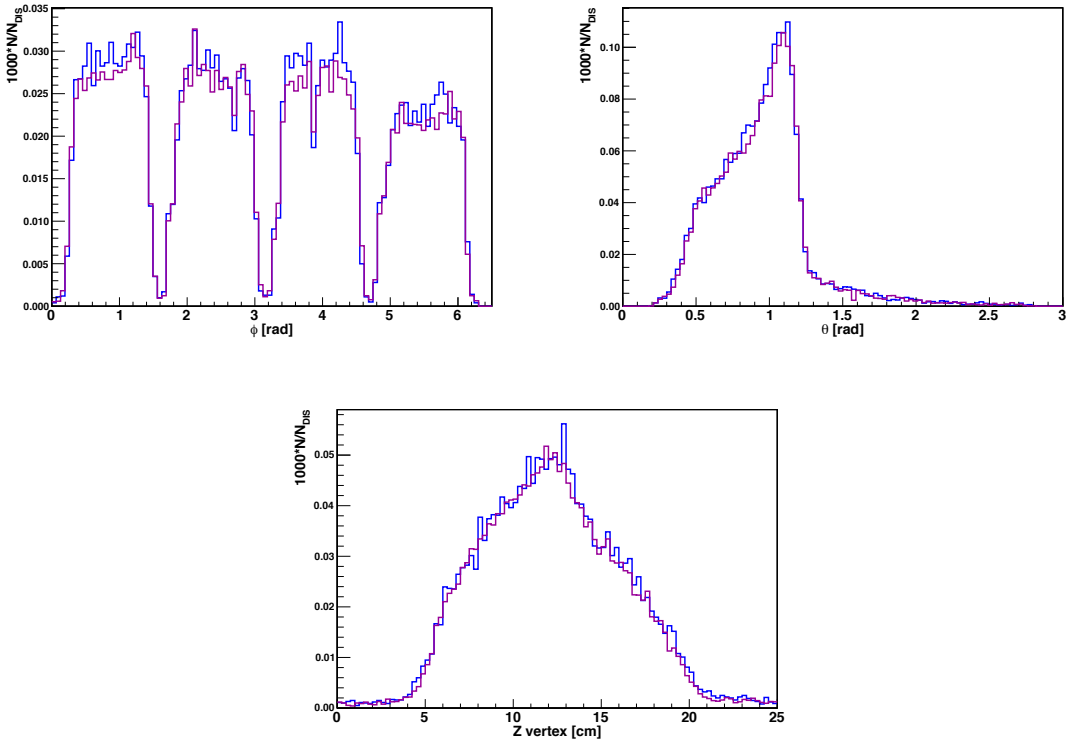

Figure 4.4: Kinematic distributions of the final DVCS candidate event sample with a positive recoil track for 2006 (blue) and 2007 (purple).

most cases Lagrangian multipliers are used to handle the constraints and then fitted. Once fitted, a new set of kinematic parameters (K^{fit}) are obtained. A χ^2 is then obtained to estimate the correctness of the fit:

$$\chi^2 = \sum_{i=0}^{n-1} \frac{(K_i^{\text{fit}} - K_i^{\text{meas}})^2}{\sigma_i^2}, \tag{4.14}$$

with the following conditions:

$$\begin{aligned} C_0 &= f_0(K_0^{\text{fit}}, K_1^{\text{fit}}, ...K_{n-1}^{\text{fit}}) = 0, \\ C_1 &= f_1(K_0^{\text{fit}}, K_1^{\text{fit}}, ...K_{n-1}^{\text{fit}}) = 0, \\ C_{m-1} &= f_{m-1}(K_0^{\text{fit}}, K_1^{\text{fit}}, ...K_{n-1}^{\text{fit}}) = 0, \end{aligned} \tag{4.15}$$

where f are functions of the kinematic parameters and K_i^{meas} and K_i^{fit} are the measured and fit kinematic parameters respectively, σ_i are the measurement errors, n

is the number of kinematic parameters and m is the number of kinematic constraints. In the case of DVCS, the following parameters were chosen in order to minimise correlations between parameters:

$$\begin{aligned} K_0 &= \tan(px_0/pz_0), \\ K_1 &= \tan(py_0/pz_0), \\ K_2 &= 1/p_0, \\ K_3 &= \tan(px_1/pz_1), \\ K_4 &= \tan(py_1/pz_1), \\ K_5 &= 1/p_1, \\ K_6 &= \phi_2, \\ K_7 &= \theta_2, \\ K_8 &= 1/(p_2 \cdot \sin\theta_2), \end{aligned} \tag{4.16}$$

where px_0, py_0, pz_0, p_0 are the x, y, z components and absolute value of the momentum of the scattered positron, px_1, py_1, pz_1, p_1 are the x, y, z components and absolute value of the momentum of the real photon and ϕ_2, θ_2 and p_2 are the azimuthal angle, polar angle and the absolute value of the momentum of the recoiling proton. There are four constraints, which are:

$$\begin{aligned} C_0 &= px_0 + px_1 + px_2 = 0, \\ C_1 &= py_0 + py_1 + py_2 = 0, \\ C_2 &= pz_0 + pz_1 + pz_2 = 0, \\ C_3 &= e_0 + e_1 + e_2 - e_{\text{beam}} - M_p \end{aligned} \tag{4.17}$$

where e_0, e_1, e_2 and e_{beam} are the energies of the scattered positron, photon recoil proton and beam positron respectively.

The minimisation of the χ^2 functions can be achieved via a method of penalty

functions [74], where penalty terms are added to the χ^2–function as follows

$$\chi^2 = \sum_{i=1}^{n} \frac{(K_i^{\text{fit}} - K_i^{\text{meas}})^2}{\sigma_i^2} + T\sum\nolimits_{j=1}^{m} \frac{C_j^2}{\sigma_{cj}^2}, \tag{4.18}$$

where σ_{cj} is the error of the j-th constraint and T is the penalty constant. If T is large enough, the constraints are automatically satisfied after the minimisation procedure.

The measurement errors were extracted from Monte Carlo generated datasets. The momentum dependence of the measurement errors were parameterised for electrons and photons measured in the forward spectrometer and protons detected in the Recoil Detector.

4.3.3 Selecting the Exclusive Data Sample

Events which are part of the DVCS candidate sample and had a recoil track are passed through the kinematic fitting routine as described above. The final event sample had only one further requirement. This is that the kinematic fit χ^2 of the event is less then 13.7, which corresponds to a fit probability $< 1\%$ (Figure 4.5). This requirement ensures a pure event sample (estimated to be greater than 99 % pure from Monte Carlo simulations).

To visualise how the sample is effected by this requirement one can consider the squared missing mass distribution shown in Figure 4.6 . The figure shows how the distribution changes once we require a positive track in the Recoil Detector, and finally once the final exclusive sample has been selected.

The comparison between data years, for the kinematic variables t, Q^2, x_B and ϕ are shown in Figure 4.7.

Two dimensional distributions showing the correlations between Q^2 and x_B and between x_B and t_c are shown in Figure 4.8 for all DVCS events in 2006 and 2007. A clear correlation is see between Q^2 and x_B in the plot on the left. No correlation is observed between x_B and t_c, and therefore no correlation would be expected between t_c and Q^2.

Previously it was mentioned that mandalstam variable t could also be calculated

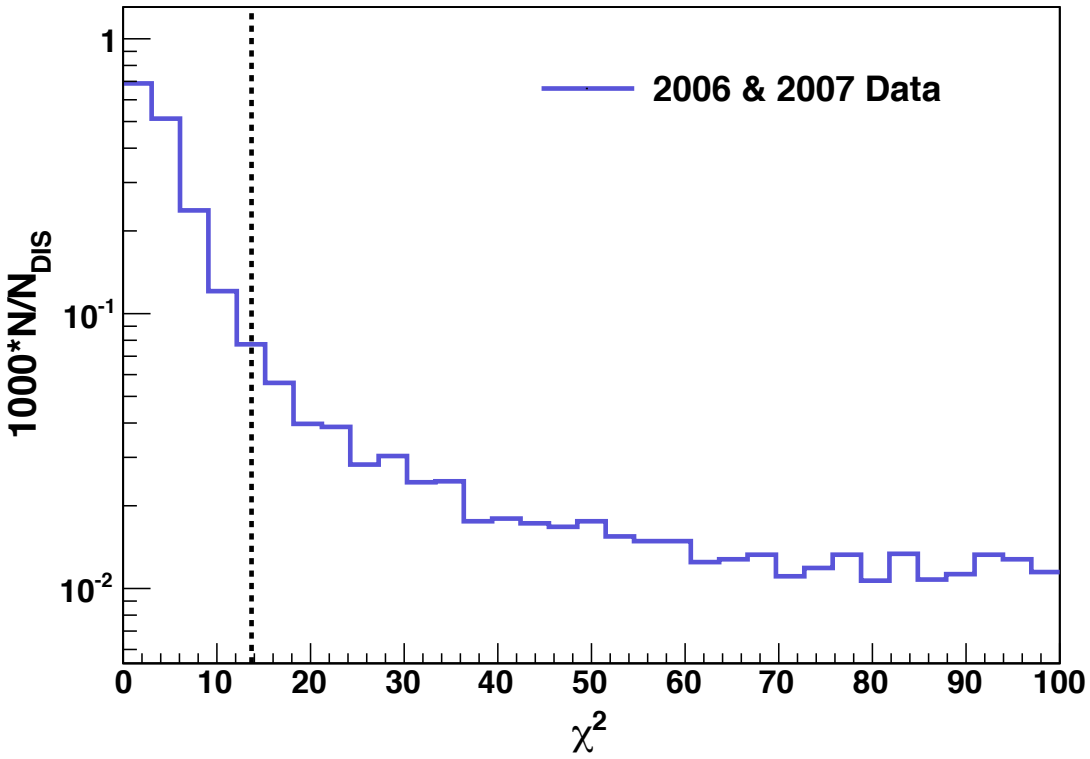

Figure 4.5: The distribution of the lowest χ^2 from recoil tracks from DVCS candidate events.

from the recoil detector information. Here Figure 4.9 shows the correlation between the the t calculated using the constrained method, t_c and using the information from the recoil detector t_{rd}.

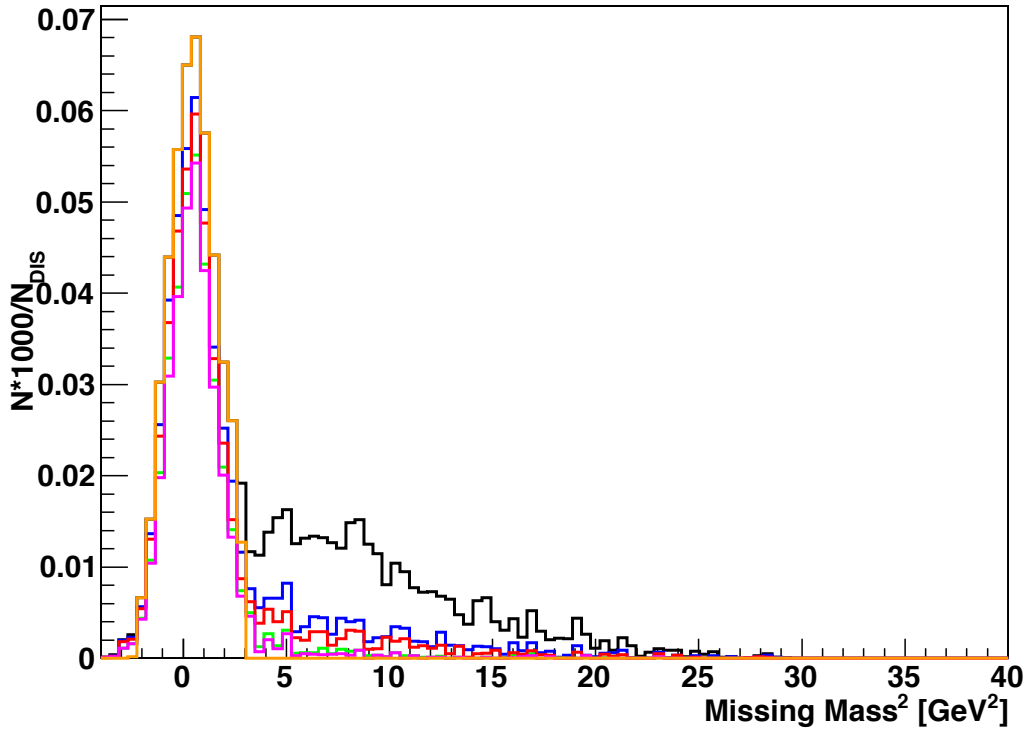

Figure 4.6: Black is DVCS candidate events not requiring a recoil proton. Blue requires a recoil proton in the Recoil Detector, red requires the cut on the quantity $0.5 < R < 1.5$ only, green is the cut on $\omega < 0.3$ only, and magenta requires both the coplanarity cuts. Orange requires no recoil proton, but with a missing mass cut, i.e. as the previous analysis

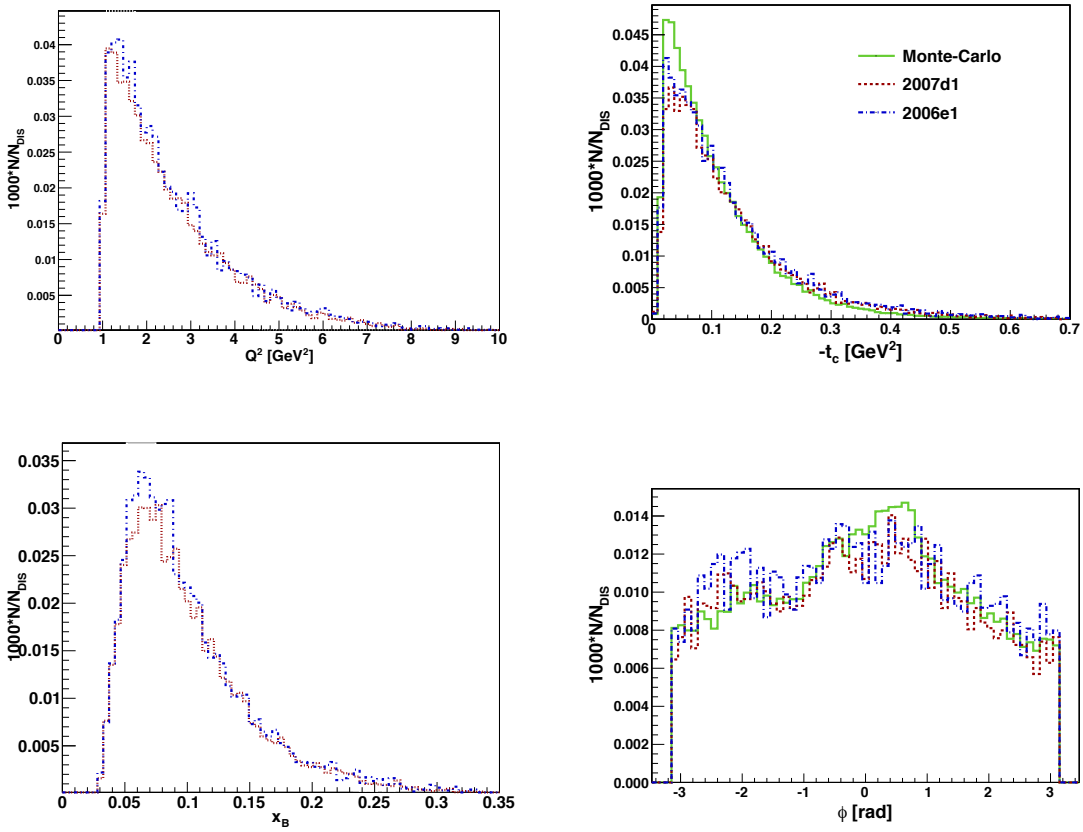

Figure 4.7: Kinematic distributions of the final DVCS event sample with recoil for 2006 (blue) and 2007 (red) and monte carlo (green).

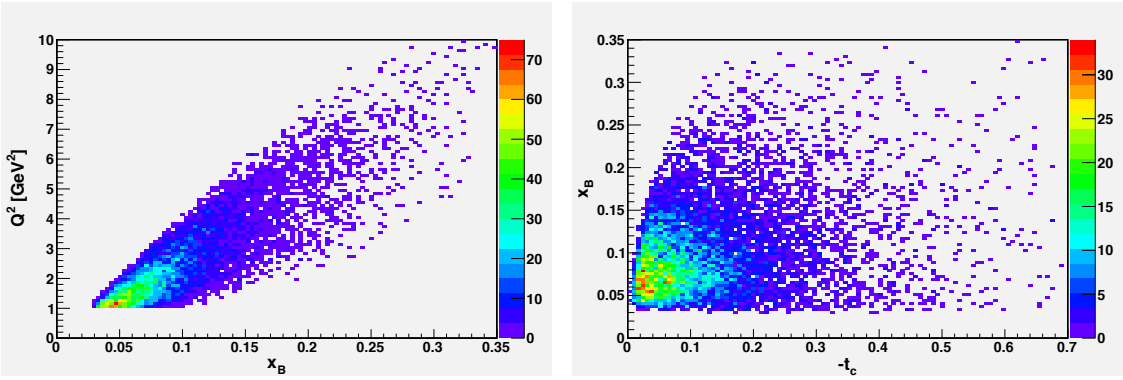

Figure 4.8: Two dimensional distributions showing the correlations between Q^2 and x_B (left) and between x_B and t_c(right).

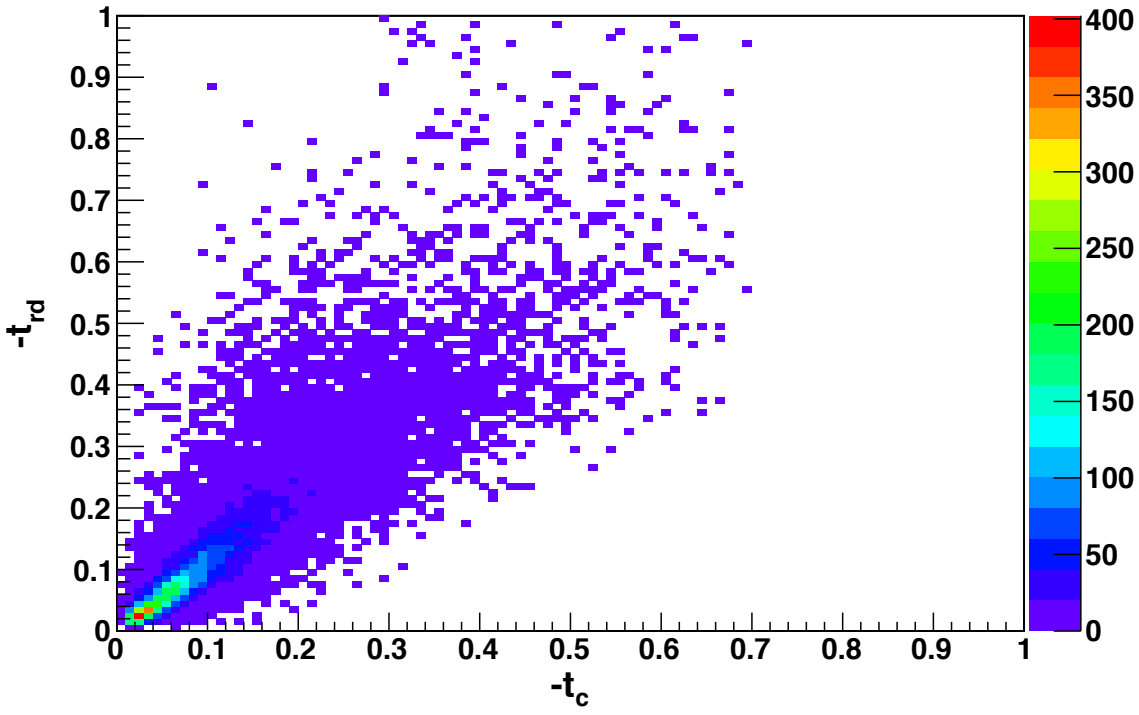

Figure 4.9: Correlation between t_c and t_{rd}, which shows that the two values are highly correlated.

4.3.4 Kinematic fitting vs 1-D cuts

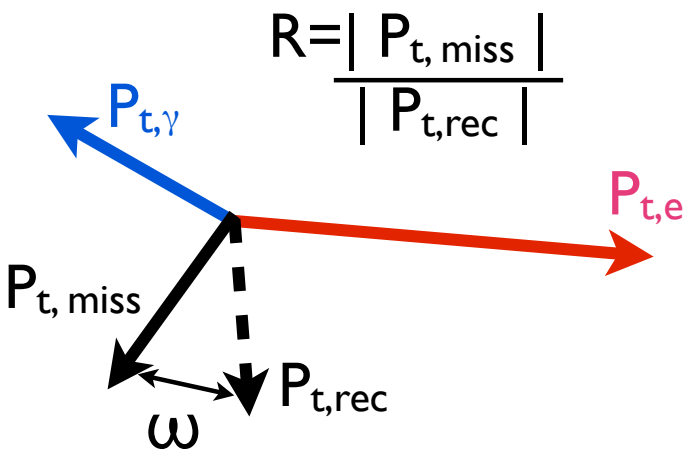

Figure 4.10: Definition of ω and R. The missing transverse momentum vector $p_{t,\vec{miss}}$, is reconstructed from the observed transverse momentum vectors of the real photon $p_{t,\vec{\gamma}}$ and the lepton, $p_{t,\vec{e}}$. The transverse momentum vector of the proton detected is $p_{t,\vec{rec}}$ [46]

Prior to the development of the kinematic fitting routine by S. Yaschenko for HERMES, the proposed method for the selection of events using the Recoil Detector was outlined in Ref. [46]. This section will show some of the studies undertaken to demonstrate that the kinematic fitting technique provided us with a good event selection technique and cleanest event sample.

The cuts were made on the quantities ω and R defined in Figure. 4.10 and shown in Figure 4.11.

For this study, the values determined from the Technical Design Report [46] from Monte Carlo simulations for these cuts are $w < 0.3$ and $0.5 < R < 1.5$.

Table 4.2 below provides the process fractions estimated from MC productions after the application of the 1–D cuts on the recoil proton track for DVCS candidate events. These cuts, plus a cut on squared missing mass of the proton, the recent analysis of the 2006–07 data set without use of the information form the RD [39], and from kinematic fitting. This analysis aims to extract a pure Elastic sample with minimal contributions from background processes. The process this analysis

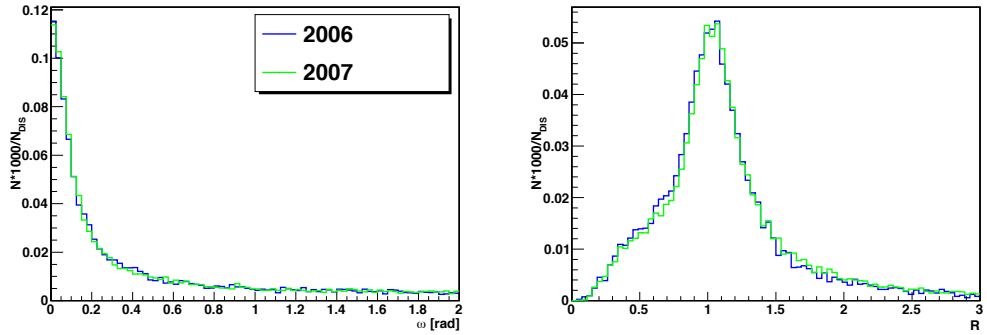

(a) ω (b) R

Figure 4.11: Distributions of the quantities ω (a), and R (b), for 2006 (blue) and 2007 (green).

is reducing the contribution from the Associated process. From Table 4.2 it can be seen that using kinematic fitting gives a very a very pure final event sample.

cuts	Assoc. BH	Elastic	SIDIS
ω and R	2.5%	94.2%	3.3%
ω, R and Missing Mass	2.3%	97.5%	0.2%
Analysis without RD [39]	11.4%	84.5%	3.7%
Kinematic Fitting	$< 1\%$	99%	$< 1\%$

Table 4.2: Fractions of the contributions of elastic BH, and background contributions from associated BH and semi inclusive processes to the sample for different selection of cuts for the recoil proton compared to a previous analysis [39] that did not make use of the Recoil Detector.

4.4 Extended Maximum Likelihood Method

The first DVCS results from HERMES were extracted using χ^2 fitting. The Maximum Likelihood method is used to extract the BHA amplitudes from the experimental data. This method minimises the fitting function to individual data points in order to avoid binning errors which would arise from other extraction methods e.g χ^2 fitting. The fitting function describes the theoretical dependence of the asymmetry on ϕ.

The Extended Maximum Likelihood (EML) method is used because it takes into

account that the data collected is a Poisson distribution [70].

For N sets of independent data points $x_i = -t, x_B, Q^2, \phi$, from a probability density function (p.d.f) $p(x;\theta)$, where θ is a set of m unknown parameters, the likelihood function is

$$\mathcal{L}(\theta) = \prod_i^N p(x_i;\theta). \tag{4.19}$$

By maximising the likelihood function the parameter set θ can be estimated. The observed number of events around the angle ϕ have a Poisson distribution about the expected value θ. To take this into account the maximum likelihood function is extended to include the p.d.f of the Poisson distribution, $\frac{\mathbb{N}^N \exp^{-\mathbb{N}}}{N!}$, to giving the EML function as,

$$\mathscr{L}(\theta) = \frac{[\mathbb{N}(\theta)]^N \exp^{-\mathbb{N}(\theta)}}{N!} \prod_i^N p(x_i;\theta). \tag{4.20}$$

Here, N is the expected number of events and $\mathbb{N}(\theta)$ can be interpreted as the normalisation of the extended p.d.f $\mathscr{P}(x;\theta) \equiv p(x;\theta)\mathbb{N}(\theta)$, i.e,

$$\mathbb{N}(\theta) = \int \mathscr{P}(x;\theta)dx. \tag{4.21}$$

A large product of small numbers may lead to rounding errors during the asymmetry extraction. To avoid this, the negative log-likelihood method is instead minimised to prevent this problem. The negative log–likelihood function to is

$$-\ln \mathscr{L}_{\mathrm{EML}}(\theta) = -\sum_i^N \ln \mathscr{P}(x_i;\theta) + \mathbb{N}(\theta). \tag{4.22}$$

For the extraction of the BHA, the extended p.d.f of the total observed events in x and P is

$$\mathcal{N}(x;P;\theta) = \mathcal{L}(P)\epsilon(x,P)\sigma_{UU}(x)[1 + PA_{\mathrm{LU}}(x;\theta)], \tag{4.23}$$

where $\mathcal{L}$ is the integrated luminosity, ϵ is the detection efficiency and σ_{UU} is the cross section for the unpolarised target. The normalisation is

$$\mathbb{N}(\theta) = \iint \mathcal{N}(x,P,\theta)dxdP, \tag{4.24}$$

and the standard p.d.f is

$$p(x; P; \theta) = \frac{\mathcal{N}(x, P; \theta)}{\mathbb{N}(\theta)}. \tag{4.25}$$

Therefore the negative log–likelihood function which is minimised during the extraction is given as

$$-\ln \mathscr{L}_{\mathrm{EML}}(\theta) = -\sum_{i}^{N} \ln[1 + P_i A_{\mathrm{LU}}(x_i; \theta)] + \mathbb{N}(\theta). \tag{4.26}$$

The following is the fit function used to extract the the BHA:

$$A_{\mathrm{LU}}(\phi) = A_{\mathrm{LU}}^{cos(0\phi)} + A_{\mathrm{LU}}^{sin\phi} sin(\phi) + A_{\mathrm{LU}}^{\sin 2\phi} \sin(2\phi). \tag{4.27}$$

The number of DVCS events at HERMES is constrained by the data taking periods and the luminosity. Studies have shown that samples with limited statistics that EML is the most suitable because the normalisation is not dependent on a fixed number of events [75].

In order to check whether including an additional $\cos\phi$ term in the fit function modifies the result, the beam-helicity asymmetry amplitudes for a 3– and 4–parameter fit are compared in Figure 4.12. Across all the kinematic bins for the leading $\sin\phi$ amplitude, no difference is observed between the two extractions. Most differences are observed in the $\sin(2\phi)$ term because it is more closely correlated with the $\cos\phi$ term. Because the additional term makes no difference to the final result, the 3–parameter fit will be used throughout the remainder of the thesis.

4.4.1 EML vs a χ^2 fitting

The data is fitted using a maximum likelihood fit rather than a χ^2 fit because EML provides an unbinned fit in ϕ, and therefore should be free of binning effects in phi. Also, EML is advantageous if the normalisation of the data set is not straight forward. One disadvantage of EML is that it does not provide an obvious measure of goodness of fit. A χ^2 fit does and has been the standard fitting technique used for many analyses in physics. Fig. 4.13 shows the comparison between a χ^2 and an EML fit of the same data with a 3 parameter fit function. This figure shows that the

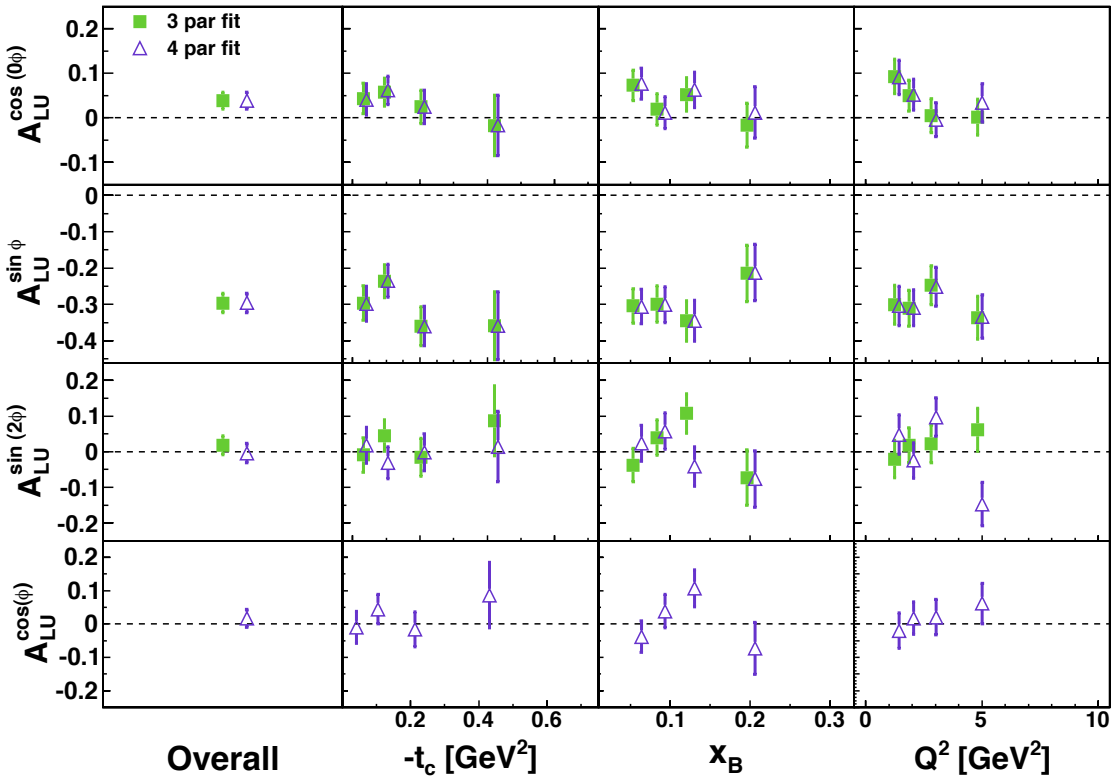

Figure 4.12: Comparison of the beam-helicity asymmetry amplitudes for different fitting functions (see text for details).

results obtained via both fitting techniques are comparable. Due to the advantage of a fitting technique free of binning effects the EML fit was chosen.

	$A_{LU}^{\cos 0\phi}$	$A_{LU}^{\sin\phi}$	$A_{LU}^{\sin 2\phi}$
EML	0.0395 ± 0.0190	-0.2960 ± 0.0268	0.0175 ± 0.0267
χ^2	0.0337 ± 0.0280	-0.2897 ± 0.0213	0.0270 ± 0.0233

Table 4.3: Comparison of χ^2 and EML fitting.

4.5 Cross Check of the Data Selection

To verify that the selection of the DVCS event sample was performed correctly, a cross check was performed with Caroline Reidl and Sergey Yaschenko both of DESY, Zeuthen. The number of DIS and DVCS events agree well. The discrepancies arise due to different levels of precision used by the analysers. The results of the cross check are shown in Table 4.4

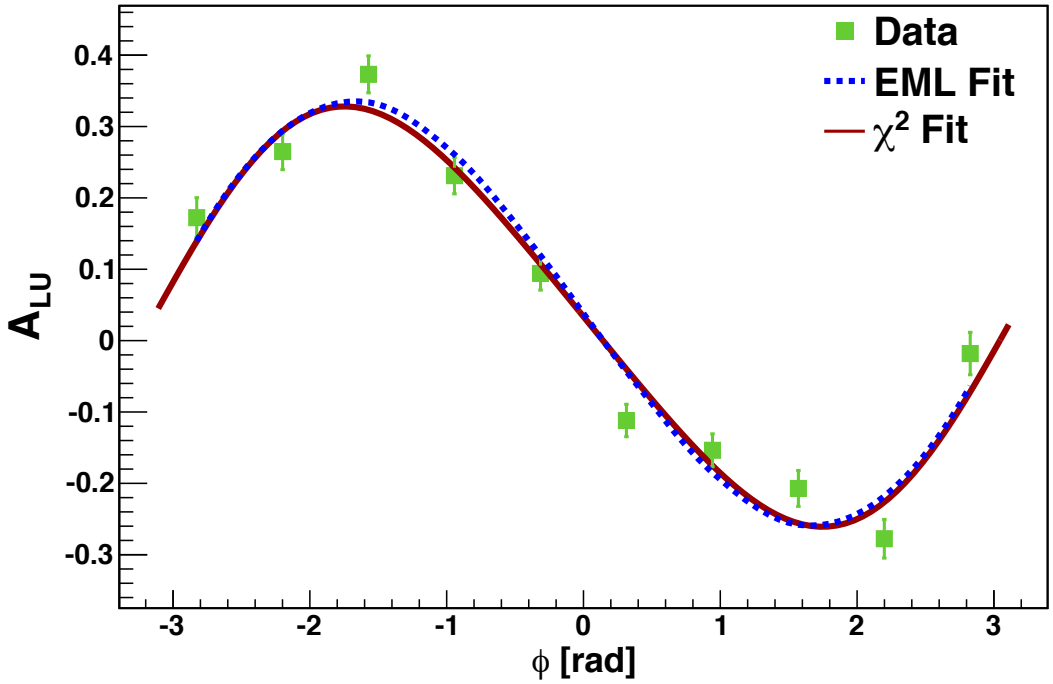

Figure 4.13: Comparison of the beam-helicity asymmetry for different fitting methods (see text for details).

	beam helicity = +1 (→)			beam helicity = -1 (←)			
	DIS	DVCS	with RD	DIS	DVCS	with RD	
2006	7,885,897	11,573	4,860	2,134,787	3,154	1,306	This Work
	7,818,554	11,497	4,888	2,116,180	3,129	1,303	C. Riedl
	7,873,911	11,570	4,888	2,131,729	3,154	1,308	S. Yaschenko
2007	9,290,370	13,690	5,539	7,733,025	10,641	4,322	This Work
	9,271,008	13,684	5,545	7,717,459	10,634	4,330	C. Riedl
	9,275,842	13,685	5,537	7,721,857	10,635	4,318	S. Ysachenko

Table 4.4: Cross check of event samples

4.6 HTC vs HRC

Previously, it was stated that HTC track fitting in the forward spectrometer is used for this analysis. Figure 4.15 shows the asymmetry amplitudes extracted from data produced using each of the HRC and HTC track fitting methods. Both track fitting methods have consistent asymmetry amplitudes across all the kinematic bins, and so the result is not dependent on the tracking method used to reconstruct forward tracks. However, larger statistical uncertainties are observed for the result using

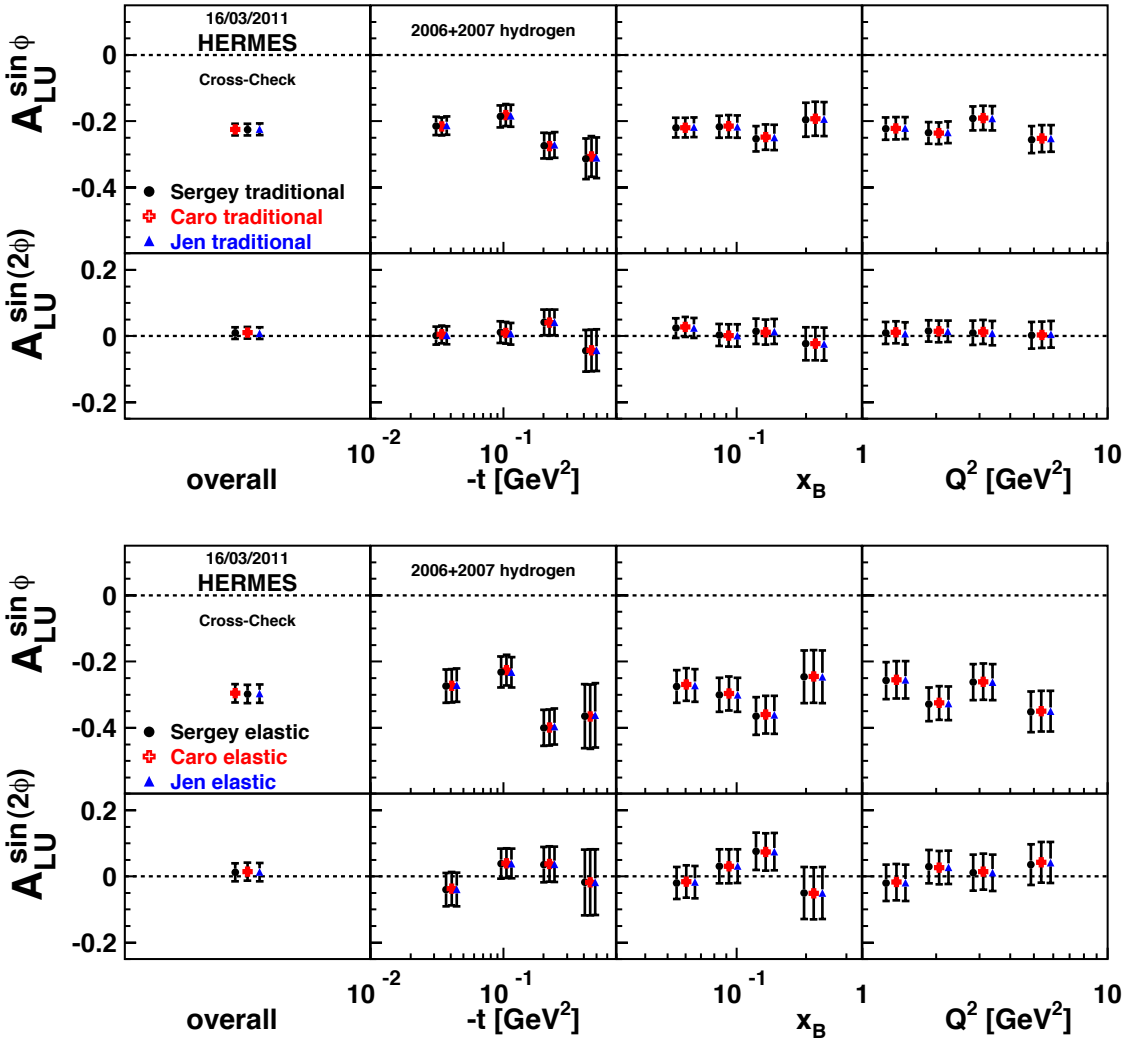

Figure 4.14: Comparison of the beam-helicity asymmetry amplitudes from three independent analysers, including the author of this work. The results are all in excellent agreement. [69].

HTC as there is a loss of 10% in statistics when HTC tracking parameters are used (due to the track probability cut $> 1\%$). No significant difference is seen, therefore the results from lepton tracks fitted using the more sophisticated HTC tracking method can be compared with the results previously published.

4.7 Recoil PID

The recoil PID (rdPID) has already been described in detail in Section 3.5.4.2. It was envisaged that it would be used to distinguish between pions and protons, however

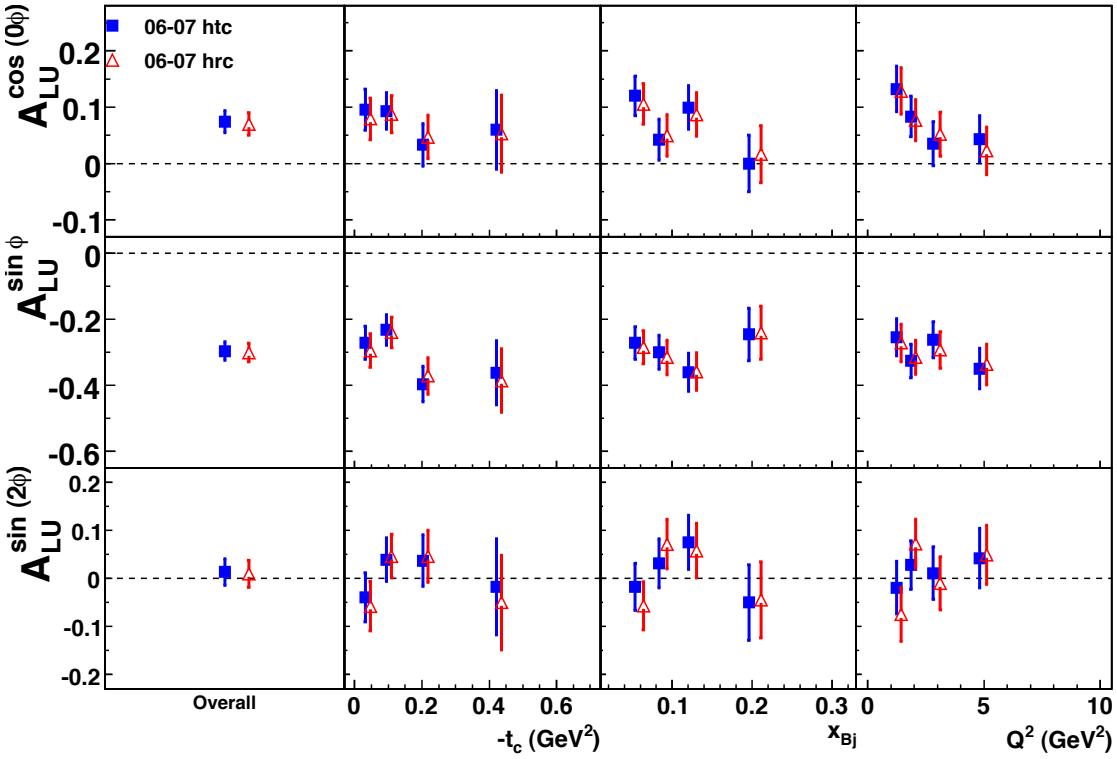

Figure 4.15: The asymmetry amplitudes expected for an analysis of the beam–helicity amplitude in the pure elastic sample extracted using each of the HRC and HTC track fitting methods.

since the use of kinematic fitting it has been demonstrated that it is superfluous for the analysis.

The distinction between protons and pions would be made as described previously. Figure 4.16 shows the Recoil track momenta versus the rdPID values for each quadrant from a sample of 2007 data of single photon events. Negative values of rdPID are generally expected to be pions, and particles with positive rdPID values are expected to be protons. The plots show two peaks in the distributions, one corresponding to protons for positive values of rdPID and one for pions at negative values of rdPID. At higher values of track momenta ($> 0.65\,\mathrm{Gev/c^2}$) there is increasing mixing between the protons and pions, as expected [68].

With the use of kinematic event fitting, it is shown that a rdPID cut has a negligible effect on the final result. Figure 4.17 shows the rdPID values of tracks selected by kinematic event fitting. It shows that the number of events with rdPID values below 0 for the event sample selected are few.

Possible values for an rdPID cut were rdPID > -2 cuts away 1.5% of statistics, rdPID > -1 cuts away 2.1% of statistics and rdPID > 0 cuts away 3.2% of statistics. Cutting away such a small percentage had a negligible effect on the asymmetry amplitude values, as shown in Fig. 4.18.

In conclusion, the a cut on the rdPID has a negligible effect on the final result it was not used for the final analysis.

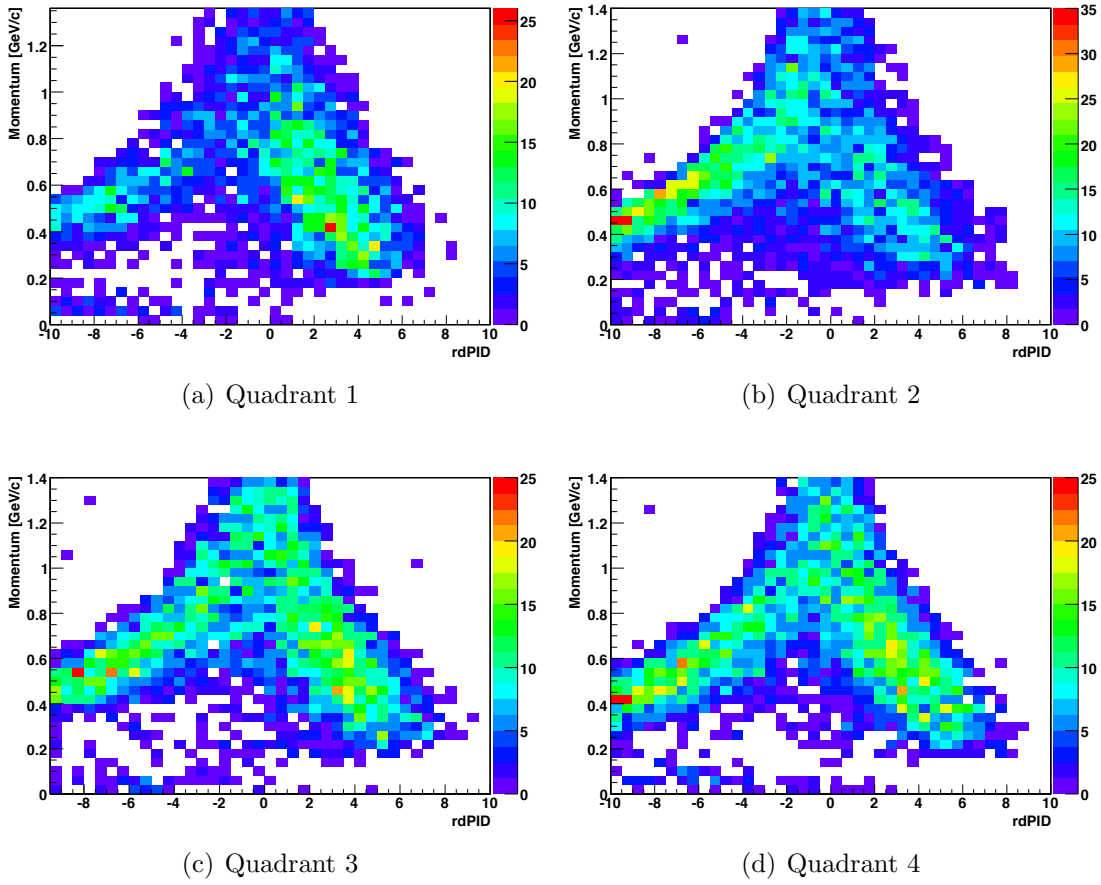

(a) Quadrant 1

(b) Quadrant 2

(c) Quadrant 3

(d) Quadrant 4

Figure 4.16:

Momentum (in GeV/c) vs. rdPID values for each quadrant of the Recoil Detector. For every Single Photon Event, the Recoil track with the smallest χ^2_{elastic} is filled into the histograms.

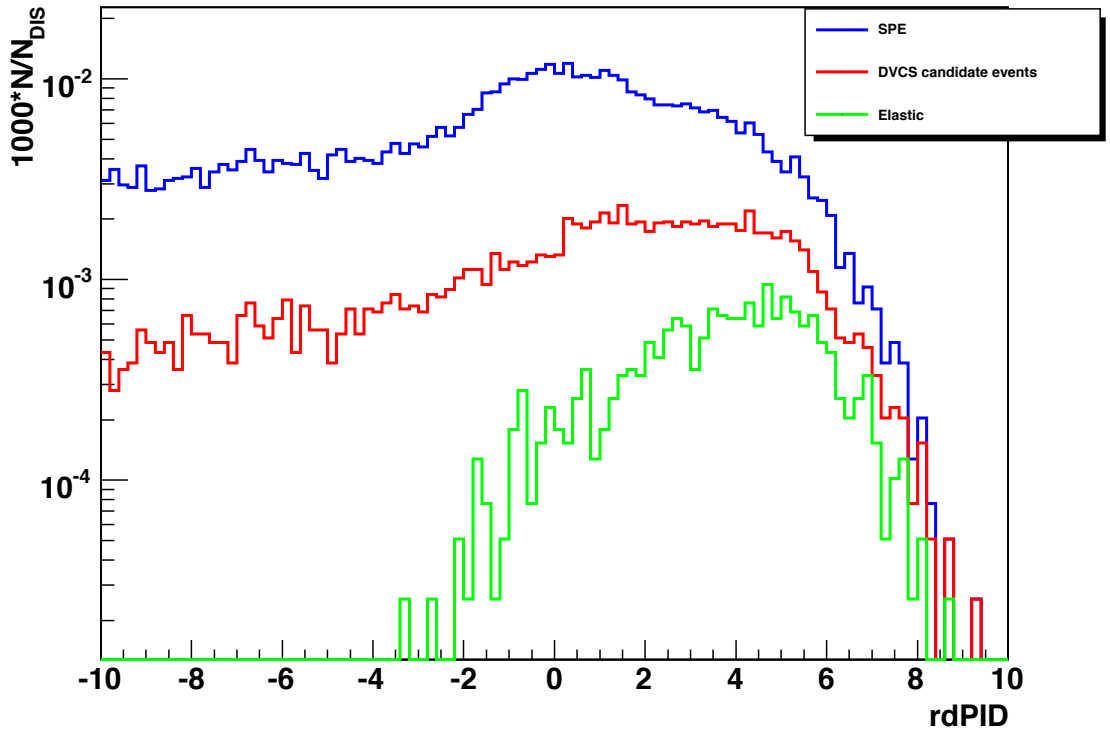

Figure 4.17: The rdPID distributions for data selected as single-photon events (blue), traditional DVCS events (red) and pure elastic events (green). The distribution for the pure elastic sample drops to zero as rdPID values become negative.

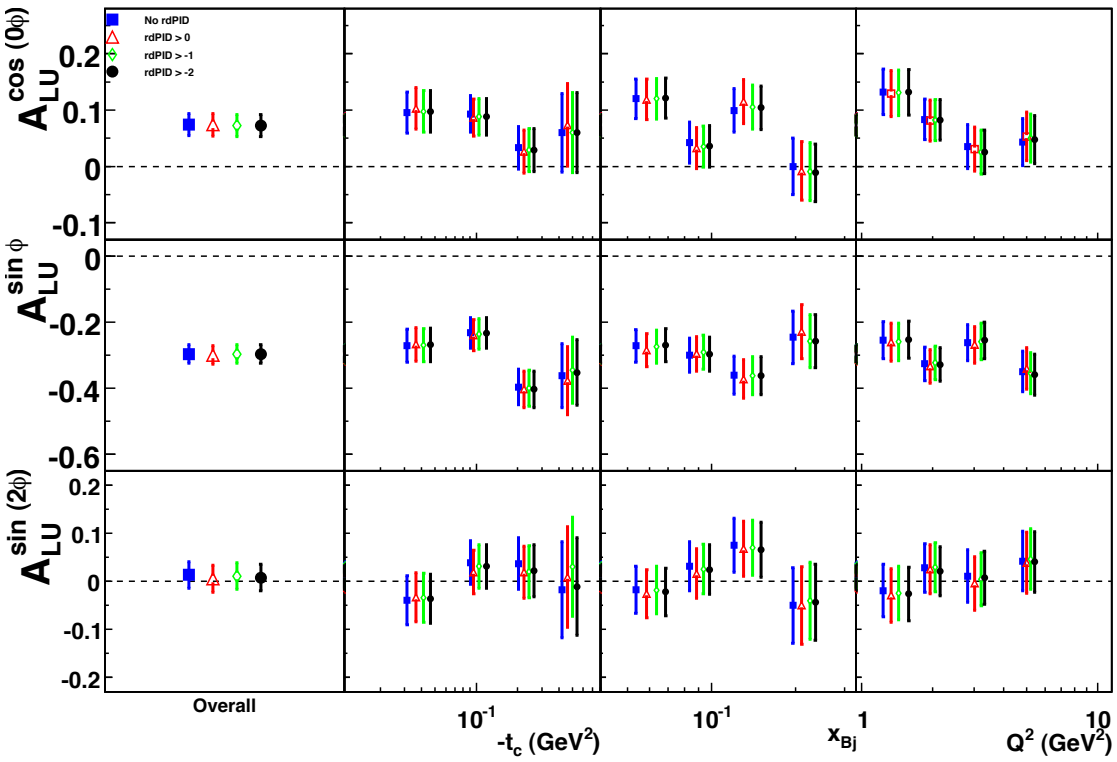

Figure 4.18:

Comparison of the effect of the cut on the rdPID on the amplitudes of the pure elastic DVCS beam-helicity asymmetry, where only the rdPID cut was varied for each point.

Chapter 5

Systematic Uncertainties

There are several possible sources of systematic uncertainties that affect the result presented in this thesis. This chapter will provide details of the systematic studies undertaken.

5.1 Low and High Target–Density Operation

During the data taking period considered in this thesis, there were periods at the end of a beam fill when the target density was increased. The periods with normal operating conditions will be referred to as "low density runs" (4.9×10^{14} nucleons/cm^3), and "high density runs" refers to the higher density runs at the end of a fill with a target density of 3.1×10^{15} nucleons/cm^3 [53].

To determine if any systematic effect occurred due to the different target densities, the beam helicity–asymmetry was extracted for both run periods. No significant difference is observed and is plotted in Fig. 5.1.

5.2 Time Dependence of Helicity Amplitudes

Due to the long period of data taking, it is possible that uncertainties could have arisen due to changes in the yield of events detected over the data taking period analysed in this thesis. This could affect the consistency of the result obtained, and if present would need to be taken into account.

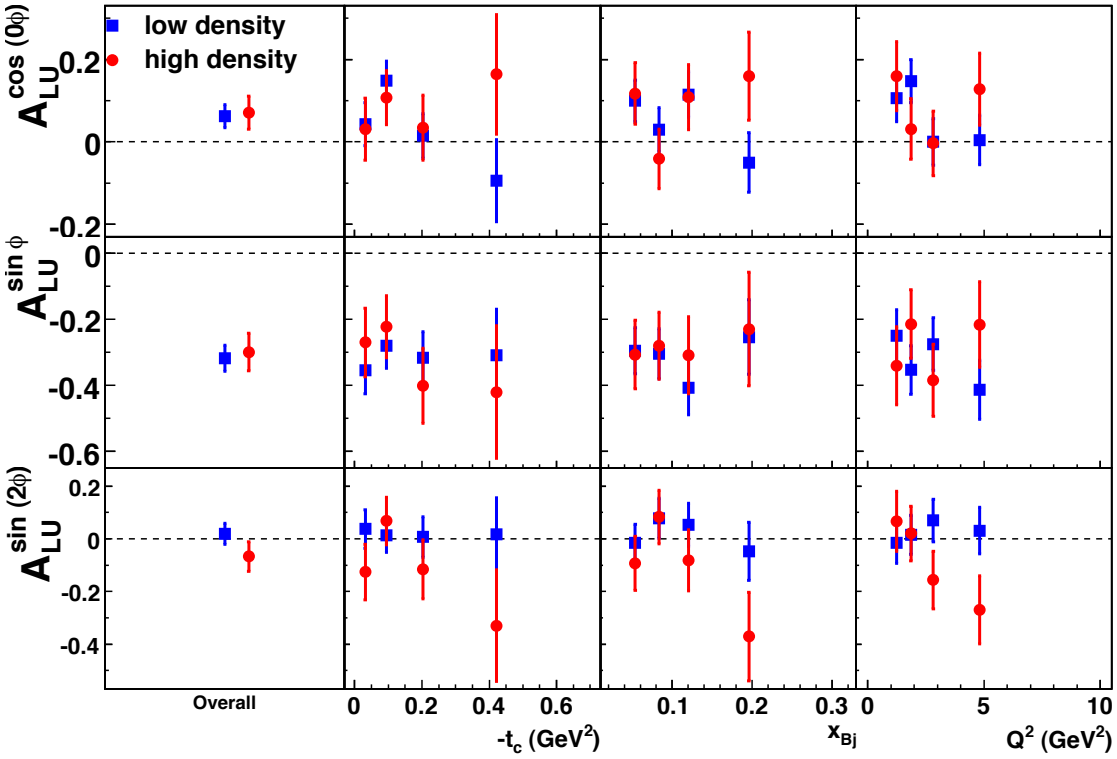

Figure 5.1: The pure elastic beam-helicity asymmetry amplitudes extracted for each of the low and high target gas density data sets. No significant difference is observed between the two data sets and so no systematic uncertainty is assigned.

To study the effect over time the BHA was extracted for 2006, and tow time periods in 2007. For one time period in 2007 of the c2 production a larger constant term was observed in the upper plot of Figure 5.2 for 2007c2(a). This coincided with a drop in yield of measured DVCS events [69]. This was no longer a problem in the newest data production 2007d1, shown in the lower plot of Figure 5.2. Here the constant term is consistent with zero for all time periods.

5.3 Background

Previous analyses using the missing mass technique were shown to to contain significant contributions from background processes. It contains contributions from three background process: associated production, where the BH/DVCS process involves an intermediate excitation of the proton into a Δ resonance, semi-inclusive

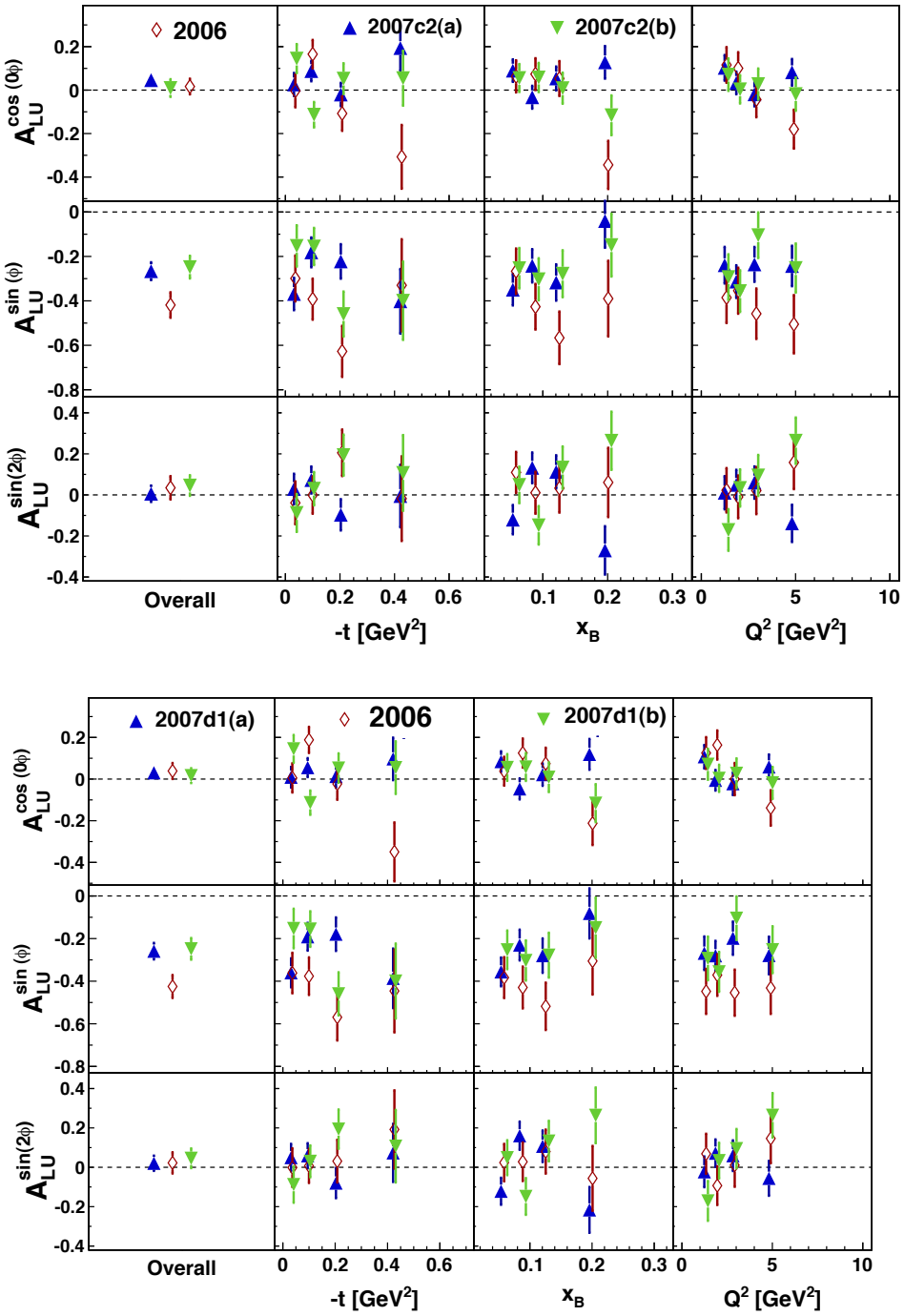

Figure 5.2: The amplitudes of the beam-helicity asymmetry extracted in three different time bins for two data productions of 2007 (c2 top and d1 lower). 2007(a) excludes an observed low yield period in 2007c2 productions and 2007(b) is the bsa extracted from the low yield period. See text for more details.

DIS processes (SIDIS) producing mostly π^0 and η mesons, and from exclusive π^0 production.

The contribution from the associated production is mostly removed by measuring the recoiling proton. Events from meson production can still be present in the data sample when only one of the photons from the decay of the meson remains in the acceptance of the forward spectrometer, or both photons are Lorentz boosted into a single cluster in the calorimeter.

If there are N background processes with the corresponding asymmetries A_i are known, corrections can be made to the extracted amplitudes

$$A_{BH/DVCS} = \frac{1}{f_{BH/DVCS}}\Big(A_{\text{measured}} - \sum_{i}^{N} f_i A_i\Big), \tag{5.1}$$

where f_i is the fractional contribution from background process i. To estimate the fraction of background in the event sample MC studies were preformed. A MC simulation using a parameterisation of the form factor for the resonance region from Ref. [76] and individual cross sections for the single-meson decay channels calculated using the MAID 2000 programme [77]. Each process is identified using the criteria:

- BH/DVCS:`g1MEvent.XTrue` $= 1$,
- Associated BH: `g1MEvent.XTrue` < 1 and `g1MEvent.W2True` < 4,
- Semi-inclusive π^0: `g1MEvent.XTrue` < 1 and `g1MEvent.W2True` > 4

where `XTrue` and `W2True` represent the values of x and W^2 generated in MC. The reconstructed event data (where generated events are passed through a simulation of the HERMES experimental set up) were then analysed to see the contribution of each process in the final event sample.

The fractional contribution is then calculated as

$$f_{\text{process}} = \frac{\sum_{i}^{N_{process}} w_i}{\sum_{i}^{N} w_i}, \tag{5.2}$$

where w_i is the MC event weight of an exclusive event i, passing all DVCS event requirements and $N_{process} \in N$. For each kinematic bin it has been shown that a

MC– weighted quantity $\sigma = \sum_i^N w_i$ has an uncertainty $d\sigma = \sqrt{\sum_i^N w_i^2}$ [78]. The values are presented in Table 5.1 for the final event sample using the Recoil Detector. Figure 6.2 shows the precess fractions for the analysis using the Recoil Detector, compared to an analysis using the missing mass technique for each background process. The exclusive pion fraction for this data set is considered to be negligible for the analysis using the Recoil Detector, because it was also very small (0.4 %) for the analysis using the missing mass technique [39].

Kinematic Bin	Elastic BH	Assoc. BH	Semi-Inc. DIS
Overall	99.9 %	< 0.1 %	< 0.1 %
$-t \leq 0.06$	99.9 %	< 0.1 %	0.0 %
$0.06 < -t \leq 0.14$	99.9 %	< 0.1 %	< 0.1 %
$0.14 < -t \leq 0.30$	99.9 %	< 0.1 %	< 0.1 %
$0.30 < -t \leq 0.70$	99.8 %	0.1 %	< 0.1 %
$0.03 < x_B \leq 0.07$	99.9 %	< 0.1 %	0.0 %
$0.07 < x_B \leq 0.10$	99.9 %	< 0.1 %	< 0.1 %
$0.10 < x_B \leq 0.15$	99.9 %	< 0.1 %	0.0 %
$0.15 < x_B \leq 0.35$	99.8 %	0.1 %	< 0.1 %
$1.0 < Q^2 \leq 1.5$	99.9 %	< 0.1 %	0.0 %
$1.5 < Q^2 \leq 2.3$	99.9 %	< 0.1 %	0.0 %
$2.3 < Q^2 \leq 3.5$	99.9 %	< 0.1 %	< 0.1 %
$3.5 < Q^2 \leq 10.0$	99.8 %	0.1 %	< 0.1 %

Table 5.1: Fractional contributions of the processes present in the exclusive event sample for each bin in $-t$, Q^2 and x_B. These were estimated from MC simulations.

The contribution from SIDIS, has been shown that 80% of SIDIS events are from π^0 production, which then decays into two photons [79], and the remaining 20% are from η decay.

The contribution from SIDIS can be corrected for by extracting the corresponding asymmetry from data, but with 2 photons in the forward spectrometer. However for the Recoil Detector, as there were limited statistics, an asymmetry could not be extracted. Therefore a value of $0 \pm \frac{2}{\sqrt{12}}$ was chosen to correspond to one standard deviation from a uniform distribution in the range $[-1, 1]$.

The final background corrected asymmetry was then determined for each kine-

matic bin as,

$$A_{\text{corr}} = \frac{A_{\text{meas}} - f_{\text{SIDIS}} A_{\text{SIDIS}}}{1 - f_{\text{SIDIS}}}, \tag{5.3}$$

where f_{SIDIS} is the fraction and A_{SIDIS} is the asymmetry amplitude of the SIDIS π^0.

There are three uncertainties which arise from the background correction of the asymmetry amplitudes. The first is the contribution to the statistical uncertainties arising from the small statistical uncertainties in the process fractions from Monte Carlo simulations. The second is a contribution from the statistical uncertainty of the background asymmetry amplitudes, which is given as $\pm \frac{2}{\sqrt{12}}$. And finally a contribution to the systematic uncertainties of the data , equal to the difference between the measured and corrected amplitudes,

$$\delta_{\text{bg,sys}} = \mid A_{\text{corr}} - A_{\text{meas}} \mid. \tag{5.4}$$

5.4 3–in–1 Systematic Uncertainty

Uncertainties which arise from the spectrometer acceptance and alignment, smearing and finite bin width have been studied extensively for previous HERMES DVCS analyses [40]. The technique used is referred to as the "3–in–1" method. The effects are described in detail as:

- **Acceptance :** The experimental set up does not provide 4π angular coverage. The effect of the limited coverage was taken into account for model comparisons.

- **Smearing :** This arose from the limited resolution of the calorimeter. The smearing is a result of an uncertainty in determining the interaction position of a particle within the calorimeter. This can have adverse effects on the reconstructed kinematics, and therefore an uncertainty in the extracted asymmetry amplitudes is introduced.

- **Finite Bin Width :** The fitting procedure does provide an unbinned fit in ϕ, however, the asymmetry amplitudes are presented in bins of $-t$, x_B and

Q^2, at the average kinematics of each bin. This results in events smearing into adjacent bins due to finite detector resolutions.

The systematic uncertainty was determined using a Monte Carlo simulation of the detector setup. The asymmetry amplitudes were produced using a fast VGG simulation [80]. The simulation calculated the asymmetry amplitudes directly from the Fourier coefficients and VGG models of GPDs. Five variants of the VGG models were used, these include different combinations of skewness, t-ansatz, b parameter and the D–term as summarised in Table 5.2. The asymmetry amplitudes are free from any detector or binning effects.

Model	Factorised t-ansatz	Skewness	b Parameter	D–term
1	✓	X	-	X
2	✓	✓	1	X
3	✓	✓	∞	X
4	✓	✓	1	✓
5	✓	✓	∞	✓

Table 5.2: Table summarising the contribution of the factorised t–ansatz, skewness, b parameter and D–term to each VGG model.

A set of Monte Carlo events were generated using the input from the fast VGG simulation for the five models, and propagated through a simulation of detectors. These MC events were then analysed in the same manner as the data, were all DVCS/BH events were required to pass the same exclusivity requirements. From this the 'reconstructed' asymmetry amplitudes are extracted for each model, using EML. The amplitudes were extracted for each kinematic bin as a function of the model specific weight, w, using the following fit function:

$$-\ln \mathscr{L}(\theta) = -\sum_{i}^{N} w^2 \ln[1 + \mathscr{P}_L \mathscr{A}_{\mathrm{UL}}(x_i;\theta)] + \mathscr{N}(\theta, w^2). \tag{5.5}$$

The systematic uncertainty arising from the ith model is

$$\delta_i = |A_{\mathrm{generated}} - A_{\mathrm{reconstructed}}|, \tag{5.6}$$

where generated asymmetry amplitudes are calculated from the corresponding GPD-parameterisation at the same average kinematics of each bin. The combined systematic uncertainty from the 5 models was calculated as:

$$\delta_{3\text{in}1} = \sqrt{\frac{1}{5}\sum_{i}^{5}\delta_i^2}. \tag{5.7}$$

The final 3–in–1 systematic uncertainty is presented in Figure 5.4, also showing the average reconstructed and generated asymmetry amplitudes of all five models.

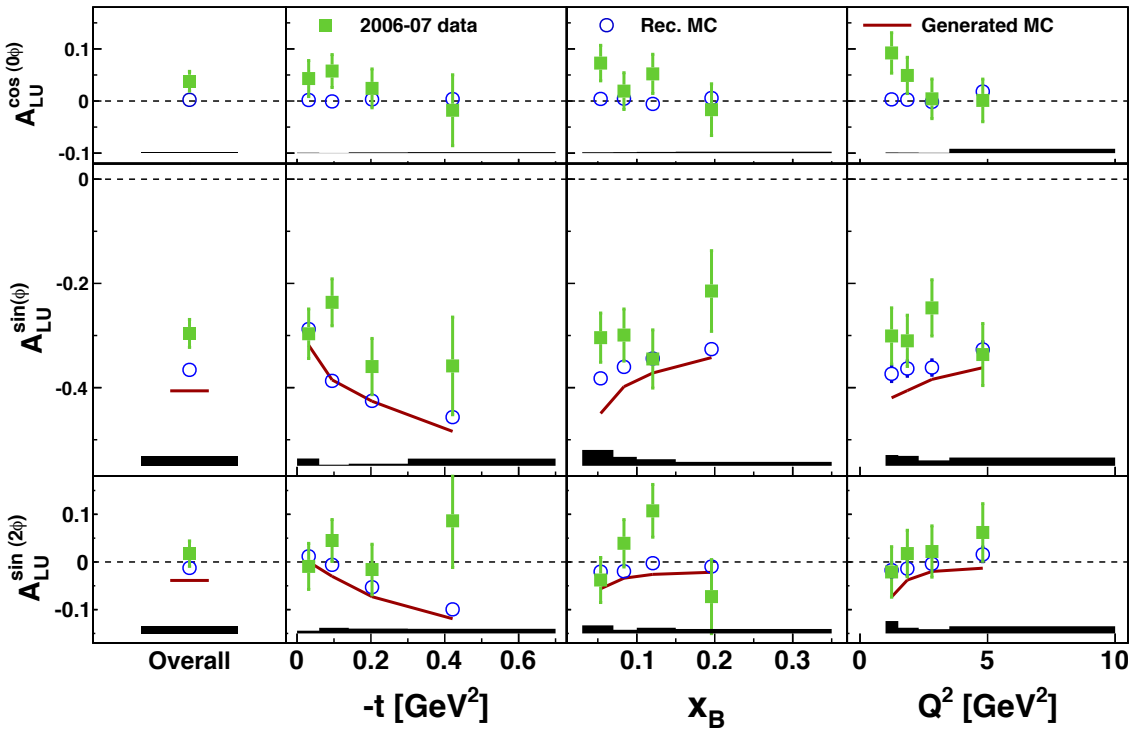

Figure 5.3: The overall "3–in–1" contribution to the systematic uncertainty of the beam-helicity asymmetry amplitudes. In each kinematic bin, the difference between the calculated curves (red curve) and the Monte-Carlo asymmetry amplitudes reconstructed in the HERMES acceptance (blue circles) from each model is taken as systematic uncertainty. Here the average of all the five models is plotted. Also shown are the amplitudes reconstructed from the pure elastic data sample (green squares).

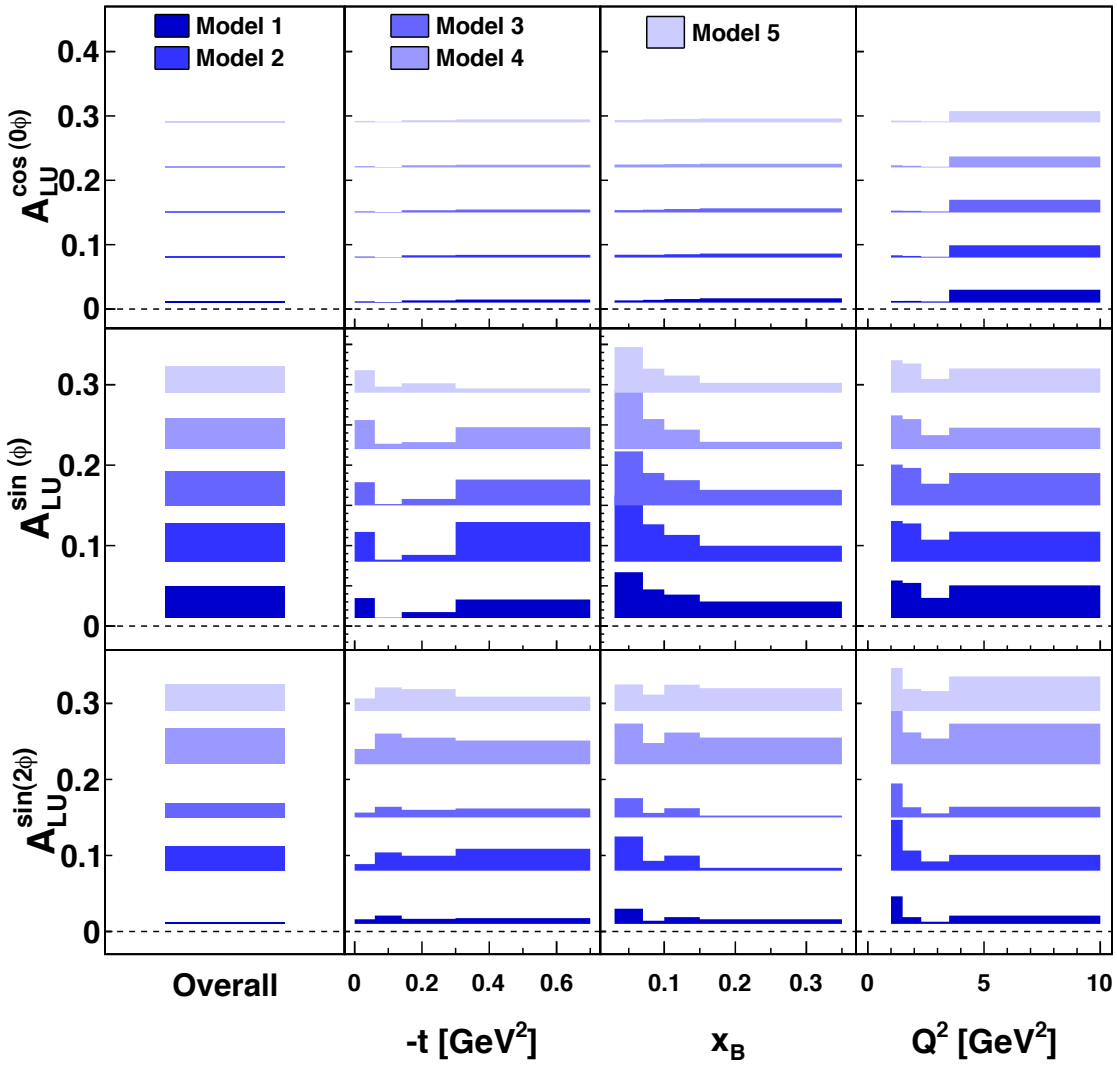

Figure 5.4: Comparison of the 3–in–1 systematic uncertainties arising from each of the VGG models for the amplitudes of the Beam Helicity Asymmetry.

5.5 Total systematic uncertainties

In summary there are a number of possible sources of systematic uncertainties. The sources that result in a systematic effect are mostly from spectrometer acceptance and alignment, smearing and finite bin width. There is also a small systematic uncertainty included from background effects from SIDIS.

The total systematic uncertainty affecting each extracted amplitude is determined in each kinematic bin as

$$\delta_{\text{syst}} = \sqrt{\delta_{\text{bg}}^2 + \delta_{\text{3in1}}^2}. \tag{5.8}$$

The contributions are shown below in Table 5.3.

	A	$\delta_{\text{stat.}}$	$\delta_{\text{total,sys}}$	$\delta_{\text{3in1, sys.}}$	$\delta_{\text{SIDIS,sys.}}$
$\sin\phi$	-0.296	0.028	0.018	0.018	< 0.001
$\sin(2\phi)$	0.013	0.027	0.015	0.015	< 0.001

Table 5.3: Overview of the contributions to the systematic uncertainty of the pure elastic beam–helicity asymmetry integrated over $-t$, x_B, and Q^2. The individual systematic uncertainties were added in quadrature to obtain the total systematic uncertainty δ_{sys}.

Chapter 6

Results

This chapter presents the final results of the extraction of the asymmetry amplitudes from the 2006–2007 data. The results are compared to the previous analysis of DVCS on an unpolarised hydrogen target that did not use information from the Recoil Detector, but with an expanded coverage compared to this analysis. They are also compared to a sample with an identical phase space and to model calculations.

6.1 Comparison with HERMES results

The final result of the asymmetry amplitudes extracted from 2006-2007 data with a fully operational Recoil Detector and an unpolarised hydrogen target are shown in Figure 6.1 (red squares). They are shown integrated over all kinematics and projected against $-t$, x_B and Q^2. Also shown in this figure are amplitudes extracted from the complete 2006 to 2007 data set, without using the Recoil Detector information [9] (green circles). This data set is taken with a different acceptance to the recoil result in this thesis, because the recoiling proton is not required to be within the acceptance of the Recoil Detector. The third set of asymmetries (blue triangles) extracted are taken from the same set of data with a fully operational recoil detector. This data selection without the Recoil Detector and requiring the reconstructed proton to be within the Recoil Detector acceptance is referred to as the "reference" sample. The error bars for all three sets are the statistical uncertainties, and the error bands are the systematic uncertainties. For the projections in $-t$, x_B and Q^2,

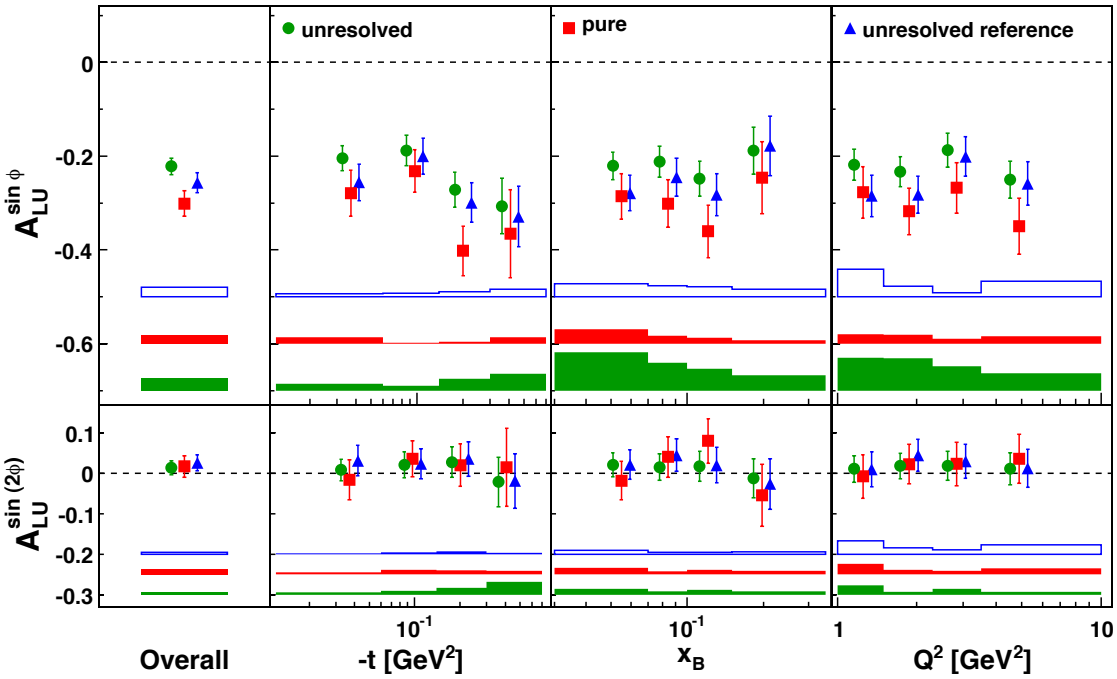

Figure 6.1: The $\sin(n\phi)$ asymmetry amplitudes of the DVCS single-charge beam helicity asymmetry of the pure elastic (red squares) and reference (blue triangles) samples extracted from 2006 and 2007 hydrogen data taken with a positron beam and fully operational Recoil Detector. Also the full 2006-2007 data set from Ref [9]. The error bars denote the statistical uncertainties and the error bands denote the systematic uncertainties.

the same binning was used as in Ref [6].

First considering the analysis of this thesis using the Recoil Detector. The leading twist $\sin\phi$ amplitude shows no dependence on x_B and Q^2,and there is an indication of a non–flat dependence on $-t$. The overall value of the higher twist $\sin(2\phi)$ amplitude is compatible with zero within statistical uncertainties. No conclusion about the kinematic dependence of this term can be drawn from these results.

The single beam–helicity asymmetry does not allow the disentanglement of BH/DVCS interference and DVCS terms as is done in [6, 9]. The amplitudes extracted without using the Recoil Detector were also extracted simultaneously with the beam charge asymmetry, thus allowing the disentanglement of the BH/DVCS interference and DVCS terms. It has been shown by HERMES that at leading twist the $A_{DVCS}^{\sin\phi}$ is consistent with zero [7, 9]. It is thus reasonable to compare the extraction of $A_{\sin\phi}^{I}$ with the recoil BHA result. However these two event samples have a

different acceptance, therefore a reference sample was used, and asymmetry amplitudes extracted in a similar manner. When the reference sample is compared to the traditional sample, the magnitude is slightly larger, but they still agree within the uncertainties. Comparing the recoil results to these two, we see that the amplitude is slightly larger overall, especially in the last two $-t$ bins where the fraction of background from associated DVCS is higher. The $\sin(2\phi)$ amplitudes for all data sets agree with zero. Because the $\sin(\phi)$ amplitude is not significantly larger for the recoil sample, this indicates that the associated DVCS BHA is small in magnitude.

Figure ??fig:fractions) shows the process fractions estimated from Monte Carlo studies for each data sample. The elastic fraction refers to the DVCS signal this work was looking for. This shows that the final data sample using the Recoil Detector is very pure and background processes are negligible.

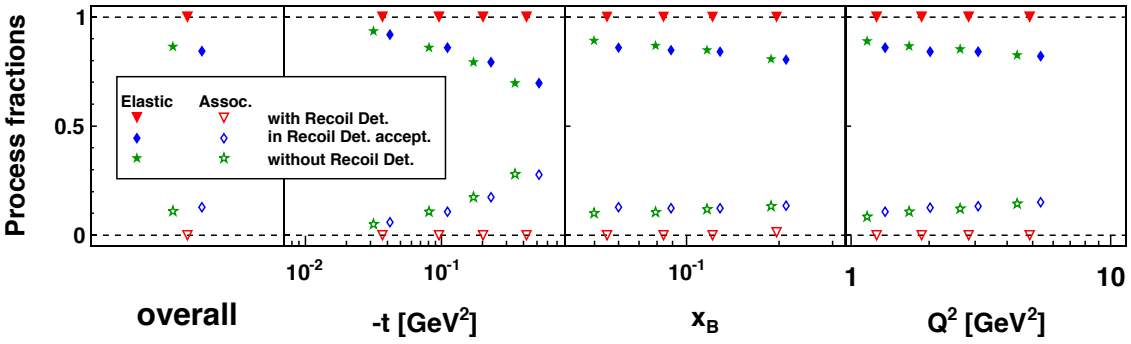

Figure 6.2: The process fractions estimated from Monte Carlo studies. The elastic fraction refers to the wanted DVCS signal, and Assoc. refers to estimated background contribution from associated DVCS.

6.2 Comparison with Model Calculations

Figure 6.3 shows the asymmetry amplitudes compared to model calculations, which are evaluated at the average value of each kinematic bin in which the asymmetry amplitudes are extracted.

The most well–known model, labelled "VGG Regge", from the GPD model described in Ref [29], and calculated using Ref [81]. This model has a number of variants. Here, a Regge–inspired ansatz for the t dependence is used. The ξ dependence is controlled by the b parameter, where b_{val} (b_{sea}) is a free parameter for

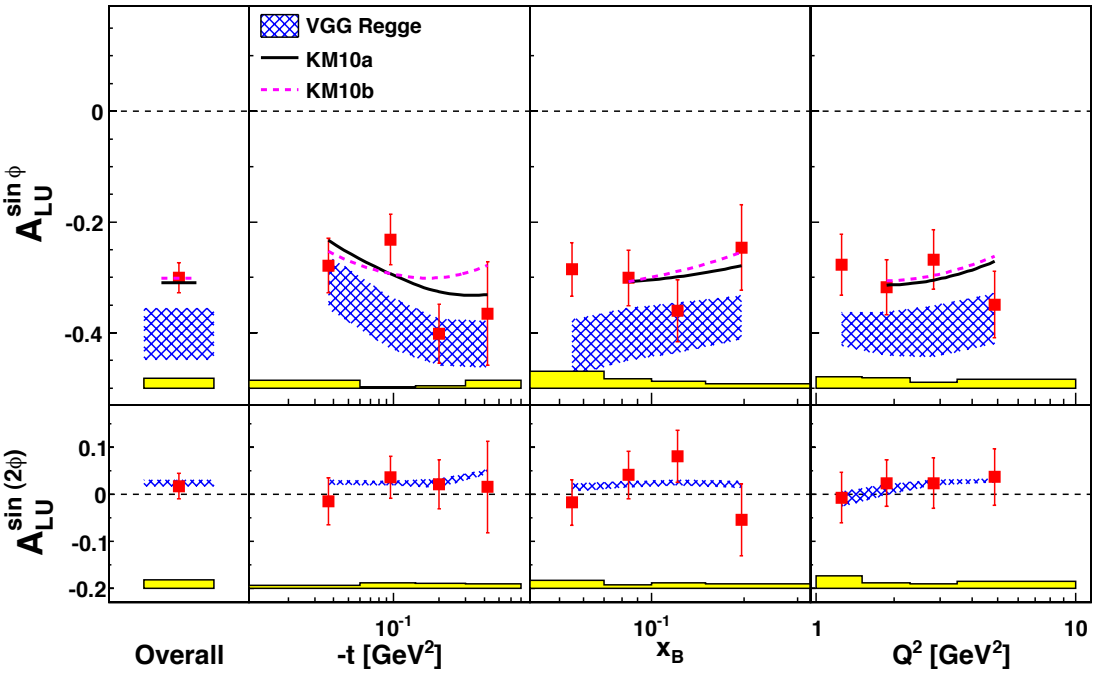

Figure 6.3: shows the recoil beam spin asymmetry result, with the error bars showing the statistical uncertainty and the error bands is the systematic uncertainty KM model and VGG curves.

the valence (sea) quarks. The broad width of the bands is due to the variation of b parameters between one and infinity. In general, the model band is larger in magnitude than the asymmetry amplitudes, where the upper part of the model bands that are closer to the extracted amplitudes, correspond to $b_{sea} = \infty$. The case where $b_{sea} = \infty$ corresponds to ξ independent GPDs.

The curves labelled "KM10" in Figure 6.3 show the results from model calculations [82] described in Ref [32]. This model includes information from previous measurements at HERMES, Jefferson Laboratory, and the collider experiments at HERA. It is a dual representation of GPDs, with very weak entangled skewness and t dependencies. The t dependence is approximated from a physically motivated Regge dependence. The solid curves exclude data from experiments at Hall A at Jefferson Laboratory [83, 84], and the dashed curves include this data. The magnitude of the predicted curves agrees well with the extracted amplitude.

The extracted asymmetry amplitudes are in better agreement with the KM models. The disagreement between extracted asymmetry amplitudes and the VGG

model [7] used to attributed to the unknown BHA of the Associated process. This result shows that within the uncertainties that the associated amplitude is likely to be small, analysis to extract the associated BHA is currently under way using at HERMES using the Recoil Detector.

6.3 Comparison with CLAS Measurements

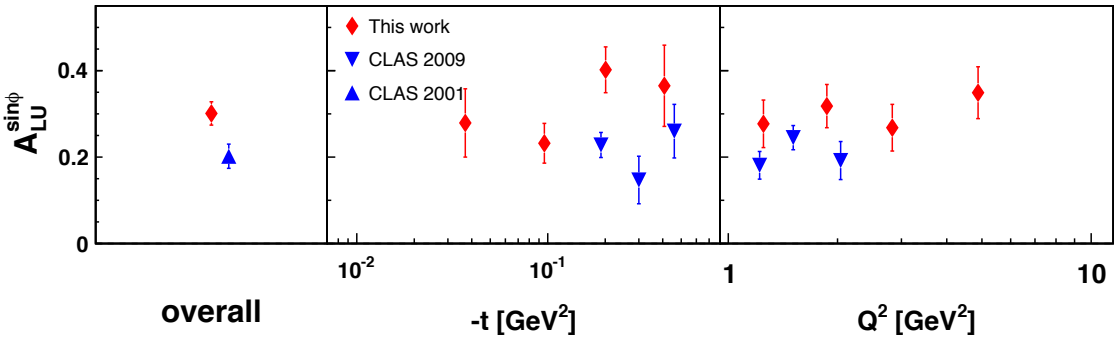

Figure 6.4: Comparison of the $\sin(\phi)$ amplitude integrated overall kinematics and versus $-t$ and Q^2 of results from this work and Jefferson Laboratory. This work is shown as a red diamond, CLAS 2009 [85] as an upside down triangle and CLAS 2001 from Ref [84] is a blue triangle . The results from CLAS were taken with a beam of opposite charge, therefore the amplitude is positive rather than negative.

The CLAS experiment has also published results of a Beam Helicity Asymmetry [84, 85]. The first measurement from CLAS [85] was extracted from data taken in 1999 using a 4.25 GeV longitudinaly polarised electron beam from a liquid hydrogen target. The second measurement [84] was extracted from data taken in 2000 with a 4.8 GeV longitudinally polarise electron beam incident off a liquid hydrogen target. The results were extracted using a least–squares fit fo the form $\mathcal{A}_{\rm LU}(\phi) = \alpha \sin\phi + \beta \sin(2\phi)$, where α and β are analogous to $A_{\rm UL}^{\sin\phi}$ and $A_{\rm UL}^{\sin(2\phi)}$ respectively.

The integrated values, $-t$ and Q^2 dependencies of the $A_{\rm UL}^{\sin\phi}$ amplitudes from HERMES and CLAS are compared in Figure 6.4. The amplitudes from CLAS are smaller in magnitude integrated overall kinematics than the result from this work. The results from CLAS are at slightly lower Q^2 and higher t, this will account for some of differences observed between the extracted amplitudes. The results from CLAS have a improved statistical accuracy due to the increased luminosity at CLAS.

6.4 Table of Results

The beam helicity amplitudes extracted for this thesis and the average kinematics for each kinematic bin plotted are shown in the table overleaf.

Kinematc Bin	$< -t >$ [GeV^2]	$< x_{\mathrm{B}} >$	$< Q^2 >$ [GeV^2]	$A_{\mathrm{LU}}^{\sin\phi} \pm \delta_{stat.} \pm \delta_{syst.}$	$A_{\mathrm{LU}}^{\sin 2\phi} \pm \delta_{stat.} \pm \delta_{syst.}$
Overall	0.132	0.101	2.612	-0.296 ± 0.027 ± 0.017	0. 017 ± 0.027 ± 0.015
$0.00 \leqslant -t \leqslant 0.06$	0.037	0.084	2.114	-0.297 ± 0.048 ± 0.014	-0.009 ± 0.048 ± 0.006
$0.06 < -t \leqslant 0.14$	0.095	0.099	2.482	-0.236 ± 0.04 5 ± 0.002	0.045 ± 0.044 ± 0.012
$0.14 < -t \leqslant 0.30$	0.200	0.114	2.971	-0.360 ± 0.05 3 ± 0.004	-0.016 ± 0.053 ± 0.010
$0.30 < -t \leqslant 0.70$	0.407	0.129	3.815	-0.358 ± 0.0 94 ± 0.014	0.086 ± 0.098 ± 0.010
$0.03 \leqslant x_{\mathrm{B}} \leqslant 0.07$	0.115	0.055	1.467	-0.304 ± 0.048 ± 0.030	-0.038 ± 0.047 ± 0.017
$0.07 < x_{\mathrm{B}} \leqslant 0.10$	0.111	0.084	2.145	-0.299 ± 0.050 ± 0.017	0.039 ± 0.050 ± 0.008
$0.10 < x_{\mathrm{B}} \leqslant 0.15$	0.134	0.121	3.116	-0.345 ± 0.056 ± 0.013	0.107 ± 0.055 ± 0.012
$0.15 < x_{\mathrm{B}} \leqslant 0.35$	0.200	0.197	5.035	-0.21 4 ± 0.077 ± 0.008	-0.073 ± 0.078 ± 0.009
$1.00 \leqslant Q^2 \leqslant 1.50$	0.100	0.058	1.250	-0.301 ± 0.054 ± 0.021	-0.021 ± 0.053 ± 0.026
$1.50 < Q^2 \leqslant 2.30$	0.113	0.080	1.869	-0.310 ± 0 .049 ± 0.019	0.017 ± 0.048 ± 0.011
$2.30 < Q^2 \leqslant 3.50$	0.133	0.109	2.830	-0.247 ± 0.054 ± 0.010	0.022 ± 0.054 ± 0.009
$3.50 < Q^2 \leqslant 10.0$	0.191	0.170	4.870	-0.337 ± 0.060 ± 0.016	0.062 ± 0.060 ± 0.015

Table 6.1: Results of the extraction of $A_{\mathrm{LU}}^{\sin(n\phi)}$ asymmetry amplitude with statistical and systematic uncertainties and average kinematics from unpolarised hydrogen taken during the 2006-2007 experimental data taking period using the Recoil Detector at HERMES for each $-t$, x_{B} and Q^2 bin. An additional 3.4 % scale uncertainty is present in the amplitudes due to the precision of the beam polarisation measurement.

6.5 Final BHA using the HERMES Recoil Detector

This work was an intermediate step towards a final BHA published by the collaboration in [86]. The published work used a more up to date data production not available to the author of this thesis at the time of analysis therefore the final asymmetry amplitudes extracted in this work differ from the published result. This work contributed to the calculation of the systematic uncertainties in the preliminary result [87], the work towards the cross check for this preliminary result and corresponding systematic studies.

The published result, [86], as mentioned above uses the most up to date data productions using the final detector calibrations for H ERMES and included improvements to the data selection methods to ensure purity. The systematic uncertainties also were calculated using only two models based on the VGG models rather than the 5 used in this thesis.

Chapter 7

Summary and Outlook

This thesis presented the analysis of Deeply Virtual Compton Scattering (DVCS) using the HERMES Recoil Detector to detect a truly exclusive data sample. The Beam Helicity Asymmetry (BHA) amplitudes were extracted from the hard exclusive leptoproduction of real photons off an unpolarised hydrogen target. The extracted asymmetry amplitudes results have been compared to previous results from HERMES.

Prior to the installation of the Recoil Detector, the recoiling proton was not detected and thus all DVCS results contained an estimated large contamination from associated DVCS. By comparing the results presented in this thesis to previous results it is possible to ascertain the effect of this contamination on the extracted asymmetry amplitudes. A slight increase was observed in the magnitude of the BHA amplitudes for the purely exclusive sample. However within the statistical uncertainties of the recoil sample they are reasonable agreement. Further work will be undertaken by HERMES to determine if possible a first extraction of the BHA for the associated DVCS.

The extracted asymmetry amplitudes can be used to access Compton Form Factor $\mathcal{H}$, which is related to the corresponding Generalised Parton Distribution (GPDs). GPDs can be used to describe the structure of the nucleon and provide experimental access to the total angular momentum of quarks.

The data were taken using a $27.6\,GeV$ longitudinally polarised positron beam incident on an unpolarised hydrogen gas target at HERMES using the Recoil Detector.

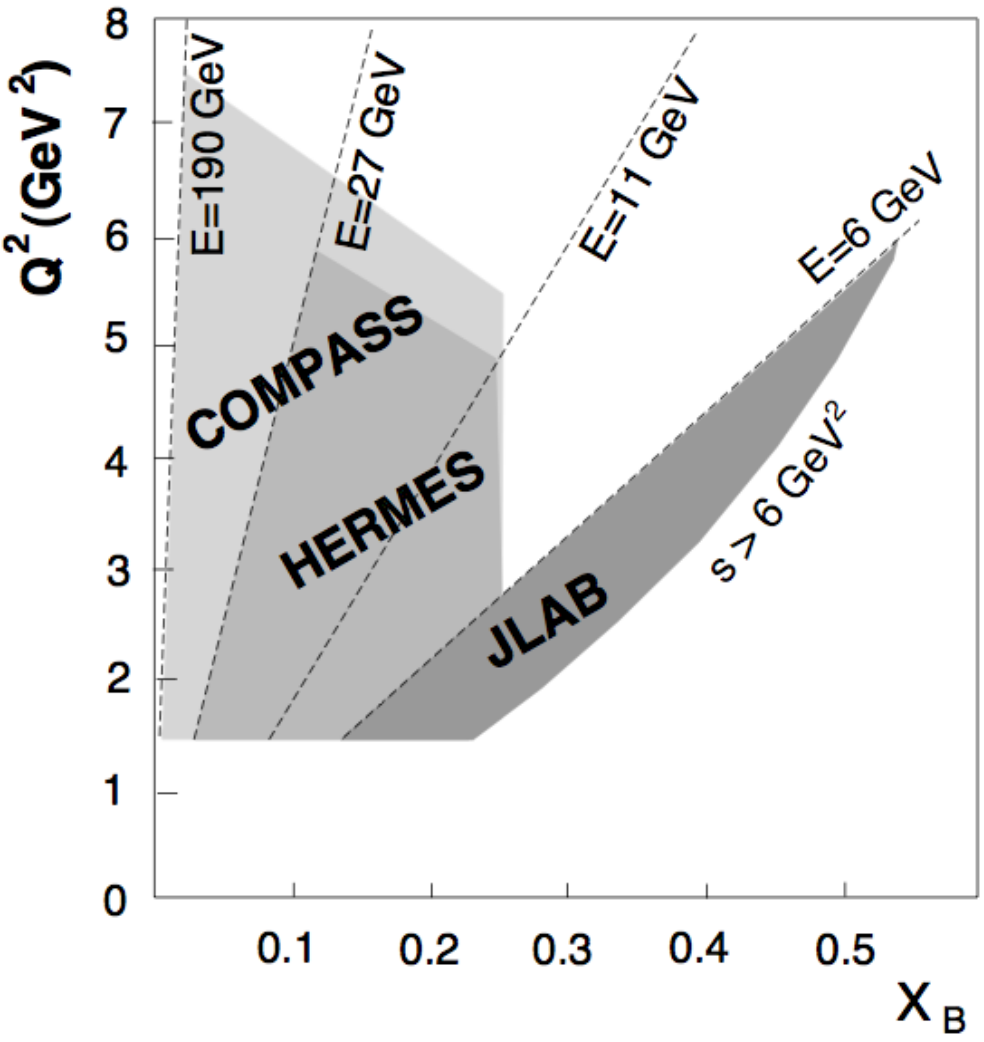

Figure 7.1: Kinematic coverage of current and planned DVCS experiments [88].

The asymmetry results were extracted over the entire kinematic range, as well as a function of $-t$, x_B and Q^2. The leading amplitude $A_{LU}^{\sin\phi}$ has an overall value of $0.301 \pm 0.027 \pm 0.018$. No strong kinematic dependence was observed, however there is a hint of dependence on $-t$, but within the statistical uncertainties no strong conclusion can be drawn. The dependencies are in agreement with the model curves, with all models showing an increase with increasing $-t$. The "VGG" model is in general larger in amplitude, which previously was attributed to the presence of associated background. The "KM" models agree well with the extracted asymmetry amplitudes within the uncertainties of the measurement.

First attempts at extracting CFF $\mathcal{H}$ have already been attempted using HERMES

[89] and CLAS [41] DVCS results discussed in Section 2.10.

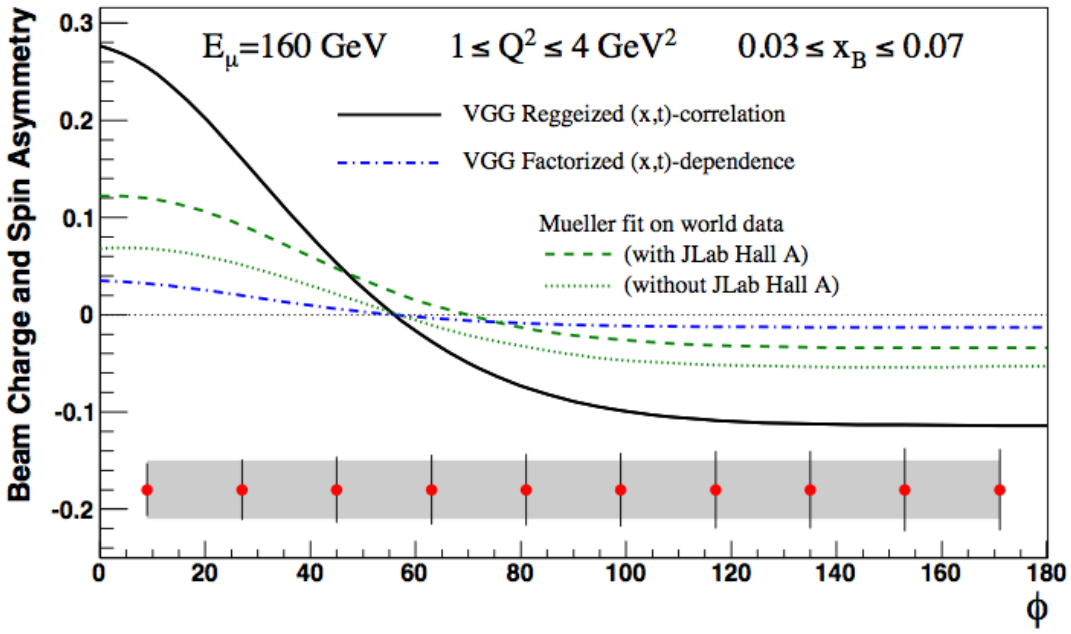

Figure 7.2: Prediction of Compass result

In the future other experiments will continue to measure DVCS at different kinematics, including COMPASS at CERN [88] and Halls A and B at Jefferson Lab. The different kinematic ranges are shown in Figure 7.1, which shows the current range explored by HERMES and Jefferson Laboratory.

In 2009, a test run was undertaken at COMPASS to ascertain the feasibility of studying DVCS. These studies showed that COMPASS was able to measure DVCS. Since then the proposal to run DVCS experiments at COMPASS was accepted and will run hopefully in 2013. A prediction by [32], shown in Figure 7.2 shows the preiction of the beam spin charge asymmetry, which is sensitive to GPD H.

After the upgrade of CEBAF at Jefferson Laboratory to $12GeV$ in the coming years, the proposed measurements from Jefferson Laboratory will be high precision measurements: cross section measurements from HALL A and beam and target spin asymmetries from CLAS. These measurements can then be used in order to extract GPD H and $\tilde{H}$.

Appendix A

Target Gas Contamination

When calibrating the Silicon Strip Detector (SSD), heavy particles were observed in the plots of the energy deposition of the inner layer versus the energy deposition of the outer layer of the SSD for all quadrants of the detector. These additional "bands" correspond to deuterons, tritons and helium nuclei as shown by the calculated bands in Figure A.1 below.

The observation of a heavy gas within the target cell was thought to have originated from a leak in the target cell or the gas feed. The aim of these studies was to attempt to quantify the level of contamination, and whether the level of contamination was constant during the data taking period with the Recoil Detector.

This section will detail the studies undertaken by the author in an attempt to quantify and understand the possible heavy target gas contamination. All studies undertaken by the author and others at HERMES are detailed in Ref. [90].

A.1 Studies using the Silicon Strip Detector

The time dependence of the contamination was investigated initially to determine if there were any fluctuations in the contamination which may have originated to hardware problems over the running period. The data for each year was separated into runs with low and high density hydrogen and deuterium target gases to compare the contamination levels between the target density and target gases. For high density hydrogen runs one would expect that a lower contamination would be observed

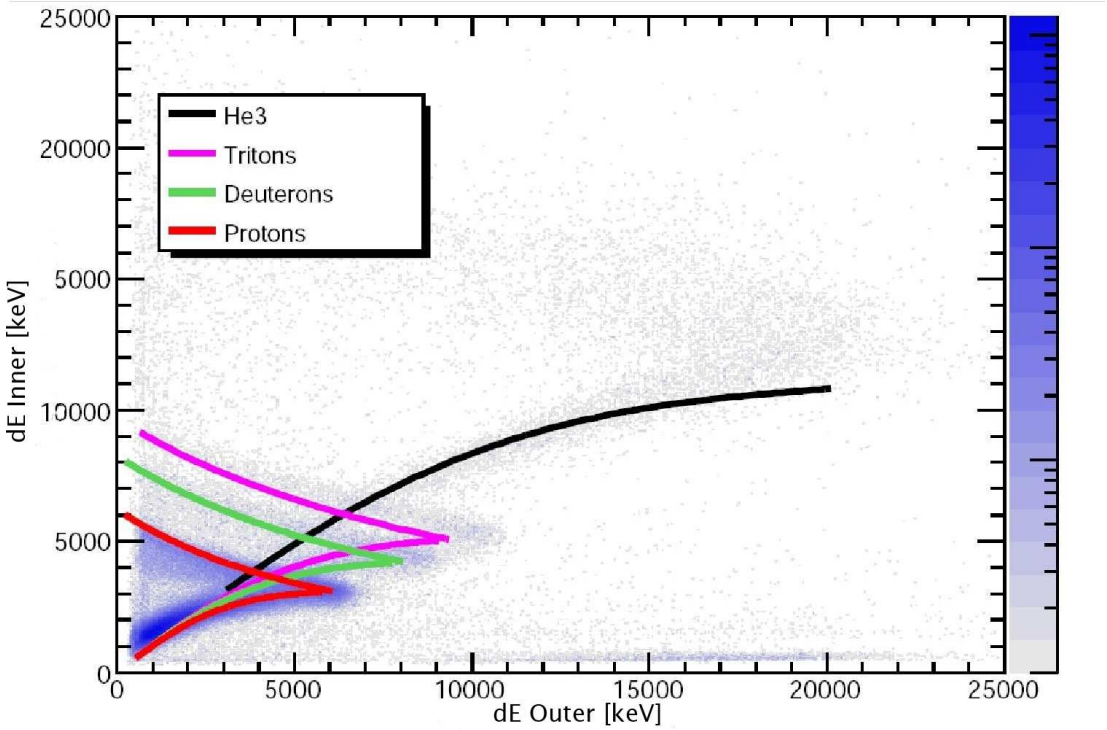

Figure A.1: Energy deposition in the inner p-side of the SSD (dE Inner) versus energy deposition in the outer p-side of the SSD (dE Outer). The coloured bands show the calculated bands for various particle types [**?**].

if the contamination resulted from a leak in the target cell or the gas feed pipe, but if the contamination originated in the gas itself then the contamination level would be consistent. The number of runs was then divided into bins of 1000 runs, such that there was enough statistics for energy deposition histograms.

In order to compare the data years and target types, deep inelastic scattering (DIS) events were selected. Histograms of the energy deposition in the inner SSD versus the energy deposition in the outer SSD were then plotted for each bin of 1000 runs. Once the histograms had been produced, a cut was made to select the helium nuclei, illustrated in Figure A.2. This cut does not isolate all of the helium particles, as helium nuclei with high momentum punch through both layers, thus the corresponding section of the band in the histogram overlaps with the proton band. The number of events within this the cut was then normalised to the total number of DIS events in the data sample.

The time dependence was investigated for all hydrogen (low and high density)

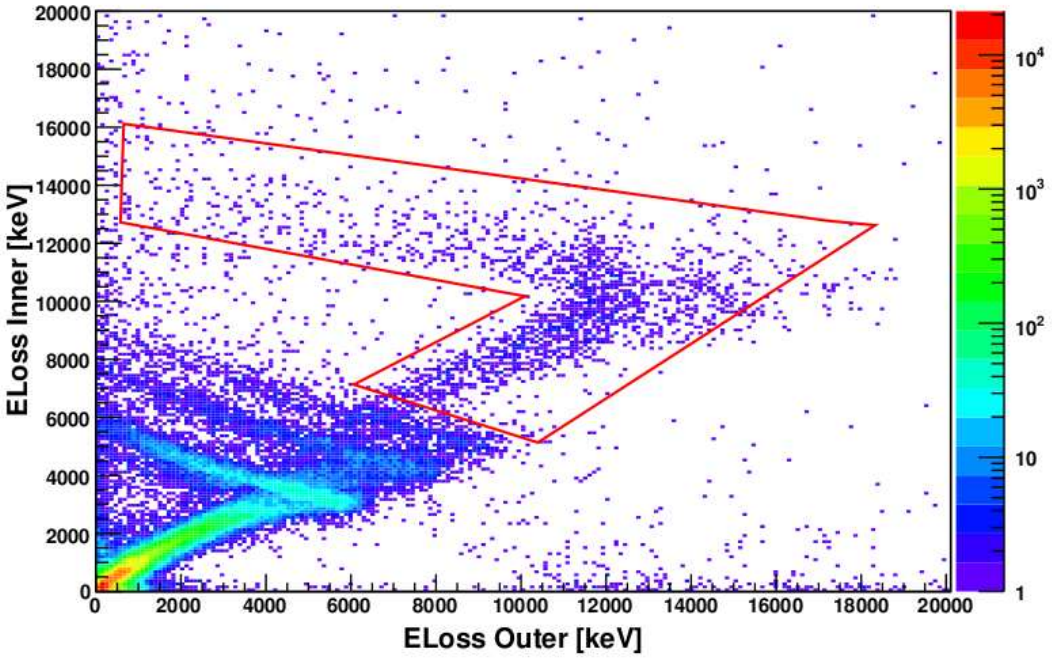

Figure A.2: A 2-dimensional histogram of the energy deposition in the inner SSD versus the energy deposition in the outer SSD. The 2–dimensional cuts used to select the heavy particles are also shown

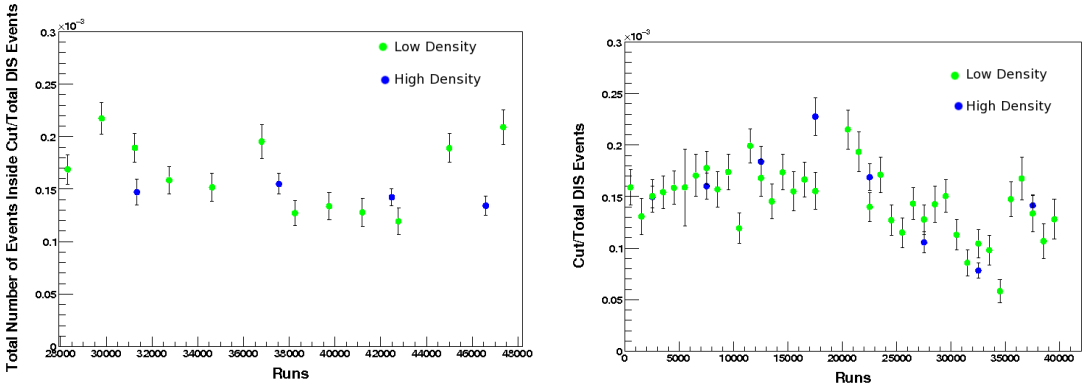

(a) Hydrogen 2006

(b) Hydrogen 2007

Figure A.3: Plots of the number of helium nuclei normalised to the number of DIS events versus run number for 2006 and 2007 hydrogen data. They show that the level of contamination for both high and low density target gases was consistent and fairly constant, with some fluctuations, over the data taking period.

and deuterium runs separately for 2006 and 2007 by plotting the normalised number of events within each cut versus run number.

In Figure A.3 and Figure A.4 the time dependence of the contamination is shown.

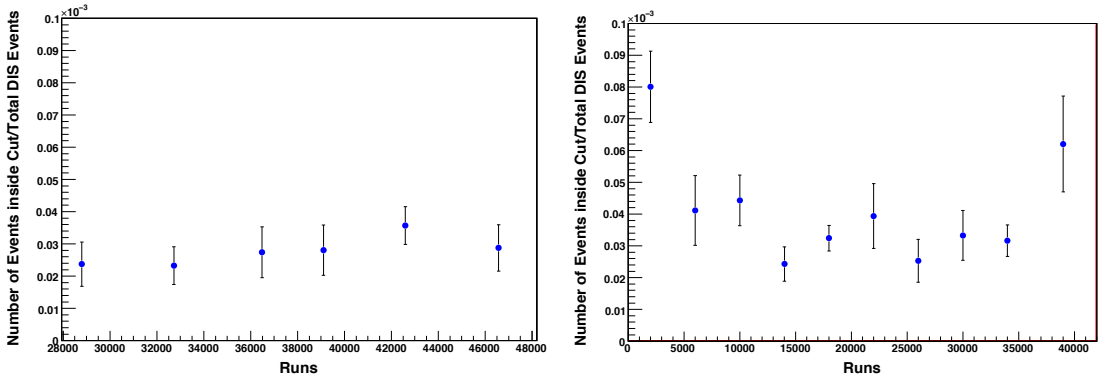

(a) Deuterium 2006 (b) Deuterium 2007

Figure A.4: Plots of the number of helium nuclei normalised to the number of DIS events versus the run number for 2006 and 2007 deuterium data. These show that the level of contamination was lower than for the hydrogen target. The level of contamination was constant apart from the beginning and the end of 2007. The fluctuations were smaller for deuterium data than the hydrogen data.

From these one can conclude that contamination was present in all data taken. For the hydrogen data the contamination level was similar for both the high and low density runs, and fluctuations were small. The level of contamination was lower for the deuterium data, and was relatively constant level during 2006, which suggest that the contamination was only present in the hydrogen target gas. The contamination level for 2007 deuterium data was consistent with 2006 but there was a larger fluctuation at the beginning and end of 2007. The fluctuations in the contamination level were larger for the hydrogen data.

From Figure A.3(b) one observes that the contamination level during 2007 was similar for both low and high density hydrogen. Looking at each fill (for each time the target cell was filled) would mean that the cause of the small observed fluctuations could be identified, however this method would not be appropriate as the number of statistics would not be sufficient as a fill was only a few runs. The level of contamination for the deuterium data was observed to be considerably less. The deuterium was sourced from a bottle and was considered to be pure, therefore the contamination could have resulted from remnants from the hydrogen or mislabelling of runs.

In order to determine whether the contamination was due to a leak in the target

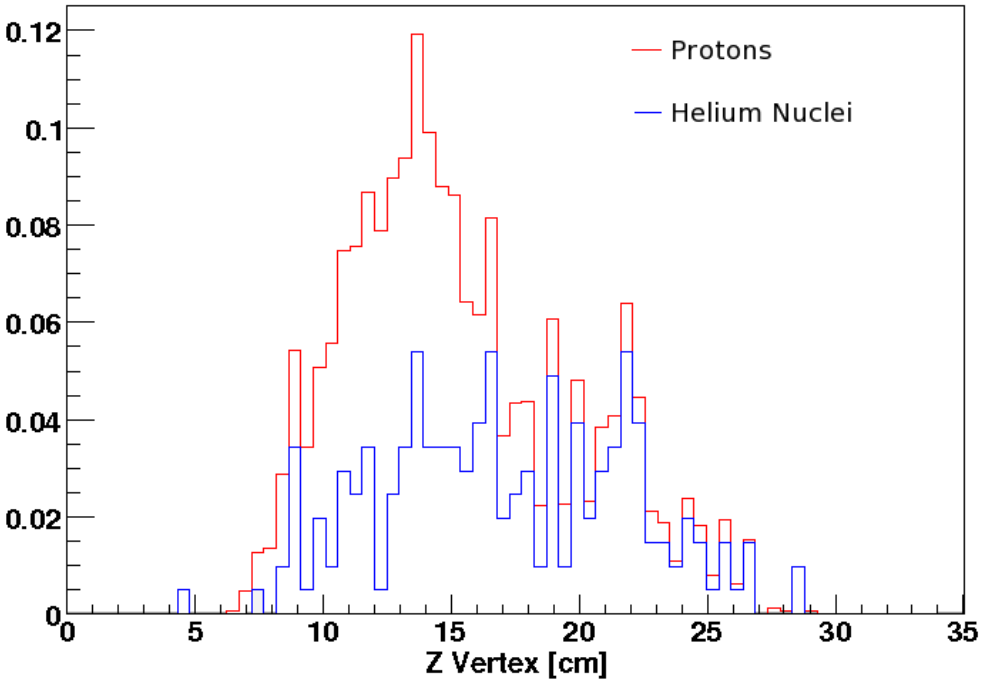

Figure A.5: The z–vertex distribution for protons and helium nuclei. The distributions are consistent which was expected.

cell itself or from the gas feed, the z–vertex distribution of the heavy particles was compared to that of the protons, as seen in Figure A.5. The distribution for both nuclei was similar. This suggests that the contamination resulted from the gas feed.

The study using data from the SSD showed that the time dependence of the contamination is relatively constant over the data taking period with some fluctuations. The level of heavy gas contamination is seen to be lower in the deuterium data. The z–vertex position of the heavy particles was observed to be consistent to the usual z–vertex distribution observed for DIS events, which means that there wasn't a leak in the target cell, but originated from the gas feed.

The conclusions which have been made from these studies is that the level of contamination is lower for the deuterium data. The level of contamination is relatively constant over 2006 and 2007 with some fluctuations. From the z-vertex distribution of the heavier particles, which is consistent with that of the lighter particles.

Appendix B

Input to the VGG code

One of the models that the extracted asymmetries are compared to is calculated from computer code [81] implementation of the VGG model described in Section 2.5.1 and Ref [29]. The model has a Regge inspired t–dependence, and the b–parameter which controls the ξ dependence. The b–parameter was varied between 1 and 9 in the computer code . The Wandzura–Wilczek (WW) approximation was chosen to include a twist–3 contributions.

- **4:** 2-body double-polarised cross-sections for DVCS using a polarised lepton beam and a polarised target
- **3:** Bethe–Heitler and DVCS contribution
- **1:** Proton target
- **36:** GPD model ξ–dependence parameterisation with MRST02 NNLO distribution
- **2:** Evolution with scale Q^2 rather than fixed $Q^2 = 2GeV^2$
- **1 and 9:** Valance quark contribution $b_{valence}$
- **1 and 9:** Sea quark contribution b_{sea}
- **2:** Regge-inspired ansatz for t–dependence with $\alpha' = 0.8$
- **2:** Exclude D term as it only contributes to the real part of CFF $\mathcal{H}$

- **2:** Evaluate GPD E using the Double-Distribution (DD) and D term
- **2:** Give the model for the DD part of GPD E considering valence quark and VM contributions
- **0.2:** Value of J_u from lattice QCD
- **0.1:** Value of J_d from lattice QCD
- **1:** Evaluate the $/pi^0$ pole contribution, i.e GPD $\tilde{E}$
- **2:** Include twist–3 corrections in the WW-approximation (i.e. correlations between antiquarks, gluons and quarks in the nucleon)
- **1:** Include GPD $\tilde{H}$
- **3:** Proton polarised along the x-axis
- **2:** Positron beam
- **27.57:** Beam energy in GeV
- **3:** Cross-sections extracted as a function of ϕ
- $< Q^2 >$ Average Q^2 from data
- $< x_B >$ Average x_B from data
- $< Q_0^2 >= 0$ Average Q_0^2 from data - DDVCS only
- $< -t >$ Average $-t$ from data
- **0:** ϕ_{start} in degrees
- **10:** ϕ_{step} in degrees
- **180:** ϕ_{end} in degrees

Appendix C

Abbreviations

BH Bethe–Heiter

BHA Beam Helicity Asymmetry

CFF Compton Form Factor

DIS Deep Inelastic Scattering

DVCS Deeply Virtual Compton Scattering

EML Extended Maximum Likelihood

GPDs Generalised Parton Distributions

HERA Hadron–Electron Ring Accelerator

HERMES Hera Measurement of Spin

HTC Hermes Tracking Code

HRC Hermes Reconstruction Code

KM Kumericki Mueller model

LPOL Longitudinal Polarimeter

PD Photon Detector

PDF Parton Distribution Functions

PID Particle Identification

RD Recoil Detector

rdPID Recoil Detector Particle Identification

SIDIS Semi Inclusive DIS

SSD Silicon Strip Detector

SFT Scintillating Fibre Detector

SPE Single Photon Event

TPOL Transverse Polarimeter

VGG Vanderhaegen, Guichon and Guidal

XTC External Tracking Code

Bibliography

[1] J. Ashman *et al.*, "An investigation of the spin structure of the proton in deep inelastic scattering of polarized muons on polarized protons," *Nucl. Phys.*, vol. B328, p. 1, 1989.

[2] A. Airapetian *et al.*, "Quark helicity distributions in the nucleon for up, down, and strange quarks from semi–inclusive deep–inelastic scattering," *Phys. Rev.*, vol. D71, p. 012003, 2005.

[3] A. Airapetian *et al.*, "Precise determination of the spin structure function g(1) of the proton, deuteron and neutron," *Phys. Rev.*, vol. D75, p. 012007, 2007.

[4] X. Ji, "Gauge-Invariant Decomposition of Nucleon Spin and Its Spin-Off," *Phys.Rev.Lett.*, vol. 78, pp. 610–613, 1997.

[5] M. Diehl, "Generalized parton distributions," *Phys. Rept.*, vol. 388, pp. 41–277, 2003.

[6] A. Airapetian *et al.*, "Measurement of Azimuthal Asymmetries With Respect To Both Beam Charge and Transverse Target Polarization in Exclusive Electroproduction of Real Photons," *JHEP*, vol. 06, p. 066, 2008.

[7] A. Airapetian *et al.*, "Separation of contributions from deeply virtual Compton scattering and its interference with the Bethe–Heitler process in measurements on a hydrogen target," *JHEP*, vol. 11, p. 083, 2009.

[8] The HERMES Collaboration, A. Airapetian et al., "Exclusive leptoproduction of real photons on a longitudinally polarised hydrogen target," *JHEP 06*, vol. 019, 2010.

[9] A. Airapetian *et al.*, "Beam-helicity and beam-charge asymmetries associated with deeply virtual Compton scattering on the unpolarised proton," *JHEP*, vol. 1207, p. 032, 2012.

[10] R. Hofstadter, "Electron scattering and nuclear structure," *Rev. Mod. Phys.*, vol. 28, pp. 214–254, Jul 1956.

[11] A. V. Radyushkin, "Scaling Limit of Deeply Virtual Compton Scattering," *Phys.Lett. B*, vol. 380, pp. 417–425, 1996.

[12] J. C. Collins and A. Freund, "Proof of factorization for deeply virtual Compton scattering in QCD," *Phys. Rev.*, vol. D59, p. 074009, 1999.

[13] X.-D. Ji and J. Osborne, "One-loop corrections and all order factorization in deeply virtual Compton scattering," *Phys. Rev.*, vol. D58, p. 094018, 1998.

[14] G. Altarelli and G. Parisi, "Asymptotic Freedom in Parton Language," *Nucl.Phys.*, vol. B126, p. 298, 1977.

[15] Dokshitzer, Yuri L., "Calculation of the Structure Functions for Deep Inelastic Scattering and e+ e- Annihilation by Perturbation Theory in Quantum Chromodynamics," *Sov. Phys. JETP*, vol. 46, pp. 641–653, 1977. [Zh.Eksp.Teor.Fiz.73:1216-1240,1977].

[16] Gribov, V.N. and Lipatov, L.N., "Deep inelastic e p scattering in perturbation theory," *Sov.J.Nucl.Phys.*, vol. 15, pp. 438–450, 1972.

[17] Lipatov, L.N., "The parton model and perturbation theory," *Sov.J.Nucl.Phys.*, vol. 20, pp. 94–102, 1975.

[18] R. L. Jaffe, "Spin, twist and hadron structure in deep inelastic processes," 1996.

[19] Efremov, A.V. and Radyushkin, A.V., "Field Theoretic Treatment of High Momentum Transfer Processes 1. Deep Inelastic Scattering," *Theor.Math.Phys.*, vol. 44, pp. 573–584, 1980.

[20] Lepage, G.Peter and Brodsky, Stanley J., "Exclusive Processes in Perturbative Quantum Chromodynamics," *Phys.Rev.*, vol. D22, p. 2157, 1980.

[21] D. Mueller, D. Robaschik, B. Geyer, F. M. Dittes, and J. Ho?ej?i, "Wave Functions, Evolution Equations and Evolution Kernels from Light-Ray Operators of QCD," *Fortsch.Phys.*, vol. 42, p. 101, 1994.

[22] A. V. Radyushkin, "Double distributions and evolution equations," *Phys.Rev. D*, vol. 59, p. 014030, 1999.

[23] X.-D. Ji, "Off forward parton distributions," *J.Phys.*, vol. G24, pp. 1181–1205, 1998.

[24] K. Goeke, M. V.Polyakov, and M. Vanderhaeghen, "Hard Exclusive Reactions and the Structure of Hadrons," *Prog. Part. Nucl. Phys.*, vol. 47, pp. 401–515, 2001.

[25] M. Guidal, "Recent experimental results on deep virtual Compton scattering and generalized parton distributions," *Nucl.Phys.Proc.Suppl.*, vol. 181-182, pp. 62–65, 2008.

[26] M. Burkardt, "Impact parameter dependent parton distributions and off forward parton distributions for zeta," *Phys.Rev.*, vol. D62, p. 071503, 2000.

[27] M. Diehl, T. Feldmann, R. Jakob, and P. Kroll, "Generalized parton distributions from nucleon form factor data," *EUR.PHYS.J.C*, vol. 39, p. 1, 2005.

[28] P. Kroll, "Generalized perton distributions: analysis and applications," 2004.

[29] M. Vanderhaeghen, P. A. M. Guichon, and M. Guidal, "Deeply virtual electroproduction of photons and mesons on the nucleon: Leading order amplitudes and power corrections," *Phys. Rev.*, vol. D60:094017, 1999.

[30] A. D. Martin, R. Roberts, W. Stirling, and R. Thorne, "Scheme dependence, leading order and higher twist studies of MRST partons," *Phys.Lett.*, vol. B443, pp. 301–307, 1998.

[31] P. Collins, "An Introduction to Regge Theory and High-Energy Physics," 1977.

[32] K. Kumericki and D.Mueller, "Deeply virtual Compton scattering at small x_B and the access to GPD H." arXiv:0904.0458.

[33] Goldstein, Gary R. and Hernandez, J. Osvaldo Gonzalez and Liuti, Simonetta, "Flexible parametrization of generalized parton distributions from deeply virtual compton scattering observables," *Phys. Rev. D*, vol. 84, p. 034007, Aug 2011.

[34] A. V. Belitsky, D. Muuller, and A. Kirchner, "Theory of deeply virtual Compton scattering on the nucleon," *Nucl.Phys. B*, vol. 629, pp. 323–392, 2002.

[35] A. Airapetian *et al.*, "Measurement of azimuthal asymmetries associated with deeply virtual Compton scattering on an unpolarized deuterium target," *Nucl. Phys.*, vol. B829, pp. 1–27, 2010.

[36] A. Airapetian *et al.*, "The Beam–Charge Azimuthal Asymmetry and Deeply Virtual Compton Scattering," *Phys. Rev.*, vol. D75, p. 011103, 2007.

[37] The HERMES Collaboration, "Measurement of double-spin asymmetries associated with deeply virtual Compton scattering on a transversely polarized hydrogen target," *Phys. Lett.*, vol. B704, pp. 15–23, 2011.

[38] D. Zeiler, *Deeply Virtual Compton Scattering off an Unpolarized Hydrogen Target at the HERMES Experiment*. PhD thesis, University Erlangen-Nuremberg, 2009.

[39] J. Burns, *Deeeply Virtual Compton Scattering off an Unpolarised Hydrogen Target*. PhD thesis, University of Glasgow, 2010.

[40] D. F. Mahon, *Deeply Virtual Compton Scattering off Longitudinally Polarised Protons at HERMES*. PhD thesis, University of Glasgow, 2010.

[41] H.Moutarde, "Extraction of the Compton form factor $\mathcal{H}$ from deeply virtual Compton scattering measurements at Jefferson Lab," *Phys. Rev.*, vol. D79, p. 094021, 2009.

[42] M. Guidal, "Constraints on the $\tilde{H}$ Generalized Parton Distribution from Deep Virtual Compton Scattering Measured at HERMES," *Phys.Lett.*, vol. B693, pp. 17–23, 2010.

[43] M. Guidal and H. Moutarde, "Generalized Parton Distributions from Deeply Virtual Compton Scattering at HERMES," *Eur.Phys.J.*, vol. A42, pp. 71–78, 2009.

[44] C. M. n. Camacho *et al.*, "Scaling tests of the cross section for deeply virtual compton scattering," *Phys. Rev. Lett.*, vol. 97, p. 262002, Dec 2006.

[45] M. Guidal, "Generalized parton distributions from deep virtual compton scattering at clas," 2010.

[46] The HERMES Collaboration, "The HERMES Recoil Detector Technical Design Report , HERMES Internal Report 02-003," 2002.

[47] A. Airapetian et al., "The HERMES Recoil Detector," *To Be Submitted*, 2013.

[48] A. A. Sokolov and I. M. Ternov, "On polarization and spin effects in the theory of synchrotron radiation," *Sov. Phys. Dokl.*, vol. 8, pp. 1203–1205, 1964.

[49] J. Buon and K. Steffen, "HERA variable-energy "mini" spin rotator and head-on ep collision scheme with choice of electron helicity," *Nucl. Instrum. Meth. A*, vol. 245, pp. 248–261, 1986.

[50] D. Barber *et al.*, "The HERA polarimeter and the first observation of electron spin polarization at HERA," *Nucl. Instrum. Meth. A.*, vol. 329, pp. 79–111, 1993.

[51] M. B. *et. al.*, "The Longitudinal Polarimeter at HERA," *Nucl. Instrum. Meth. A*, vol. 479, pp. 334–348, 2002.

[52] A.Nass et al., "The HERMES polarized atomic beam source," *Nucl. Instrum. Meth. A.*, vol. 505, pp. 633–644, 2003.

[53] Target Group, "Unpolarised gas feed system - (ugfs)," *Shift Crew - Operation Manual*, 2006.

[54] M. J. Murray, *DVCS at HERMES: The Recoil Detector & Transverse Target Spin Asymmetries*. PhD thesis, DESY, 2008.

[55] K. Ackerstaff *et al.*, "HERMES spectrometer," *Nucl. Instrum. Meth.*, vol. A417, pp. 230–265, 1998.

[56] M. Tytgat, "Particle identification with the HERMES RICH," *Nucl. Instrum. Meth. A.*, vol. 433, pp. 286–288, 1999.

[57] R. Kaiser, *Measurement of the spin structure of the neutron using polarised deep inelastic scattering.* PhD thesis, Simon Fraser University, 1997.

[58] R.Kaiser, "Particle identification at hermes, hermes internal report 97-025," 1997.

[59] H. Avakian, "Performance of the Electromagnetic Calorimeter of the HERMES Experiment," *Nucl. Instrum. Meth. A*, vol. 417, pp. 69–78, 1998.

[60] T. Keri, *Detection of exclusive reactions in the Hermes Recoil Fiber Tracker.* PhD thesis, Justus-Liebig Universitaet Giessen, 2008.

[61] M. Hoek, *Design and Construction of a Scintillating Fibre Tracker for measuring Hard Exclusive Reactions at HERMES.* PhD thesis, Justus-Liebig-Universitaet Gissen, 2006.

[62] C. Hulse, *The HERMES recoil photon detector and the study of deeply virtual Compton scattering.* PhD thesis, University Gent, 2010.

[63] G. D. Hill, *Deeply Virtual Compton Scattering off Unpolarised Deuterium at HERMES.* PhD thesis, University of Glasgow, 2008.

[64] W. Wander, M. Duren, M. Ferstl, K. Ackerstaff, M. Funk, *et al.*, "DAD - Distributed ADAMO Database system at HERMES," pp. 349–353, 1995.

[65] W.Wander, *Reconstruction of High-Energy Scattering Event in the HERMES Experiment.* PhD thesis, Friedrich-Alexander-Universitaet-Erlangen-Nuernberg, 1997.

[66] E. Avetisyan, J. Bowl-s, J. Burns, C. Riedl, C. V. Hulse, and S. Yaschenko, "Analysis of the 2006/2007 data," *HERMES Internal Report*, 2009.

[67] C. Shearer, *Spin Matrix Element Extraction for the ρ Vector Meson on Hydrogen and Deuterium Targets at HERMES*. PhD thesis, University of Glasgow, 2005.

[68] X. Lu, "The hermes recoil detector: Particle identification and determination of detector efficiency of the scintillating fiber tracker," 2009. Diploma Thesis.

[69] J. Bowles, J. Burns, M. Murray, W. Nowak, C. Riedl, and S. Yaschenko, "Amplitudes of the single-charge beam-helicity asymmetry in dvcs off a hydrogen target with the proton remaining in the ground state," *HERMES Release Report*, 2011.

[70] X. Lu. and Z. Ye., "Simultaneous Extraction of the BSAs and the BCA Associated with DVCS with the Extended Maximum Likelihood Method," *HERMES Internal Report*, 2007.

[71] F. Ellinghaus, *Beam Charge and Beam Spin Azimuthal Asymmetries in Deeply Virtual Compton Scattering*. PhD thesis, Humboldt-Universität, 2004.

[72] J. Peter Berge and Frank T. Solmitz and Horace D. Taft , "Digital computer analysis of data from bubble chamber. 3. the kinematical analysis of interaction vertices," UCRL-9097.

[73] S. Yaschenko, "Kinematic fitting routine for hermes."

[74] S.N Dymov and V.S Kurbatov and I.N Silin and S.V Yaschenko, "Constrained minimization in the C++ environment," *Nuclear Instruments and Methods in Physics Research Section A: Accelerators, Spectrometers, Detectors and Associated Equipment*, vol. 440, no. 2, pp. 431 – 437, 2000.

[75] R. J. Barlow, "Extended maximum likelihood," *Nucl. Instrum. Meth.*, vol. A297, pp. 469–506, 1990.

[76] F. Brasse et al. *Nucl. Phys. B*, vol. 110, p. 413, 1976.

[77] D. Drechsel, O. Hanstein, S. S. Kamalov, and L. Tiator, "A unitary isobar model for pion photo- and electroproduction on the proton up to 1 GeV," *Nuclear Physics A*, vol. 645, pp. 145–174, Jan. 1999.

[78] B. Krauss, "Statistical Errors and Monte Carlo, HERMES Internal Report," 2005.

[79] Z. Ye., *Transverse Target spin asymmetry associated with deeply virtual Compton scattering on the proton and a resulting model-dependent constraint on the total angular momentum of quarks in the nucleon.* PhD thesis, University of Hamburg, 2006.

[80] V. A. Korotkov and W. D. Nowak, "Future Measurements of Deeply Virtual Compton Scattering at HERMES," *Eur.Phys.J. C*, vol. 23, pp. 455–461, 2002.

[81] M. Vanderhaeghen, P. A. M. Guichon, and M. Guidal, "Computer code for the calculation of dvcs and bh cross sections."

[82] K. Kumericki and D.Mueller, "Computer code for the calculation of dvcs cross sections."

[83] Camacho, C. Munoz and others, "Scaling tests of the cross section for deeply virtual Compton scattering," *Phys. Rev. Lett.*, vol. 97, p. 262002, 2006.

[84] Gavalian, G. and others, "Beam Spin Asymmetries in DVCS with CLAS at 4 .8 GeV," *Phys. Rev.*, vol. C80, p. 035206, 2009.

[85] S. Stepanyan *et al.*, "Observation of exclusive deeply virtual compton scattering in polarized electron beam asymmetry measurements," *Phys. Rev. Lett.*, vol. 87, p. 182002, Oct 2001.

[86] A. Airapetian *et al.*, "Beam-helicity asymmetry arising from deeply virtual Compton scattering measured with kinematically complete event reconstruction," *JHEP*, vol. 1210, p. 042, 2012.

[87] J. Bowles, C. Riedl, and S. Yaschenko in *DIS Procs.*, (2011).

[88] N. d'Hose, E. Burtin, P. Guichon, and J. Marroncle, "Feasibility study of deeply virtual compton scattering using COM PASS at CERN," *The European Physical Journal A - Hadrons and Nuclei*, vol. 19, pp. 47–53, 2004.

[89] M. Guidal and H. Moutarde, "Generalized Parton Distributions from Deeply Virtual Compton Scattering at HERMES," *Eur. Phys. J.*, vol. A42, p. 71, 2002.

[90] J. Bowles, "Target gas contamination studies for hermes," *HERMES Internal Report 09-023*, 2009.